TU Braunschweig - Niedersächsisches Forschungszentrum für Luftfahrt

Berichte aus der Luft- und Raumfahrttechnik

Forschungsbericht 2018-18

Towards improved understanding atmospheric boundary layer processes by airborne high resolution measurements

Dr. Astrid Lampert

TU Braunschweig
Institut für Flugführung

Diese Arbeit erscheint gleichzeitig als von der Fakultät für Maschinenbau der Technischen Universität Carolo-Wilhelmina zu Braunschweig zur Erlangung der venia legendi und der Privatdozentur genehmigte Habilitationsschrift.

https://doi.org/10.24355/dbbs.084-201906170934-0

Die Deutsche Bibliothek - CIP Einheitsaufnahme
Die Deutsche Nationalbibliothek verzeichnet diese Publikation in der Deutschen Nationalbibliografie; detaillierte bibliografische Daten sind im Internet über http://dnb.de abrufbar.

Dr. Astrid Lampert
Towards improved understanding atmospheric boundary layer processes by airborne high resolution measurements

ISBN 978-3-947623-12-9

als Manuskript gedruckt

Diese Arbeit erscheint gleichzeitig als von der Fakultät für Maschinenbau der Technischen Universität Carolo-Wilhelmina zu Braunschweig zur Erlangung der venia legendi und der Privatdozentur genehmigte Habilitationsschrift.

Herausgeber der NFL Forschungsberichte:
TU Braunschweig - Niedersächsisches
Forschungszentrum für Luftfahrt
Hermann-Blenk-Straße 27 · 38108 Braunschweig
Tel: 0531-391-9822 · Fax: 0531-391-9804
Mail: nfl@tu-braunschweig.de
Internet: www.tu-braunschweig.de/nfl

https://doi.org/10.24355/dbbs.084-201906170934-0

Technische Universität Braunschweig

Institut für Flugführung

– Habilitation treatise –

Towards improved understanding atmospheric boundary layer processes by airborne high resolution measurements

November 7th, 2018

Author: Dr. Astrid Lampert
Department: Mechanical Engineering

Technische Universität Braunschweig
Institute of Flight Guidance
Hermann-Blenk-Str. 27
38018 Braunschweig

https://doi.org/10.24355/dbbs.084-201906170934-0

https://doi.org/10.24355/dbbs.084-201906170934-0

To my grandparents

https://doi.org/10.24355/dbbs.084-201906170934-0

https://doi.org/10.24355/dbbs.084-201906170934-0

Table of Contents

List of Symbols **IX**

1 Introduction: Experimental meteorological research with airborne platforms 1
1.1 Motivation . . . 1
1.2 Scientific background . . . 3
1.2.1 Boundary layer development and afternoon-evening transition (AET) 3
1.2.2 Formation and occurrence of the low-level jet (LLJ) . . . 5
1.2.3 Atmospheric aerosol and new particle formation . . . 6
1.3 Technical background . . . 7
1.3.1 Generation of wind energy . . . 7
1.3.2 Overview of airborne humidity sensors . . . 10
1.3.3 State of the art meteorological UAS . . . 14
1.4 Outline of the Treatise . . . 15

2 Carrier Platforms (P) 16
2.1 Research aircraft Dornier Do128 D-IBUF - P1 . . . 16
2.1.1 History and instrumentation Do128 . . . 16
2.1.2 Operation Do128 . . . 17
2.2 Helipod - P2 . . . 18
2.2.1 History and instrumentation Helipod . . . 18
2.2.2 Operation Helipod . . . 19
2.3 Meteorological Mini Aerial Vehicle - P3 . . . 20
2.3.1 History and development M^2AV . . . 20
2.3.2 System M^2AV . . . 20
2.3.3 Operation M^2AV . . . 21
2.4 ALADINA - P4 . . . 22
2.4.1 Development and cooperation ALADINA . . . 22
2.4.2 System ALADINA . . . 22
2.4.3 Operation ALADINA . . . 23
2.5 Quadrocopter ALICE - P5 . . . 24
2.5.1 Development and instrumentation ALICE . . . 24
2.5.2 Operation ALICE . . . 24

3 Methods for signal processing 26
3.1 Complementary filtering technique . . . 26
3.2 Wind vector derivation . . . 28
3.3 Turbulence parameters . . . 29
3.4 Latent heat fluxes . . . 31
3.5 Eddy dissipation rate . . . 31
3.6 Synchronisation of high resolution data . . . 32

https://doi.org/10.24355/dbbs.084-201906170934-0

4 Specific sensors (S) and techniques for boundary layer studies 33
4.1 LICOR water vapour sensor - S1 . . . 33
4.2 Miniaturized payload for UAS - S2 . . . 35
4.2.1 Meteorological payload . . . 35
4.2.2 Aerosol payload . . . 37
4.3 Wind lidar - S3 . . . 38

5 Scientific results from field research studies 40
5.1 Low-level jet statistics and its importance for wind energy (S3) . . . 40
5.1.1 LLJ definition . . . 40
5.1.2 Location of the study . . . 41
5.1.3 Analysis of LLJ events . . . 41
5.1.4 LLJ impact on the Weibull wind speed distribution . . . 43
5.1.5 Intra-annual variability of the Weibull distribution . . . 47
5.1.6 Summary: Importance of LLJ for wind energy . . . 47
5.2 Low-level jet and turbulence anisotropy (P3, S2) . . . 49
5.2.1 Location, instrumentation and modeling . . . 49
5.2.2 Meteorological conditions . . . 50
5.2.3 Development of meteorological parameters during the AET . . . 51
5.2.4 LLJ effects on turbulence parameters . . . 55
5.2.5 Summary: Effect of the LLJ on turbulence parameters . . . 57
5.3 Far field wakes behind offshore wind parks (P1) . . . 58
5.3.1 Overview WIPAFF project . . . 58
5.3.2 Wind parks and flight pattern . . . 60
5.3.3 Observations and analyses of the far field wake . . . 61
5.3.4 Validation of WRF model simulations . . . 62
5.3.5 Potential impact on local climate . . . 63
5.3.6 Summary: Observations of far field wakes behind wind parks . . . 64
5.4 Fast humidity sensors for airborne latent heat fluxes (P1, P2, S1) . . . 67
5.4.1 Airborne experiments . . . 67
5.4.2 Analysis and interpretation of vibrations, humidity spectra and latent heat fluxes . . . 73
5.4.3 Recommendation for airborne applications of LICOR sensors . . . 81
5.4.4 Summary: Airborne application of LICOR hygrometers for latent heat fluxes . . . 82
5.5 New particle formation (P4, S2) . . . 83
5.5.1 Location and instrumentation of the study site . . . 83
5.5.2 NPF in the residual layer only . . . 83
5.5.3 NPF and downward mixing . . . 84
5.5.4 NPF with sporadic downward transport . . . 86
5.5.5 Summary: New particle formation and thermodynamic structure . . . 87

6 Outlook: Future techniques for airborne meteorological research 91
6.1 Potential of meteorological research with unmanned aerial systems . . . 91
6.1.1 Intelligent UAS . . . 91
6.1.2 UAS payload modifications . . . 91

https://doi.org/10.24355/dbbs.084-201906170934-0

6.1.3 UAS for replacing other techniques 92
6.1.4 New methods for measuring meteorological parameters 92
6.1.5 Legal aspects 92
6.2 Dynamic calibration of fast H_2O sensors for research aircraft 95
6.3 Meteorological data for future mobility and energy supply 96
6.4 Future choice of appropriate airborne platforms 97

Bibliography **98**

https://doi.org/10.24355/dbbs.084-201906170934-0

https://doi.org/10.24355/dbbs.084-201906170934-0

List of Symbols

Acronyms

ACTRIS	Europ. Res. Infrastructure for the observation of Aerosol, Clouds, and Trace gases
ALADINA	Application of Light-Weight Aircraft for Detecting In-Situ Aerosol
ABL	atmospheric boundary layer
AET	afternoon evening transition
AGL	above ground level
AMSL	above mean sea level
BC	black carbon
CAA	Civil Aviation Authority
CCN	cloud condensation nuclei
CPC	condensation particle counter
EMEP	European Monitoring and Evaluation Programme
EZ	entrainment zone
GAW	Global Atmosphere Watch
GNSS	Global Navigation Satellite System
GPS	Global Positioning System
H_2O	water
H_2SO_4	sulphuric acid
HAI	Hygrometer for Atmospheric Investigations
IFF	Institute of Flight Guidance
IMU	inertial measurement unit
INS	inertial navigation system
KIT	Karlsruhe Institute of Technology
LiPo	lithium polymer
LLJ	low-level jet
M^2AV	Meteorological Mini Aerial Vehicle
MASC	Multi-Purpose Airborne Sensor Carrier
MINC	Miniature Integrated Navigation and Control System
ML	mixed layer
NH_3	ammonium
NOTAM	Notice to Airmen
NPF	new particle formation
OH	hydroxyl molecule
OPC	optical particle counter
RL	residual layer
ROCS	Research Onboard Computer System
RPAS	remotely piloted aircraft system
SBL	stable boundary layer

https://doi.org/10.24355/dbbs.084-201906170934-0

TKE	turbulent kinetic energy
TROPOS	Leibniz Institute of Tropospheric Research
TSMPS	Twin Scanning Mobility Particle Sizer
UAS	unmanned aerial system
UAV	unmanned aerial vehicle
UL/DEWI	Unterwriters Laboratories/Deutsches Windenergie-Institut
UTC	coordinated universal time
WIPAFF	Wind Park Far Field
WRF	Weather Research and Forecast Model
gs	ground speed
n.a.	not available
tas	true air speed

Symbols

α	$^\circ$	angle of attack
β	$^\circ$	angle of sideslip
β	2	Kolmogorov constant
γ	-	ratio of heat capacity at constant pressure and at constant volume
ϵ	$\mathrm{J\,kg^{-1}\,s^{-1}}$	eddy dissipation rate
ϵ_0	$8.85\cdot 10^{-12}\,\mathrm{A\,s\,V^{-1}\,m^{-1}}$	dielectric constant of vacuum
ϵ_r	-	relative dielectric permittivity
θ	K	potential temperature
κ	-	shape factor
λ	$\mathrm{m\,s^{-1}}$	scale factor
ρ	$\mathrm{kg\,m^{-3}}$	air density
σ_u^2	$\mathrm{m\,s^{-1}}$	wind speed variance, u direction
σ_v^2	$\mathrm{m\,s^{-1}}$	wind speed variance, v direction
σ_w^2	$\mathrm{m\,s^{-1}}$	wind speed variance, w direction
τ	s	rotation period
Θ	$^\circ$	pitch angle
$\vec{\Omega}$	$^\circ\,\mathrm{s^{-1}}$	vector of angular momentum rates
Φ	$^\circ$	bank (roll) angle
Ψ	$^\circ$	yaw (heading, azimuth) angle
A	$\mathrm{m^2}$	area
A	-	anisotropy ratio
C	W	capacity
C_p	-	power coefficient
D	-	structure function
E	$\mathrm{W\,m^{-2}}$	latent heat flux
E_{kin}	J	kinetic energy
I	$\mathrm{W\,m^{-2}}$	transmitted radiation
I_0	$\mathrm{W\,m^{-2}}$	emitted radiation
L	$\mathrm{J\,kg^{-1}}$	evaporation heat
$\underline{M}_{fa}$	-	transformation matrix aerodynamic to aircraft-fixed

https://doi.org/10.24355/dbbs.084-201906170934-0

$\underline{M}_{gf}$	-	transformation matrix aircraft-fixed to geodetic
Ma	-	Mach number
N	cm^{-3}	particle number concentration
P	W	power
R	$8.3\,\mathrm{J\,K^{-1}\,mol^{-1}}$	gas constant
T	K	temperature
T_{static}	K	static air temperature
T_{total}	K	total temperature
V	$\mathrm{m\,s^{-1}}$	horizontal wind speed
c_p	$29.07\,\mathrm{J\,kg^{-1}\,K^{-1}}$	specific heat capacity at constant pressure
c_v	$20.76\,\mathrm{J\,kg^{-1}\,K^{-1}}$	specific heat capacity at constant volume
d	m	distance
f	-	Weibull probability distribution function
f	Hz	frequency
k	m^{-1}	absorption coefficient
k	$^{-1}$	wave number
m	kg	mass
m	$\mathrm{g\,kg^{-1}}$	mixing ratio
p	hPa	pressure
p_0	hPa	pressure at surface
q	$\mathrm{g\,kg^{-1}}$	specific humidity
s	m	distance
$\vec{s}$	m	lever arm vector
t	s	time
v	$\mathrm{m\,s^{-1}}$	wind speed
$\vec{v} = (u, v, w)$	$\mathrm{m\,s^{-1}}$	wind vector, met. coord. (East/North/Up positive)
$\vec{v_a}$	$\mathrm{m\,s^{-1}}$	air flow vector, aerodynamic coordinate system
$\vec{v_g}$	$\mathrm{m\,s^{-1}}$	wind vector, geodetic coordinate system
$\vec{v_{gs}}$	$\mathrm{m\,s^{-1}}$	ground speed
v_{tas}	$\mathrm{m\,s^{-1}}$	true air speed

https://doi.org/10.24355/dbbs.084-201906170934-0

https://doi.org/10.24355/dbbs.084-201906170934-0

1 Introduction: Experimental meteorological research with airborne platforms

This habilitation treatise describes experimental meteorological research with airborne platforms operated at the Department of Mechanical Engineering of the Technische Universität Braunschweig. The research was done at the work group "Airborne Meteorology and Measurement Techniques". Within this project, the methods and results of three different topics are combined:

- "Meteorology", which involves several phenomena in the atmospheric boundary layer
- "Airborne" platforms which are used as sensor carriers
- "Measurement techniques" and corresponding sensors specially designed to describe the physical properties of the atmospheric boundary layer.

Therefore the introduction below presents the scientific and technical background and current knowledge related to the proposed research fields which concern mainly: the characterisation of the low-level atmospheric layer which is of prime interest for onshore and offshore wind farm performance, the humidity fluxes and the formation of new particles which drive cloud formation. Of the many flying platforms (P) and sensors (S) that are used worldwide for airborne meteorology, the P-S combinations of the presented studies, and that are necessary to obtain results beyond the current state of the art, are described in the following within the scientific context.

1.1 Motivation

Airborne meteorological data sets fill an important gap between continuous stationary ground-based data with high temporal resolution and the global coverage of of radar and satellite remote observations. In many cases, the understanding of atmospheric processes requires the flexible probing of the air at certain altitudes and within well defined lateral boundaries (Martin et al., 2011).
Fundamental meteorological research is not only a purpose on its own, but there are highly complex interactions of atmospheric phenomena with modern human infrastructure, like the generation of renewable energy and aviation. Especially since the decision to end the use of nuclear power in Germany (Coalition Agreement, 2013), the installation of wind turbines is rapidly growing at onshore and offshore locations. Therefore, a profound knowledge of wind field properties and accurate prediction tools are essential to overcome the

https://doi.org/10.24355/dbbs.084-201906170934-0

challenges of the high wind speed variability, to develop flexible storage or feeding-in solutions, and finally to handle the non-constant power output.
For investigating the onset of cloud formation, for understanding the role of aerosol particles in this environment, and for observing the early stage development of clouds, there is the need for in situ data of temperature, humidity, turbulence, aerosol content and characteristics (Wehner et al., 2015). As clouds are highly dynamic features, moving along the main wind direction, the strategies of repeated probing at the same location and travelling with the mean wind speed provide promising data output. Another example is the missing link of greenhous gas emissions from locally installed point measurements to the coarser global satellite data. For a realistic estimation and model validation of regional emission budgets, it is necessary to expand the continuous local observations to scenarios covering scales of several 100 km.
Depending on the application, different types of airborne vehicles can be the best compromise between endurance, flight altitude, space and weight requirements, logistical constraints, complexity and cost. The spectrum of airborne systems for atmospheric research has been extended in the last decades to smaller scales by the emerging and quickly developing technology of unmanned aerial systems (UAS). The integration into the air space is a current challenge, as more and more research institutes, federal agencies, companies and private persons want to profit from the advantages of the comparatively low-cost systems.
Aviation strongly depends on accurate weather information. Additionally to the nowadays available meteorological tools for weather briefing, the need for new products and additional real-time data in the cockpit is a current research field. These additional data might be warnings of wind shear or enhanced turbulence, an automated detection of aircraft wakes, or a short-term forecast (nowcast) of thunderstorm cells (Sauer et al., 2016).
In this treatise, five different research field studies are addressed, each with its own technical challenges that were considered by applying specific platforms, sensors and data processing. They can be summarized as the following:

- With the increasing number of onshore and offshore wind farms erected in Germany, the estimation and forecasting of the wind speed distribution are an important challenge. They are actually derived from continuous surface observations, models and few upper air soundings. However, typical wind phenomena like the low-level jet (LLJ), a narrow sized altitude interval with strongly enhanced wind speed during stable atmospheric conditions, are difficult to capture in numerical models. Because LLJ may play a significant role for wind energy, as they typically appear around hub height of wind turbines (Lampert et al., 2015), their properties need to be accurately analysed from measured wind profiles.

- Associated with the low level jet mentioned above is an increase in turbulence induced by wind shear. Turbulence can be described as eddies of different size. As the low level jet typically appears during the night above land, and during the day above the ocean, when the atmosphere is stably stratified with vertical motions suppressed, this can significantly modify anisotropy properties of turbulence (Lampert et al., 2016) and therefore increase vertical transport processes. These turbulence properties can be can be described using specific sensors on airborne platforms at

https://doi.org/10.24355/dbbs.084-201906170934-0

the corresponding altitudes (Canut et al., 2016).

- Turbulence and atmospheric stability play an important role for the extent of wakes behind offshore wind parks. The energy for turning the wind turbine is extracted from the wind field, reducing the wind speed behind the wind park even in the far field of several km (Emeis et al., 2016) to several 10 km (Platis et al., 2018). The wind speed recovers quickly when high turbulence and unstable atmospheric stratification prevail. The correct simulation of wakes in mesoscale models can be validated with airborne data sets (Siedersleben et al., 2018a). For studying changes in temperature and humidity downstream of wind parks, airborne measurements are required (Siedersleben et al., 2018b).

- Moisture in the atmosphere is of high importance as the base for cloud formation. Further, latent heat fluxes represent an important term in the energy balance, providing the transport of both energy and moisture from the surface into the atmosphere. Therefore, the airborne quantification of latent heat fluxes on a scale of 100 km fills an important gap for global climate models, and serves to determine if measurements at fixed locations are representative for the area. However, the prerequisite for reliable latent heat fluxes is the validation of fast humidity sensors concerning their time delay, response time and spectral behaviour (Lampert et al., 2018a).

- The formation of new particles in the atmosphere has been mostly studied by ground-based observations. However, as the largest part of particles is not emitted directly from the surface into the atmosphere but forms from precursor gases, it is essential to study atmospheric processes contributing to these events directly at the altitudes where particle bursts are located (Altstädter et al., 2015, Platis et al., 2015). The results are used to validate models and theories, and reveal that even for "unfavorable" conditions under cloudy sky, these processes can occur (Altstädter et al., 2018a).

For the different research fields that are addressed in this habilitation treatise, the scientific and technical state of the art background information is presented with details in the following sections.

1.2 Scientific background

Several topics will be presented below, namely: (i) the boundary layer development and afternoon-evening transition (AET), (ii) the formation and occurrence of the low-level jet (LLJ) and (iii) the atmospheric aerosol and new particle formation.

1.2.1 Boundary layer development and afternoon-evening transition (AET)

Atmospheric stability describes the way an air parcel moves after being deflected in the vertical. If it experiences a repulsing force and is moved back to the original position, the

https://doi.org/10.24355/dbbs.084-201906170934-0

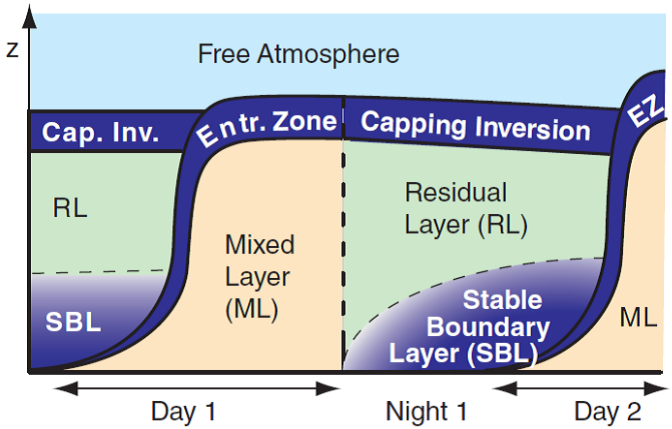

Figure 1.1: The diurnal development of the atmospheric boundary layer. Figure from Stull (2017)

atmosphere is stably stratified. If the air parcel experiences an accelerating force moving it further away from its original position, the atmosphere is unstably stratified (or mixed). To determine the atmospheric stability, the vertical profile of the potential temperature is used. The potential temperature is defined as the temperature θ that an air parcel at a specific altitude with the corresponding pressure p and temperature T would have after moving it adiabatically to sea level altitude with normal pressure p_0=1013,25 hPa (Stull, 1988).

$$\theta = T \cdot (\frac{p_0}{p})^{\frac{R}{c_p}} \tag{1.1}$$

In this formula R=8.31 J K^{-1} mol^{-1} represents the gas constant of air and c_p is the specific heat capacity at constant pressure. If the potential temperature increases with altitude, the atmosphere is stably stratified, if it decreases, the atmosphere is unstable. For constant potential temperature with height, steady movements of air parcels without dynamic acceleration forces are possible.

The atmospheric boundary layer (ABL) is characterized by a typical diurnal cycle (Fig. 1.1), described e.g. by Stull (1988): For conditions of low wind speed and only scattered cloud cover, the ABL is convectively mixed (unstable, called mixed layer, ML) up to a certain altitude between typically several 100 m to 1.5 km around noon (Wildmann et al., 2015). Also the ML is covered by a capping inversion, separating the ABL from the free troposphere. With decreasing solar radiation, vertical mixing is reduced, and gradually a temperature inversion builds up from the surface. During the night, there is a stably stratified atmospheric boundary layer (SBL) from the ground up to several 100 m (Stull, 1988, Kaimal and Finnigan, 1994). Above the temperature inversion, there are remnants of the part of the ABL that was included in the turbulently mixed ABL during the day,

https://doi.org/10.24355/dbbs.084-201906170934-0

the so-called residual layer (RL). This layer is decoupled from the surface by thermal stratification, and therefore does not experience friction forces induced by the surface. After sunrise, the temperature inversion is heated away from the ground (so called morning transition,e.g. Angevine et al., 2001), until the residual layer is included in the turbulently mixed layer again. The area where turbulent mixing between the ABL and the free troposphere takes place is called entrainment zone (EZ).
The transition of the atmospheric boundary layer from convectively mixed during daytime to stably stratified during night time is called "afternoon-evening transition". There are different definitions for the time interval of the AET. As the driving process of the AET is the atmospheric cooling due to longwave radiation and decreasing solar irradiance, the beginning of the AET is often defined by the the onset of decreasing sensible heat fluxes at the surface (Nadeau et al., 2011). The AET ends when the sensible heat flux at the surface becomes negative. The meteorological parameters undergo significant changes during the AET: The wind speed typically decreases (Mahrt, 1981), sometimes associated with a change in wind direction (Stull, 1988), the near surface temperature decreases, and the mixing ratio increases quickly (Fitzjarrald and Lala, 1989). A ground-based temperature inversion builds up, which reduces the turbulence in horizontal and vertical direction (Busse and Knupp, 2012). Typically, the turbulent kinetic energy, which is a measure of turbulence (see Sect. 3.3), decreases first slowly, while there is still influence of solar radiation, and then rapidly after sunset (Nadeau et al., 2011). Also the spectral shape of turbulence and anisotropy are altered during the AET (Darbieu et al., 2015): Under convective conditions and low wind speed, turbulence is almost isotropically distributed in the three directions. With increasing stability, vertical motions are damped, and turbulent eddies are elongated in horizontal direction (Canut et al., 2016).
In contrast to the better understood and mostly homogeneous morning transition (Wildmann et al., 2015), the processes during the AET occur spatially inhomogeneous on different scales. These local differences further influence the ABL development during the night (Acevedo and Fitzjarrald, 2001, Cuxart et al., 2016). In complex terrain, local temperature gradients may contribute to the development of a nocturnal Low-level Jet (LLJ, Conangla and Cuxart, 2006). The stronger wind speed during LLJ events enhances the anisotropy, as eddies are elongated even further in horizontal direction (Mason and Thomson, 1987, Mauritsen and Svensson, 2007).
Above large open water surfaces, e.g. the North Sea, the diurnal cycle of atmospheric stability can be inverted: With the larger heat capacity, the surface temperature of water is almost constant over time periods of several days. The atmospheric temperature near the surface is therefore often higher than the water temperature during the day and lower during the night. This leads to the land-sea circulation or sea breeze (Savijärvi et al., 2005, Steele et al., 2015). Therefore, stable stratification can be expected during the day, and especially in the afternoon for certain wind directions, when air masses warmed up above land surfaces are transported above the open water (Smedman et al., 1997). This results in LLJ appearance during the day (Lampert et al., 2018b). During the night, unstable stratification with enhanced vertical transport of moisture and the formation of sea smoke can be expected (Saunders, 1964). Stable stratifications in the North Sea occur more than 20% of the time on an annual base (Platis et al., 2018), and even more frequently in the Baltic Sea (Smedman et al., 1997, Dörenkämper et al., 2015). The main seasons for encountering these conditions above the North Sea are spring and summer (Coelingh et al.,

https://doi.org/10.24355/dbbs.084-201906170934-0

1996), although stable stratifications have been reported in October as well (Lampert et al., 2018a, Platis et al., 2018).

1.2.2 Formation and occurrence of the low-level jet (LLJ)

Like the well-known jet stream, the low-level jet denominates a strong and vertically confined wind band, occurring, however, at much lower altitudes. The LLJ is located in the atmospheric boundary layer, usually with a vertical extent of 50 to 200 m (e.g. Wittich et al., 1986, Baas et al., 2010, Prabha et al., 2011). In theory, the ABL is sub-divided into the ground-layer or Prandtl layer, in which the Coriolis force is negligible compared to the friction force (extending up to some 10 m, depending on season and roughness of the location) and the Ekman layer above. The vertical wind profile according to the classical theory is a logarithmic increase in the ground-layer, which is often approximated by a power law, and a wind profile reaching the geostrophic wind with asymptotic behavior and a characteristic rotation of the wind direction, the Ekman spiral, in the Ekman layer (Emeis, 2001).
Above land, the LLJ typically forms during the afternoon transition on clear sky days: The formerly convectively mixed ABL changes to the stably stratified nocturnal ABL. As a ground-based temperature inversion builds up by radiative cooling under clear sky conditions, the upper parts of the ABL, called residual layer, are decoupled from the direct influence of the surface (Davies, 2000). The friction force does not reach the residual layer any more, and the wind speed can even exceed the geostrophic wind speed (Davies, 2000), which results from the equilibrium of the pressure gradient force and the Coriolis force in the free troposphere above the ABL.
However, the LLJ above land surface is not only observed during the afternoon and evening transition, but during the second half of the night as well (e.g., Banta et al., 2002, Abdou et al., 2010), and less frequently during the day (e.g., Baas et al., 2009). These LLJ events may be caused and influenced by synoptic-scale baroclinity (Stensrud, 1996), the passage of fronts (Doyle and Warner, 1993), or orographic effects (Banta et al., 2002). Its properties and occurrence strongly depend on the meteorological situation, like the strength of the temperature inversion (e.g., Baas et al., 2009, Kallistratova et al., 2009) and general circulation type (Emeis, 2014), as well as in detail the geostrophic wind speed and presence of clouds (Emeis, 2014). In some areas, the phenomenon occurs regularly in a predictable way and is exploited for wind energy (Banta et al., 2002). Also above the ocean, LLJ events have been reported (Parish, 2000, Garreaud and Muñoz, 2005, Savijärvi et al., 2005).
In Europe, specific LLJ events have been analysed (e.g. Kallistratova et al., 2013), and some climatologies are available (Baas et al., 2009). In Spain, LLJ observations at a relatively low altitude of 90 m with a wind speed maximum of 7 to 8 $\mathrm{m\,s^{-1}}$ have been reported (Conangla and Cuxart, 2006).
Near the location of Braunschweig airport, which is the study site for the experiment presented in Sect. 5.1, some experimental and numerical studies on LLJ occurrence have been conducted (Kottmeier et al., 1980, Kraus et al., 1985, Wittich et al., 1986, Emeis, 2014). The typical altitude of the wind speed maximum was found to be at around 200 m (Kraus et al., 1985, Wittich et al., 1986). The relationship of the LLJ with global warm-

https://doi.org/10.24355/dbbs.084-201906170934-0

ing has been analysed with the help of a regional climate model, and the LLJ altitude is expected to shift upwards (Gross, 2012).

1.2.3 Atmospheric aerosol and new particle formation

Aerosol particles play a crucial role in the climate system directly by influencing the radiation budget and indirectly by acting as cloud condensation nuclei and therefore interacting with the hydrological cycle (IPCC, 2013), and modify local ABL dynamics (Barbaro et al., 2014). However, their local and global impact are difficult to quantify, as they are highly variable both on temporal and on spatial scales. Additionally, their chemical composition, microphysical and optical properties vary substantially. The Earth's surface can act either as a source or sink for aerosol particles and precursor gases. Aerosol formation, uptake, mixing, growth and gravitational settling proceed throughout the ABL. The vertical aerosol concentration is connected to the thermodynamic structure of the atmosphere. It is well-mixed in a turbulent ABL and forms layers of different properties in a thermally stably stratified boundary layer, as well as in the free troposphere (e.g., Stone et al., 2010). The new formation of a large number of nucleation mode particles (size range from ∼3 to 15 nm in the particle diameter) in the ABL has been observed worldwide at various rural, marine, urban and polar observation sites and constitutes a significant source of the atmospheric aerosol (Kulmala et al., 2004). Different nucleation processes lead to the formation and, if sufficient condensable gases are available, to subsequent growth of particles to a detectable size above 3 nm and further to the Aitken mode size (∼15 to 100 nm) within a few hours. Then they may act as cloud condensation nuclei (CCN) and scatter solar radiation, influencing the regional and global climate (Spracklen et al., 2008). Wiedensohler et al. (2009) showed that new particle formation (NPF) may enhance the available CCN by an order of one magnitude. However, a large number of Aitken mode particles represents a condensation sink for condensable gases and inhibits NPF (Wehner et al., 2007). Being able to understand and predict NPF is a key issue in quantifying the direct and indirect aerosol effects on climate. In the ABL, particle bursts have been reported in the entrainment zone (Nilsson et al., 2001), the residual layer (Stratmann et al., 2003), and the convectively mixed layer (Stratmann et al., 2003). In the EZ and the RL, a likely theory describes the mechanism of NPF as binary nucleation of sulphuric acid H_2SO_4 and water vapour H_2O (Kulmala et al., 2004). Models and measurements indicate that near the surface, ternary nucleation involving the ingredients sulphuric acid H_2SO_4, water vapour H_2O, and ammonium NH_3 is a possible process (Korhonen et al., 1999), and organic volatile compounds play a crucial role in some cases (Lyubovtseva et al., 2005). Above a certain particle diameter, volatile material dominates the particle growth (Wehner et al., 2007). Ground-based observations of NPF were connected to intense solar radiation (O'Dowd et al., 1999, Nilsson et al., 2001), high vertical wind gradients (indicating a strong turbulent mixing), downward particle flux, low water vapour concentration and enhanced ozone concentration (Boy et al., 2003). Some studies indicate that there is a relation with turbulence (Bigg, 1997, Nilsson et al., 2001). NPF was observed in regions with increased turbulence within the RL (Stratmann et al., 2003, Siebert et al., 2007, Wehner et al., 2010), while these particles were mixed downwards and detected at ground stations later on. A network of ground-based observations revealed a mesoscale horizontal extent of NPF over

https://doi.org/10.24355/dbbs.084-201906170934-0

hundreds of kilometers (Wehner et al., 2007). Further, NPF was often observed with intermittent direct solar radiation, at the edges of clouds (Keil and Wendisch, 2001, Wehner et al., 2015). Airborne measurements investigated the large scale variability of the particle concentrations along air mass trajectories (O'Dowd et al., 2009). Detailed high resolution measurements of the small-scale vertical and horizontal variability are recommended for the implementation of NPF in models (Boy et al., 2006, Hellmuth, 2006).

1.3 Technical background

The following section provides the technical background related to the field research studies described above with emphasising the state of the art on the generation of wind energy, on the techniques for measuring humidity and on the use of unmanned aerial sytems.

1.3.1 Generation of wind energy

To describe the characteristics of wind for various research fields, different methods are applied. The current wind profile for a specific site is of interest for aviation (e.g. wind shear information for helicopter pilots who land in wind parks). In many cases, wind is only measured at ground or at a specific altitude, and a power law or logarithmic extrapolation of the wind profile is used to estimate the wind speed at higher altitudes (Justus and Mihilai, 1976). However, this does not necessarily provide realistic wind profiles (Lampert et al., 2015).
The kinetic energy E_{kin} contained in the horizontal motion of the atmosphere with wind speed v can be calculated as

$$E_{kin} = \frac{1}{2} \cdot m \cdot v^2 \tag{1.2}$$

The mass flowing through the area A swept by the rotor blades of a wind turbine in a time t can be substituted by the air density ρ:

$$E_{kin} = \frac{1}{2} \cdot \rho \cdot A \cdot v \cdot t \cdot v^2 \tag{1.3}$$

Therefore the power P_{air} passing through the rotor area is

$$P_{air} = \frac{E_{kin}}{t} = \frac{1}{2} \cdot \rho \cdot A \cdot v^3 \tag{1.4}$$

The available power determines the energy output of a specific wind turbine, and is proportional to the cubed value of the horizontal wind speed (Burton et al., 2011). The power output P of a wind turbine can then be calculated according to

$$P = \frac{1}{2} \cdot \rho \cdot v^3 \cdot C_p \cdot A \tag{1.5}$$

C_p is the power coefficient, which depends on the wind speed and can theoretically reach a maximum of 0.59. A typical power coefficient for the wind turbine of type Siemens SWT-3.6-120 with a rotor diameter of 120 m is shown in Fig. 1.2 (Siemens Website, 2018). The "cut-in" speed, where the turbine starts to produce power, is 3-4 $\mathrm{m\,s^{-1}}$, the "rated speed" above which there is constant power output is 12-13 $\mathrm{m\,s^{-1}}$, and the "cut-out speed", at

https://doi.org/10.24355/dbbs.084-201906170934-0

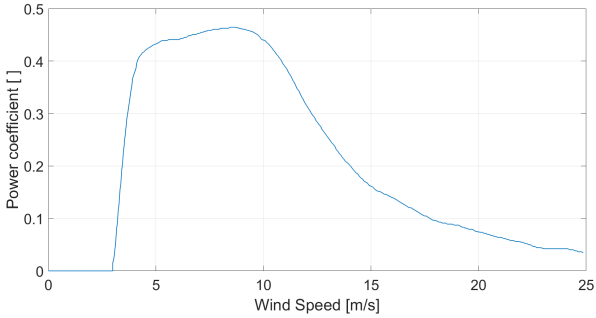

Figure 1.2: Power coefficient of the wind turbine Siemens SWT-3.6-120. (Siemens Website, 2018)

which the wind turbine is switched off for security reasons, is $25\,\mathrm{m\,s^{-1}}$. This means that below the so called rated speed, there is a cubic relationship between horizontal wind speed and power output. Higher wind speed means higher energy production. However, high wind speed is often associated with high wind shear, which increases the system loads and may have a negative impact on life time (Gutierrez et al., 2016). A thorough knowledge of the expected wind speed distribution is therefore essential for chosing an appropriate site for wind turbines. The wind speed distribution is often expressed as a Weibull probability density distribution for a certain altitude:

$$f(V) = \frac{\kappa}{\lambda} \cdot (\frac{V}{\lambda})^{\kappa-1} exp^{-(\frac{V}{\lambda})^{\kappa}} \tag{1.6}$$

Here, f is the Weibull probability distribution function, V is the horizontal wind speed, κ is the dimensionless shape factor, and λ is the scale factor in $\mathrm{m\,s^{-1}}$. In this study, the Weibull distribution of the wind data is calculated according to the maximum likelihood method (see e.g., Stevens and Smulders, 1979).
Some standards (IEC 61400-12 and DIN EN 61400-12-1) apply instead the Rayleigh distribution with a fixed shape parameter of 2, which is typical for Europe (Burton et al., 2011).

In the German Bight, large clusters of offshore windparks are planned and realized. The offshore wind park capacity will reach 7.8 GW until 2020 (Neddernann and Neumann, 2015). The current state of wind parks in operation (spring 2018) is shown in Fig. 1.3. However, as individual wind turbines extract kinetic energy from the wind field and therefore reduce the wind speed, shadowing effects for the neighbouring wind turbines and whole wind parks can be expected. The superclusters are oriented along the main wind direction South-West (Emeis et al., 2016, Leiding et al., 2016), and West, therefore a large interaction between the wind parks can be expected. Power losses between individual wind turbines within a wind park are in the range of several 10% for unstable and even more for stable conditions (El-Asha et al., 2017), with the highest relative losses behind the

https://doi.org/10.24355/dbbs.084-201906170934-0

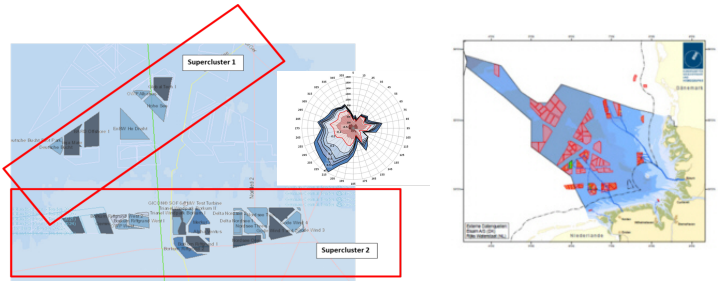

Figure 1.3: Left: Operational (grey) and planned (blue) wind parks in the German Bight in December 2017. Source: *http : //www.4coffshore-.com/windfarms/windfarms.aspx?windfarmId = DE*13. Two superclusters are indicated, where a high impact on downstream windparks can be expected. Wind rose: UL DEWI. Right: Overview of the planned wind parks in the German Bight (red polygons). Source: *http : //www.bsh.de/de/Meeresnutzung/Wirtschaft/Windparks-/Windparks/PNS.jsp*

first two rows of wind turbines (Hansen et al., 2012), and the absolute losses increasing with each row (Barthelmie et al., 2007). Even the wind decrease within one wind park is difficult to represent in numerical simulations due to the dependence on meteorological conditions (Barthelmie et al., 2009), and for this reason wake interactions between individual wind turbines cannot be simulated satisfactorily (Troldborg et al., 2011). Further, enhanced turbulence contributes to power losses, but is difficult to quantify (Foreman et al., 2017). As for the decay of aircraft wake vortices (e.g., Holzäpfel and Gerz, 1999, Holzäpfel, 2003), the length of these effects depends on the atmospheric stability (Türk and Emeis, 2010). Turbulence produced mechanically by friction forces and thermal convection is low above the smooth sea surface, leading to long far field wakes (Dörenkämper et al., 2015), in contrast to conditions above land, where wakes recover within few km downstream of wind parks. Especially for stable conditions, the downward transport of momentum is suppressed, which is the main mechanism to reduce wakes (Emeis, 2010). Synthetic aperture radar (SAR) satellite images of sea surface roughness (Fig. 1.4) show the presence of large far field wakes under stable conditions (Li and Lehner, 2013, Christiansen and Hasager, 2005). Also numerical simulations suggest that far reaching wakes can be expected for stable atmospheric conditions (Fitch et al., 2012). These large areas of reduced wind speed interact with downstream wind parks and reduce the power output. Therefore, it is of high relevance to improve forecasting of wake length to obtain a realistic estimate of expected power output of wind parks. Stable stratifications and LLJ phenomena are not yet included in industrial models like WindFarmer or Openwind to forecast the power output of wind parks. Instead they consider only neutral conditions and a logarithmic wind profile. The importance of including wind profiles in models, not only wind data at hub height, is acknowledged by the wind energy community in recent

https://doi.org/10.24355/dbbs.084-201906170934-0

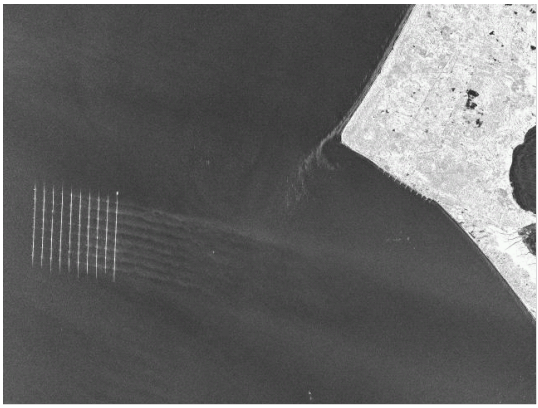

Figure 1.4: SAR image of the wind park Horns Rev off the Danish West coast on 16 February 2012. The wind is coming from westerly direction. Wakes are visible in the east of the wind park. Figure from Emeis et al. (2016) Source: DLR.

years (Wagner et al., 2009, Eecen et al., 2011, Wagner et al., 2011, Paulsen and Wagner, 2012, Wagner et al., 2014).

1.3.2 Overview of airborne humidity sensors

Water vapour and clouds in the atmosphere have a large impact on the energy balance (Ramanathan et al., 1989), the hydrologic cycle (e.g. Chahine, 1992) and therefore on local and global climate (Trenberth et al., 2007, Zhou et al., 2011). A general increase in ABL air moisture and humidity within the troposphere has been reported (IPCC, 2013). The distribution of moisture is difficult to measure and model accurately due to its large spatial and temporal variability (e.g. Klaus et al., 2012).
Airborne sensors for meteorological research have to fullfil specific requirements. On the one hand, a high temporal resolution is needed in order to obtain a high spatial resolution for the moving platforms. On the other hand, long-term stability and high accuracy, if possible without the need of frequent re-calibration, are essential. In practice, this leads to the combination of complementary sensors for both high resolution and long-term accuracy. Measuring humidity with high accuracy is challenging. In the troposphere, the water vapour concentration varies over three orders of magnitude, with high spatial and temporal variability. Also for well controlled conditions in a cloud chamber, intercomparison measurements of different hygrometers probing the same air simultaneously revealed discrepancies between different measurement systems around 10 %, and for cold and dry conditions similar to the upper troposphere and lower stratosphere, the instruments had a variation around the reference value of 20 % (Fahey et al., 2014).
In principle, four methods of measuring humidity are known and commonly applied for airborne measurements:

https://doi.org/10.24355/dbbs.084-201906170934-0

- The capacitive hygrometer, e.g. a Vaisala humicap, is based on changes in the capacity for different ambient humidity. The sensor consists of a dielectric material (organic polymer or porous ceramics), which is highly sensitive to humidity, included in a capacitor. The capacity C is related to the relative dielectric constant or permittivity ϵ_r according to the formula

$$C = \epsilon_0 \cdot \epsilon_r \cdot \frac{A}{d_1} \tag{1.7}$$

  Here, ϵ_0 denotes the dielectric constant of vacuum (ϵ_0=8.85·10^{-12} A s V^{-1} m^{-1}), ϵ_r is the relative dielectric permittivity, d_1 the distance between the capacitor plates, and A the area of the condensator plates. Changes of the capacity are caused by changes in the relative dielectric constant ϵ_r, which depends on the uptake of water vapour. Changes in the relative humidity are attributed to changes in the capacitance by calibration. The results may be hampered by contamination of the dielectric material, e.g. by aerosol particles, especially if they have a hygroscopic effect (Wildmann et al., 2014b). Therefore regular check of the calibration and cleaning of the sensor is required.
  The system is relatively inexpensive and light-weight. A disadvantage is the limited response time of around 1 to 10 s, which can be improved by an inverse modelling technique (Wildmann et al., 2014b). The comparatively large response time results in a hysteresis effect, which is additionally biased, as increasing humidity results in a faster response time than decreasing humidity, where diffusive processes to remove the humidity from the sensor are slower.

- The dew point mirror is based on the principle of condensing humidity on a metal mirror, which is quickly cooled down to the dew point temperature by a Peltier element. The changes in the reflectivity of the mirror are registered optically. The response time of the dew point mirror strongly depends on the ambient temperature, but as well on the accuracy and speed of the temperature control, with a typical value of 0.5 s (e.g. for the dew point mirror TP3S of Meteolabor). The response time increases for cold conditions. Further, quick changes in humidity may not be captured reliably. Altogether, the dew point mirror is often used as reference, as it has a higher accuracy than the capacitive sensor. Problems may arise from a too high or too low air speed at the sensor, as mentioned in Beaton and Spowart (2012).

- The absorption hygrometer, e.g. the Lyman Alpha sensor of Buck research and the combined humidity and CO_2 sensor of LICOR, is based on the property of water vapour to absorb radiation in different wavelength ranges, from the UV to the IR spectral range. The spectrum of many water vapour absorption lines (absorption bands) in the wavelength range between 1300 and 3000 nm (IR) is shown in Fig. 1.5. The absorption lines of water vapour result from discrete transitions from one energetic eigen state to a different rotational, vibrational or electronic state, described by quantum mechanics. The radiation in a small wavelength range (quasi monochromatic light) is attenuated by molecular absorption according to the Lambert-Beer relationship

$$I = I_0 \cdot e^{\frac{-k \cdot d_2 \cdot q}{q_0}} \tag{1.8}$$

https://doi.org/10.24355/dbbs.084-201906170934-0

Here, I denotes the transmitted radiation after the attenuation in the measurement cell, I_0 is the incoming radiation, k is the absorption coefficient of water vapour for this particular wavelength, which is proportional to the density of absorbing molecules and the absorption cross section, d_2 is the optical path length of the measurement cell, and $\frac{q}{q_0}$ represents the normalized water vapour content in humid air (Foken, 1990). Absorption hygrometers are more costly, heavy, and require a sophisticated installation for airborne measurements. Some absorption hygrometers are designed as open path sensors, sampling directly the ambient air passing through an open measurement cell. Others are extractive systems, that need a pump to guide the air to a closed measurement cell. This technique provides much higher measurement frequencies in the range of 20 to 100 Hz compared to the humidity sensors mentioned above. Disadvantages are the cross-sensitivity to other trace gases, and the need to measure additional control parameters (pressure, temperature) in the humidity channel.
A particular system is the fluorescence hygrometer, which is used for airborne applications as well (Zöger et al., 1999, Schiller et al., 2008). In this form, water vapour molecules are dissociated by radiation at a wavelength smaller than 137 nm, creating electonically excited states of the hydroxyl molecule (OH). The fluorescence light emitted during relaxation to the ground state in the wavelength range 280 nm to 330 nm is recorded, providing the concentration of water vapour (Zöger et al., 1999).

- The tunable diode laser absorption spectrometer (TDLAS) is based on the principle of quickly scanning a small spectral range around a single water vapour absorption line. Then the absorption spectrum is analysed. Not only information on the concentration of water vapour, but as well on ambient pressure and temperature can be derived. The method achieves the highest possible accuracy and the highest frequency up to several kHz, without the need of calibration (Buchholz et al., 2013, 2014). However, to date, data are not available in real-time but require extensive post processing. The sensors are experimental systems and not commercially available.

For decades, the Lyman Alpha, used here as a synonym for the Lyman Alpha sensor of Buck Research, US (Buck, 1973), belonging to the group of absorption hygrometers, has been used as the standard fast humidity sensor with a measurement frequency of up to 100 Hz (Buck, 1976). It is based on the emission of ultraviolet (UV) radiation with a wavelength of 121.56 nm (transition of an electron from the first excited state n=2 to the ground state n=1 in the hydrogen atom, called Lyman Alpha emission line). The lamp used as source for the radiation is based on glow discharge of hydrogen. It has been manufactured by the company Buck Research, and cannot be purchased commercially any more. The required length of the measurement chamber is only a few mm (Buck, 1976). As the Lyman Alpha wavelength is strongly absorbed by water vapour, the signal in the ion chamber detector is weakened accordingly. The Lyman Alpha sensor has been operated in many research aircraft (Busen and Buck, 1995, Twohy et al., 1997, Corsmeier et al., 2001, Drüe and Heinemann, 2007).
As the previous standard Lyman Alpha sensor is not available any more and is therefore being replaced by the airborne research groups, different other fast humidity sensors come up. A similar system is the Krypton hygrometer KH20 of Campbell Scientific, USA,

https://doi.org/10.24355/dbbs.084-201906170934-0

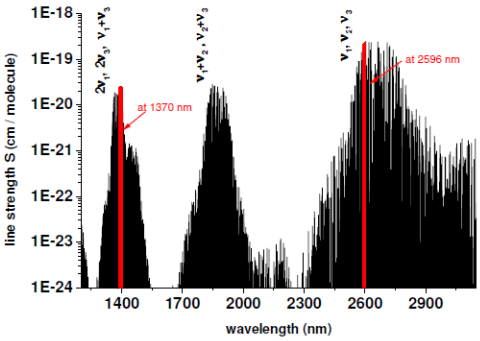

Figure 1.5: Absorption spectrum of water vapour in the wavelength range 1300 to 3000 nm. The absorption lines at 1370 nm and 2596 nm (vertical red lines) are used for the TDLAS technique described by (Buchholz et al., 2013, 2014). Figure from Buchholz (2014).

which, like the Lyman Alpha sensor, has a cross sensitivity to oxygen and therefore has to be calibrated carefully (Foken and Falke, 2012). For the research aircraft of the National Center for Atmospheric Research (NCAR, US), a new Lyman Alpha sensor was built up, which showed promising first results (Beaton and Spowart, 2012).

For large research aircraft, some specifically designed hygrometers are implemented: On the National Science Foundation Gulfstream-V aircraft, a cavity diode laser hygrometer with two absorption lines in the near-infrared is deployed with a temporal resolution of 25 Hz(Zondlo et al., 2010). On the National Aeronautics and Space Administration (NASA) ER-2 aircraft, a specifically designed near-infrared tunable diode laser spectrometer is deployed for measuring atmospheric water vapour concentration (May, 1998), with a sampling rate of 1 Hz and 10% accuracy (Herman et al., 2017). On the High Altitude Long-Range Aircraft (HALO) of the Deutsches Zentrum für Luft- und Raumfahrt (DLR), an innovative TDLAS spectroscopic sensor developed by the Physikalisch-Technische Bundesanstalt (PTB) Braunschweig is deployed (Buchholz et al., 2014).

The humidity sensor of LICOR for measuring fast humidity is based on the absorption of near infrared radiation. It has a longer measurement chamber of 12.5 cm compared to a few mm for the Lyman Alpha. The working principle of the LICOR hygrometer is described in detail in Sect. 4.1.

The LICOR humidity sensors have been used for airborne applications additionally to the Lyman Alpha or to replace the Lyman Alpha for many years (Pillai et al., 2011, Hiller et al., 2014). The sensors have been implemented in various configurations, some facing with the sensor head forward (the helicopter borne sondes Helipod, see Sect. 2.2, and the Airborne Cloud Turbulence Observation System ACTOS, Schmeissner et al., 2015), some with the sensor head oriented vertical (French Piper Aztec), some with an open housing (Siebert et al., 2013), some with a metal grid (Helipod), some with additional purging

https://doi.org/10.24355/dbbs.084-201906170934-0

with synthetic air to keep the detector free of water vapour (Schmitgen et al., 2004).
The manufacturer warns in the manual that the sensor should not be applied with vibrations around 150 Hz and the harmonics (Licor, 2014). However, the impact on measurement results is not quantified. As the LICOR sensor is currently the cheapest fast-response water vapour sensor commercially available and small enough to be easily integrated into aircraft, its airborne applications will very likely increase.
Compared to the LICOR sensor, the tunable diode laser hygrometer can be operated much faster and with a known accuracy, providing the most precise humidity values available to date (Buchholz et al., 2013, 2014).
The suitability of the LICOR sensor for measuring airborne humidity fluctuations is investigated in Sect. 5.4.

1.3.3 State of the art meteorological UAS

The use of unmanned aerial systems (UAS), known as well as the similarly used terms unmanned aerial vehicles (UAV), remotely piloted aircraft systems (RPAS), or drones, has become a widespread method for meteorological research. After a few very early applications (Konrad et al., 1970), the first atmospheric research groups started using unmanned systems in the 1990ies (Holland et al., 2001). Since then there has been a revolution concerning functionality, size and complexity of even commercially available airborne systems, autopilots, and the corresponding hardware and software. Nowadays, UAS cover a broad range of meteorological research fields. The smallest systems (e.g., Reuder et al., 2009), with a weight below or only slightly exceeding 5 kg, are mainly equipped with basic meteorological sensors for humidity and temperature. They are used comparable to a recoverable radiosonde (Soddell et al., 2004). Some provide additional measurements of further parameters, e.g. the ozone concentration (Illingworth et al., 2014).
For determining the 3D wind speed, a multi-hole probe together with a Global Navigation Satellite System (GNSS) receiver and an Inertial Measurement Unit (IMU) are implemented (van den Kroonenberg et al., 2008, Thomas et al., 2012, Wildmann et al., 2014a). Other systems use specific flight patterns and assumptions to provide an estimate of the wind speed and direction with an accuracy of $1\,\mathrm{m\,s^{-1}}$ (Holland et al., 1992, Cassano et al., 2016), and of turbulent fluxes of sensible and latent heat (Dias et al., 2012, Bonin et al., 2013). The UAS Meteorological Mini Unmanned Aerial Vehicle (M^2AV), described in Sect. 2.3, belongs to this size and weight class.
Several systems with an overall takeoff weight between 5 and 25 kg rely on miniaturized sensors for measuring additionally aerosol properties. A mixing condensation particle counter in combination with a three-wavelength absorption photometer and chemical sampling has been used by Bates et al. (2013). Another system includes measurements of longwave and shortwave broadband radiation, aerosol concentration and size distribution, as well as a video camera (de Boer et al., 2016).
The systems have been deployed to study atmospheric processes worldwide at different locations. Bates et al. (2013) report on measuruements at Ny-Ålesund, Svalbard, for studying long-range transport of aerosol particles into the Arctic, and especially the sources of black carbon (BC). The system of de Boer et al. (2016) has been developed to study Arctic haze properties in the Alaskan Arctic. Further, applications to perform measurements in thunderstorms and tornadic supercells have been reported (e.g., Elston et al., 2011).

https://doi.org/10.24355/dbbs.084-201906170934-0

Other UAS with combustion engines provide the capability of long-range flights, as far as permitted by the authorities. Therefore they are mostly deployed above sparsely inhabited areas. Such systems have been operated for up to 30 h per flight in the Arctic (Curry et al., 2004), Antarctic (Cassano et al., 2016) and e.g. above the Indian Ocean (Ramanathan et al., 2007). In addition to meteorological sensors, surface properties are monitored by remote sensing, like the ice cover, type of sea ice and surface temperature (Curry et al., 2004). The UAS ALADINA, which is described in detail in Sect. 2.4, is similar in size and application.
The simultaneous use of more than one UAS has been reported by e.g. Ramanathan et al. (2007), who coordinated three aircraft measuring aerosol concentration, soot and radiation related to clouds. UAS operation with two aircraft following different flight patterns to combine the best measurement strategy was performed as well in the study of Platis et al. (2015) described in Sect. 5.5. A recent overview over UAS applied for meteorological research and their instrumentation is provided by Elston et al. (2015) and Villa et al. (2016).

1.4 Outline of the Treatise

The treatise combines the different fields that are subject to investigation by the work group "Airborne Meteorology and Measurement Techniques" at the Institute of Flight Guidance, TU Braunschweig. The manuscript shows documented examples of capabilities and performances by using the currently available platforms, sensors, and methodology, and addresses limitations which should be overcome in the future. The work is structured as follows: After the general introduction to the manifold topics in the current Chapter 1 above, the different platforms, their capabilities for meteorological campaigns and their measurement equipment are presented in Chapter 2. The methods used for data treatment are presented in Chapter 3. Some specific sensors that have been studied in detail and have been used for meteorological applications are described in Chapter 4. A scientific analysis and discussion of five atmospheric case studies are given in Chapter 5. The final Chapter 6 concludes with an outlook on future requirements for experimental research at the interface of meteorology and engineering, the potential of UAS in fundamental meteorological research, and the need for careful choice of the appropriate platforms and sensors for each application.
Finally it should be underlined that the results presented in this treatise, for both scientific and technical aspects of this work, have already been published in peer reviewed journals (see bibliography section, own publications in bold letters).

https://doi.org/10.24355/dbbs.084-201906170934-0

2 Carrier Platforms (P)

In this chapter the different platforms with their performances and specific sensors are described that have been used during the field experiments presented in this treatise.

2.1 Research aircraft Dornier Do128 D-IBUF - P1

2.1.1 History and instrumentation Do128

The research aircraft Do128-6 with call sign D-IBUF was the first aircraft for polar research in Germany since the Second World War ("Polar 1"). It is a twin-engine turboprop aircraft with tail wheel. Measurement campaigns and logistic flights in the Antarctic were performed in 1983/84. As the polar aircraft was replaced with a larger Do-228 aircraft with longer endurance, the Institute of Flight Guidance of the TU Braunschweig purchased the Do128-6 in 1986 for different research topics in the field of flight mechanics, flight guidance, and boundary layer meteorology (Hankers, 1989, Corsmeier et al., 2002, Bange et al., 2002, 2006, Drobinski et al., 2013, Ducrocq et al., 2013).

A nose boom at the front contains the meteorological sensors to probe the undisturbed air (Corsmeier et al., 2001). The temperature is measured by two complementary sensors, which are combined by high- and low pass filtering techniques: The slow, but highly accurate Rosemount (US) DB102 temperature sensor, and the Rosemount EL102 sensor with fast response time. The temperature sensors are mounted in a sophisticated Rosemount inlet to obtain directly the static air temperature (Stickney et al., 1994), and can additionally be heated (Hankers, 1989).

For measuring humidity, three different measurement principles are used: A capacitive Vaisala Humicap HMP233, Finland, a dew point mirror TP 3-S of Meteolabor, and a Lyman-Alpha optical sensor L-6 / HMS-2 of Buck Research, US. The humidity sensors have a joint heatable inlet, and other parameters like temperature and pressure are recorded for the humidity channel as well. The available humidity sensors on the IBUF have been compared to additional measurements with an airborne cavity ring-down spectrometer (CRDS) for stable isotope composition of water wapour, a customized Picarro L2130-i (Sodemann et al., 2016). The best agreement was found for a combination of the Lyman-Alpha and humicap sensors. The combination of Lyman-Alpha and dew point mirror showed a bias under very dry conditions (Sodemann et al., 2016).

With the heatable multi-hole probe of Rosemount, connected with very short tubes to the pressure transducers of Setra, US, the static and dynamic pressure, as well as the airflow angles are retrieved in the aircraft-fixed coordinate system, which are related to the rotation angles, the angle of attack α and the angle of sideslip β (Boiffier, 1998). The high resolution data of the position and attitude reference system are provided by the inertial measurement unit (IMU) Honeywell Lasernav, US, and the newer iNAV-RQH-1003 of iMAR, Germany, which are integrated into the cabin, and GPS (NovAtel OEM-V, now

https://doi.org/10.24355/dbbs.084-201906170934-0

Figure 2.1: The research aircraft Do128-6 D-IBUF (left) and the nose boom with meteorological sensors (right): multi-hole probe, pressure transducers, temperature sensors, and humidity channel.

additionally a NovAtel GPS OEM-6, Canada).
A radio altimeter operating at altitudes up to 2500 ft is located in the middle of the cabin floor. A Heimann infrared KT15 sensor, Germany, to determine the surface temperature is integrated in the bottom of the cabin.
Additional instrumentation can be integrated depending on the application. For instance, more sensors for wind measurements can be installed at the wing tips and at the vertical tail. Air chemistry sensors and a drop sonde system have been used (Corsmeier et al., 2002), as well as a sensor for real-time processing of water vapour isotopic composition (Sodemann et al., 2016). For the humidity intercomparison flight discussed in Section 5.4, three additional LICOR humidity sensors presented in Section 4.1 were integrated into the aircraft. A laser scanner and cameras in the visible and infrared wavelength range have been deployed for various projects. Also for the flights around wind parks (Sect. 5.3), additional optical sensors were installed, namely two downward looking cameras, for the visible range the MV1D1312-G2 of Photonfocus, Switzerland, and for the infrared range the A35SC of FLIR, Germany, and a scanning laser VZ-1000 of Riegl, Germany, for deriving sea surface parameters.

2.1.2 Operation Do128

With the low cruising airspeed of 60 to 70 $\mathrm{m\,s^{-1}}$, the Do128 is particularly suitable for high resolution meteorological research within the ABL, although it is possible as well to fly up to an altitude of 7000 m with additional oxygen for the crew. The non-pressurized cabin allows a straightforward modification for additional sensors, which have to undergo the process of airworthiness certification, including e.g. the proof of mechanical stability and electromagnetic compatibility. The Pratt and Whitney, US, turbines are rather quiet, making the airplane attractive for e.g. flights at low altitudes to test the landing procedures of airports. In Lower Saxony, the Institute of Flight Guidance had the permanent permit to fly as low as 150 m above uninhabited terrain even before 2017, when this was generally defined as the minimum flight altitude. For particular missions, a permit to fly at very low altitudes can be requested. Altitudes as low as 60 m have been granted above the North Sea to investigate the far field effects of wind parks and the impact on local

https://doi.org/10.24355/dbbs.084-201906170934-0

climate (Emeis et al., 2016, Platis et al., 2018), and measurements several meters above the frozen Baltic Sea have been performed (Brümmer et al., 2002).
Flights under instrument flight rules (IFR) are possible with the meteorological measurement equipment. Meteorological research flights into icing conditions and into convective storm clusters have been done by Groenemeijer et al. (2009).
In this treatise, flights with the Do128 are presented which were conducted in the far field downstream of offshore wind parks (Sect. 5.3), and for an intercomparison flight of different fast response humidity sensors (Sect. 5.4).

2.2 Helipod - P2

2.2.1 History and instrumentation Helipod

The helicopter borne meteorological sonde "Helipod" was developed by Aerodata, Germany, on behalf of TU Braunschweig and the Leibniz University Hanover in 1992, funded by the Federal Ministry of Education and Research, Germany. It was operated by the Institute of Aerospace Systems, TU Braunschweig, from 1994 to 2012 (e.g., Bange and Roth, 1999, Bange et al., 2002, Martin and Bange, 2014), and by the Institute of Flight Guidance since 2013 (Lampert et al., 2018a). Helipod was designed to probe the atmospheric dynamics with high accuracy and minimal disturbance. It does not have wings nor an own propulsion, and has a small, aerodynamically formed fuselage with a length of about 5 m and a width of 0.6 m. The overall weight is 320 kg. Helipod samples the atmosphere autonomously, without the need of external power supply. Recording commands can be given from the onboard operator via telemetry.
Helipod is equipped with sensors for atmospheric dynamics, similar to the IBUF instrumentation (see Sect. 2.1): The same multi-hole probe and corresponding pressure transducers of Setra, US, are implemented for determining the air flow angle. A GPS system with eight receivers for a full 3D attitude alignment (GNATTI System of Geo++ GmbH, Germany) and IMU (LITEF LCR 88, Germany) are used for the wind vector calculation according to Sect. 3.2. The temperature is measured complementary with high accuracy by a Rosemount Pt100 element and with fast response time by a Dantec fine wire sensor. Humidity measurements are performed with a Lyman Alpha sensor of Buck Research, US, a capacitive Vaisala HMP110, Finland, a dew point mirror 1011B of General Eastern, US, and a LICOR LI-7500, US, which measures carbon dioxide as well (see further description in Sect. 4.1). A Heimann KT19 infrared sensor records the surface temperature. Altitude information up to at least 1500 m and with 0.5 m resolution is provided by a radar altimeter. Further, a LICOR LI-7700 methane sensor of the cooperation partner Prof. Dr. Torsten Sachs, leader of the Helmholtz Yound Investigator Group TEAM (Trace Gas Exchange in the Earth-Atmosphere System on Multiple Scales) at the German Research Centre for Geosciences (GFZ) was included for the measurements in 2014.
The data is recorded with different data acquisition rates. The air flow angles, fast temperature, humidity (Lyman-Alpha) and attitude information is available at 500 Hz, which enables to determine a true resolution of 100 Hz after applying anti-aliasing filters. The LICOR systems provide data at a maximum frequency of 20 Hz. GPS data are available at 10 Hz resolution. In the post processing, the data of different sensors are combined by complementary filtering (see Sect. 3.1).

https://doi.org/10.24355/dbbs.084-201906170934-0

Figure 2.2: The meteorological probe Helipod.

2.2.2 Operation Helipod

The Helipod can be towed by almost any helicopter. Operation is possible under visual flight rules (VFR) only. With an air speed of $40\,\mathrm{m\,s^{-1}}$, a rope of 15 m length allows to operate the Helipod without influences of the rotor downwash for a standard helicopter with two turbines (e.g. AS350). For larger helicopters, like the Russian Mi8, a rope length of 30 m is suitable for operation at the same air speed. After take-off of the helicopter, the Helipod is attached via the rope. No power supply from the helicopter is necessary. Two onboard car batteries in series provide power for around 4 h of measurement. Data are uploaded to the operator onboard the helicopter via telemetry, and stored on the board computer. When pickung up speed, Helipod turns into the direction of flight.
Before touching the Helipod during the landing, the system has to be grounded. The Helipod is treated as an external load. In contrast to the payload integrated into the Do128, no airworthiness certification is necessary.
The pendulum frequency of the Helipod under the helicopter depends on the length of the rope. For the 15 m rope used for smaller helicopters, a main oscillation period of around 8 s plus harmonics, and a bank oscillation period of around 1 s have been reported (Bange and Roth, 1999). This does not affect the wind vector calculation (Sect. 3.2). An intercomparison flight of the Helipod and the Do128 showed a good agreement for flux calculations (Sect. 3.4) at the same altitude, and therefore confirms the high quality and reliability of both systems (Bange et al., 2006).
In this treatise, Helipod data obtained during a mission in the Lena River Delta, Siberia, are presented in Sect. 5.4.

https://doi.org/10.24355/dbbs.084-201906170934-0

Figure 2.3: The M^{2}AV flying close to the meteorological tower at Lindenberg in 2011.

2.3 Meteorological Mini Aerial Vehicle - P3

2.3.1 History and development M^{2}AV

The Meteorological Mini Aerial Vehicle (M^{2}AV) was developed at TU Braunschweig, Institute of Aerospace Systems, under the guidance of Dr. Jens Bange, now professor at University of Tübingen, and Prof. Dr.-Ing. Peter Vörsmann. It was constructed and built by the company Mavionics GmbH, Germany. It was one of the first meteorologically equipped automatic UAS worldwide, and it was the first UAS capable of determining the 3D wind vector (Spiess et al., 2007, van den Kroonenberg et al., 2008) and therefore allowing to calculate turbulent fluxes (Martin et al., 2014). The widespread use of UAS, and particular of the M^{2}AV, became possible with the development of small-size and light-weight GPS and IMU sensors, which do fit the challenging space and weight constraints.
The concept of the M^{2}AV is the base for other meteorological UAS developments: At TU Braunschweig, ALADINA is now a larger UAS with more payload capacities (Sect. 2.4), at Tübingen University, the Multi-Purpose Airborne Sensor Carrier (MASC) with similar dimensions to the M^{2}AV is used for various meteorological applications (Wildmann et al., 2014a, Platis et al., 2015).

2.3.2 System M^{2}AV

The M^{2}AV is an unmanned aerial vehicle based on the aircraft type “Carolo T200” with a wing span of 2 m and a weight of 6 kg (Fig. 2.3). It is composed of epoxy-glass resin and does not have a landing gear, resulting in a low total weight. To leave the nose free for undisturbed measurements, the aircraft is powered by a twin-engine system, therefore the “T” in the denomination. It is operated with electrical batteries. Compared to combustion motors, this provides the advantages of less vibrations and a constant center of gravity during the flight. The typical cruising speed is 22 m s^{-1}, the endurance about 50 min.
In the front compartment, there is space for the payload of around 1 kg, incluing batteries

https://doi.org/10.24355/dbbs.084-201906170934-0

and the autopilot system. The batteries are located at the rear side of the fuselage. They are removed for charging after each flight, and exchanged quickly if a next flight is planned immediately.

2.3.3 Operation M²AV

The M²AV is started and landed remotely piloted. For launching, a bungee rope is applied on grass (van den Kroonenberg et al., 2008). For applications in cold conditions, like on Antarctic snow and sea ice surfaces, starting with a winch is possible as well (Jonassen et al., 2015), and is preferred due to the loss of elasticity of the bungee rope. The M²AV lands directly on its fuselage. A smooth surface like flat grass or snow is required with dimensions of approximately 25 x 60 m, depending on the wind conditions and the pilot's capabilities.
The system can be fully controlled during the mission by an autopilot system. The autopilot in use for the measurement campaigns presented here is the MINC (Miniature Integrated Navigation and Control System) with a total weight of 50 g, developed by the company Mavionics. It combines IMU measurements in three directions, the GPS signal and static and dynamic pressure measurements to determine attitude, position, altitude and air speed (Martin et al., 2011). The MINC autopilot follows pre-defined waypoints approximated by user-defined cubic splines, which can be updated by a telemetry link from the mission control ground station during the flight. The accuracy necessary for the 3D wind is achieved by the autopilot flying precise straight and level legs. The standard deviation of altitude is in the range of typically 1 m for flight legs of 3 km length (Martin et al., 2014). The lateral deviation of the aircraft from the planned trajectory is normally in the range of ±2 m, but may be as large as ±10 m for harsh gusty conditions (van den Kroonenberg et al., 2008). The reliability of the autopilot enabled the successful deployment of the UAS outside the line of sight above Antarctic sea ice at altitudes as low as 15 m.
For operation in Germany, limitations are imposed by the civil aviation agency (CAA). Getting a flight permission for systems with weight between 5 and 25 kg involved the aviation authorities of the federal states of Germany until April 2017. Above 25 kg, an airworthiness certification is necessary, and getting a flight permission is much more complicated (only in restricted airspace, operated by a certified pilot). For UAS below 25 kg deployed for research purposes, flights were only allowed under visual control of a safety pilot until April 2017, which means within a radius of around 1 km depending on visibility conditions, and excluding flights into clouds. For flight legs of 3 km length, an operation with two safety pilots handing over the responsibility of surveilling the system has been practised (Martin et al., 2014). Flight permissions up to an altitude of 1500 m have been granted for individual meteorological research projects. Until April 2017, a flight permission had to be requested with the written agreement of the owner or leaseholder of the property where the flights were planned, the local police or other regulatory authority, and the nature protection agency. Furthermore, documents about insurance, the UAS technical data and pilot training were required. A declaration of the safety pilots was needed to ensure that no personal data would be collected. Upon approval, a NOTAM (Notice to Airmen) was issued to warn pilots about the UAS activities. The beginning

https://doi.org/10.24355/dbbs.084-201906170934-0

and end of the flight activities for each day have to be communicated to air traffic control, and a responsible person has to be available at the phone for the duration of the missions. UAS flights above inhabited areas are normally not allowed for scientific research. The new regulations are presented in Sect. 6.1.5, but were not applicable to the flights presented here.

The M^2AV has been deployed for high resolution atmospheric profiling (Martin et al., 2011, Jonassen et al., 2015) and for deriving turbulent parameters (van den Kroonenberg et al., 2012, Martin et al., 2014, Martin and Bange, 2014) worldwide at various locations. In this treatise, M^2AV data are analysed for a case study of the nocturnal low-level jet in Southern France and its impact on turbulence properties, which is presented in Sect.5.2.

2.4 ALADINA - P4

2.4.1 Development and cooperation ALADINA

The author's idea to develop a somewhat larger UAS than the M^2AV, meteorologically equipped and expanded with more payload capabilities, was born as in aerosol research, it is very helpful to study not only aerosol properties on ground, but local profiles and vertical distributions of particles within the atmospheric boundary layer. The project ALADINA (Application of Light-Weight Aircraft for Detecting In situ Aerosol) was funded by several research grants of the German Research Foundation (grants no. LA 2907/5-1, 5-2 and 5-3), with the project partners Prof. Dr. Alfred Wiedensohler, Dr. Birgit Wehner and Dr. Markus Hermann of the Leibniz Institute of Tropospheric Research (TROPOS) providing the expertise of miniaturisation and calibration of aerosol sensors, as well as many years of experience with the analysis of aerosol measurements, and the group of Prof. Dr. Jens Bange, University of Tübingen, contributing with years of experience of operating meteorological sensors on UAS gained with the M^2AV (see Sect.2.3) and the newer systems MASC.

2.4.2 System ALADINA

ALADINA (Fig.2.4) is based on the "Carolo P360" aircraft, which was developed and built by Andreas Scholtz at the Institute of Aerospace Systems, TU Braunschweig (Scholtz et al., 2011). It is made of epoxid resin and has a wingspan of 3.6 m. The pusher aircraft (therefore the P in the denomination) with the propeller at the rear of the fuselage is operated with electric accumulators. Two large lithium polymer (LiPo) batteries in series, with a capacity of 21 Ah each, provide power for a flight time of around 40 min. For aerosol observations, it is even more critical to avoid own pollution by a combustion motor than for the purely dynamic meteorological measurements of the M^2AV. The maximum take-off weight can be up to 25 kg with a payload up to 4.5 kg. In contrast to the M^2AV, ALADINA has a landing gear. The cruising speed is $28\,m\,s^{-1}$.
The P360 was specifically designed to carry relatively large and heavy payload compared to other UAS. The front compartment with dimensions of 0.35 x 0.31 x 0.19 m allows the integration of "bulky" sensors (Fig.2.5). The form of the P360 can be adapted easily, e.g.

https://doi.org/10.24355/dbbs.084-201906170934-0

Figure 2.4: ALADINA measurement flight in Melpitz near Leipzig, Germany.

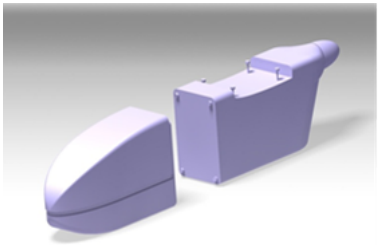

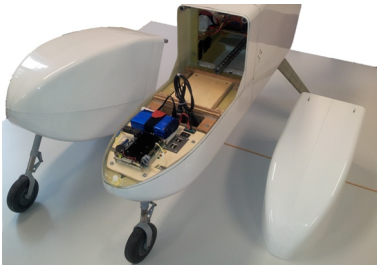

Figure 2.5: The front compartment of the P360 is designed for the integration of payload, and can be removed easily (Scholtz et al., 2011).

the fuselage can contain a bottom opening for cameras, and the nose can be modelled according to the needs of the sensor integration (Scholtz et al., 2011).

2.4.3 Operation ALADINA

The operation of ALADINA involved the same procedure for obtaining a flight permission as described for the M^2AV (see Sect. 2.3.3) until April 2017. ALADINA can take off and land not only on soft grass and snow surface, but on gravel and asphalt as well. An airfield with dimensions of about 25 x 60 m is necessary, depending on the wind conditions, surface properties and pilot's skill. The stalling speed is around $17\,m\,s^{-1}$. Near this speed, especially banked turns are critical for stall due to the large fuselage.
ALADINA was originally equipped with the Research Onboard Computer System (ROCS) autopilot of the Institute of Flight Mechanics and Control of Stuttgart University (Haala et al., 2011), which was used successfully for the MASC aircraft as well (Wildmann et al., 2014a). Similar to the MINC autopilot, waypoints can be updated during the flight within the telemetry range of around 1.5 km. The flight mission can be monitored and

https://doi.org/10.24355/dbbs.084-201906170934-0

modified on a laptop computer. Starting in 2017, the open source autopilot Pixhawk 2 is now deployed.
Data are transmitted to the ground station at a rate of 1 Hz to allow continuous monitoring of the sensors, and to adapt the flight strategy to the current meteorological conditions. This is a major improvement compared to the M^2AV, where data are only available after the flight.
The ALADINA meteorological payload was re-designed based on experiences during flight campaigns. The setup of the new sensor system (Bärfuss et al., 2018) is described in Sect. 4.2.
In this treatise, ALADINA observations during several measurement campaigns at the aerosol monitoring station Melpitz near Leipzig, Germany, are presented in Sect. 5.5.

2.5 Quadrocopter ALICE - P5

2.5.1 Development and instrumentation ALICE

For operation in sea ice conditions, it turned out to be difficult to operate a fixed-wing UAS with the necessity to prepare a sufficiently large smooth landing strip on ice. For some applications, easy handling during take-off and landing is more important than having a turbulence probe on board. This led to the idea of developing a quadrocopter system with payload capacity for meteorological sensors and additionally taking air samples. The samples can later be analysed in the laboratory. In the project ALICE (Airborne tool for methane isotopic composition and polar meteorological experiments), such a quadrocopter was realized and equipped with payload at the Institute of Flight Guidance. The quadrocopter itself has a maximum diameter of 1160 mm without propeller blades, 1820 mm including the propeller blades, a height of 780 mm and a maximum weight of 24.9 kg. Technical details were adapted to meet the needs of polar missions. E.g. the thermal insulated batteries can be easily removed from the system, as they need to be heated and transferred to the mission site in heated containers. The performance of ALICE up to an altitude of 1000 m has been demonstrated. The system has been operated successfully up to a wind speed of $18\,m\,s^{-1}$. For improving safety of persons and equipment on the ground, the emergency parachute system ST160 of Opale Parachute, France, with a weight of 1020 g has been implemented.
Different meteorological sensors are integrated into the system: For recording temperature, a HMP110 of Vaisala, Finland, is used, a digital temperature sensor TSYS01 of Innovative Sensor Technology (IST), Switzerland, two Pt100 elements, and two self-fabricated finewire sensors. For measuring humidity, the HMP110 of Vaisala is used, and the Rapid P14 of IST. Further, twelve glass bottles are included. They are evacuated before the flight. An electromagnetic valve can be opened and closed again via remote control to take air samples at different altitudes. The air samples are analysed to derive the methane isotopic composition and thus provide information on the origin of atmospheric methane. ALICE and the payload are shown in Fig. 2.6.

2.5.2 Operation ALICE

The quadrocopter ALICE was operated during the Polarstern cruise PS109 (ARK-XXXI/4) from Tromsø to Bremerhaven from 12 September to 13 October 2017 (Kanzow, 2018). The

https://doi.org/10.24355/dbbs.084-201906170934-0

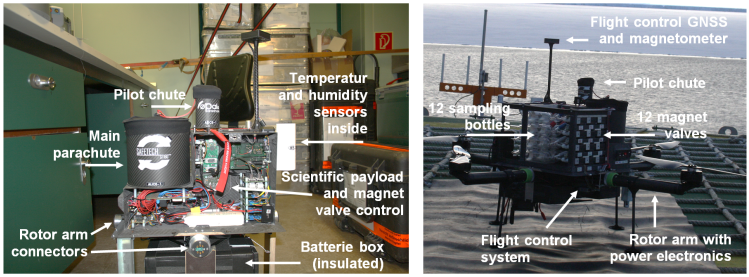

Figure 2.6: The quadrocopter ALICE with its payload for air sampling and meteorological measurements.

destination was the sea ice east of Greenland. ALICE was deployed in cooperation with the work group of Dr. Ellen Damm of the Alfred Wegener Institute of Polar and Marine Research, performing biogeochemical analyses of sea ice and ocean. Valuable experience was obtained during the cruise (Kanzow, 2018), including logistical challenges of obtaining a flight permission for takeoff and landing on the Polarstern helideck, and the coordination with air traffic control in Danish controlled air space. Procedures for UAS operation on the ship were established, and the helideck was recognised as a resource to be distributed among UAS operating crews and the helicopter crew. The autopilot and telemetry were tested in the magnetically and electromagnetically disturbed surrounding of the vessel, the unfavourable polar Earth's magnet field characteristics and the highly unfavourable positioning satellite constellation in polar regions. The Pixhawk2 autopilot was able to operate reliably despite the error in the Earth magnetic field induced by the vessel. During manual takeoff, a re-alignment of the magnetic system was done. The mass efficient passive thermal insulation of the batteries and the measurement system were rated as very appropriate. The data availability was 100%. Prior to the campaign, tests were performed in the climate chamber of IFF down to -40°C. Further, during the tests under cold conditions, the vibrations with amplitude and frequency determined for ALICE inflight conditions were applied with a shaker. Nevertheless, in the harsh Arctic conditions, a major problem was the leak tightness of the plastic valves in the glass bottles for air sampling.
As the first observational data obtained with ALICE are still being processed, only preliminary results are shown in Sect. 6.1 to demonstrate the potential of this measurement system.

https://doi.org/10.24355/dbbs.084-201906170934-0

3 Methods for signal processing

To derive the meteorological parameters with best possible accuracy for the boundary layer studies, different mathematical methods are used. They are explained briefly in this chapter.

3.1 Complementary filtering technique

Generally, time series of any measurement signals can be decomposed into oscillations at various frequencies. Additionally to the signals of interest, there may be contributions of mechanical oscillations of the whole system, as well as white noise. Certain frequencies can be eliminated from the signal by applying filtering techniques. The high pass filter removes oscillations with a frequency lower than the predetermined cutoff frequency, and the low pass filter attenuates oscillations with a frequency higher than the cutoff frequency. For the studies presented here, sensors with different temporal behaviour are combined by complementary filtering: The relatively slow, but accurate and long-term stable sensors were low pass filtered, and the relatively fast sensors with less reliable absolute values were high pass filtered with the same cutoff frequency. E.g. for complementary filtering of humidity sensors, a cutoff frequency of 1 Hz is suitable to combine the signal of the fast sensors (Lyman Alpha and LICOR) and of the slow capacitive humidity sensor or dew point mirror (see Sect. 5.4). This can be done with a Butterworth filter of 1st order. In MATLAB, the function "filtfilt" serves to provide filtered signals without phase shift (Oppenheim et al., 1999).

The method of complementary filtering is illustrated in Fig. 3.1. In this case, the air temperature is measured onboard ALADINA by two sensors, the fast fine wire and the slow TSYS01 sensor (see Sect. 4.2). The signal of the slow sensor is first corrected by applying the inverse transfer function, assuming a transfer function of first order (called reconstruction function in Fig. 3.1). This is done to remove phase lag induced by the heat capacity of the sensor. Then, high- and low-pass filtered data are combined. The cutoff frequency should be lower than the cutoff frequency of the assumed first order system for the reconstruction filter to avoid amplification of noise. The sensor response times can be estimated by comparing ascents and descents, which should provide the same temperature profiles, but differ due to the sensor transfer functions (see example in Fig. 3.2). The method of Tagawa et al. (2003) estimating thermal time constants in the frequency domain was successfully applied to ALADINA temperature data (Bärfuss et al., 2018). However, the method requires an overlap of the signals in a broad and reliable frequency range. For humidity data based on capacitive sensors, the method does not provide plausible time constants, as each sensor has different time constants for increasing and decreasing humidity.

An example of retrieving the complementary filtered temperature is given in Fig. 3.2. The vertical profiles of temperature for a consecutive ascent and descent are shown for different

https://doi.org/10.24355/dbbs.084-201906170934-0

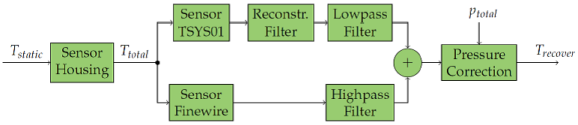

Figure 3.1: Flow chart demonstrating the principle of the complementary filtering and reconstruction technique. In this example, temperature is measured with the slow, but accurate sensor TSYS01, and the fast fine wire. Figure from Bärfuss et al. (2018)

sensors, the slow TSYS01 and HMP110 sensors and the fast fine wire sensor. In the profiles of the slow sensors, a hysteresis effect caused by the response time is visible. The combined signal after complementary filtering was calculated from TSYS01 and fine wire sensor. The static air temperature can be derived from measuring the stagnation point temperature by correcting the time lag effect and the total temperature effect as described in Stickney et al. (1994) using individual coefficients for the UAS. The static air temperature T_{static} is calculated from the measured total temperature T_{total} with the following formula:

$$\frac{T_{total}}{T_{static}} = 1 + \frac{\gamma - 1}{2} Ma^2 \tag{3.1}$$

Here, $\gamma = 1.4$ is the ratio of the heat capacity at constant pressure and the heat capacity at constant volume, and Ma is the Mach number. Further parameters like the dry potential temperature can then be calculated according to Stull (1988).

https://doi.org/10.24355/dbbs.084-201906170934-0

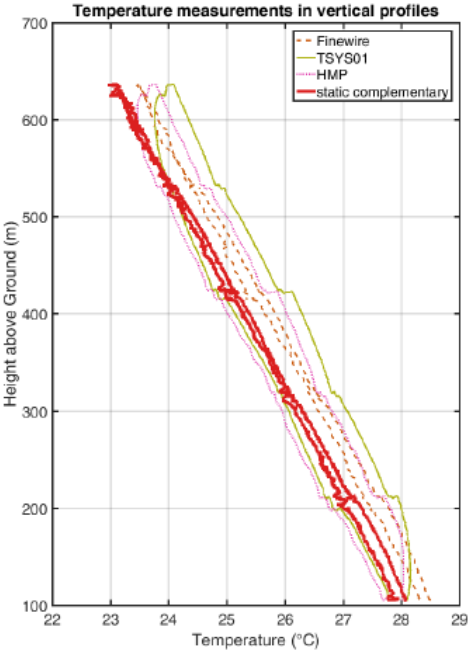

Figure 3.2: Temperature profiles of consecutive ascent and descent: the slow TSYS01, the fast fine wire, the slow HMP110, and the complementary signal of TSYS01 and fine wire. Figure from Bärfuss et al. (2018)

3.2 Wind vector derivation

For wind vector measurements, the validity of Taylor's hypothesis of frozen turbulence is applied, which assumes that the eddies are sampled faster than they decay (Taylor, 1938). The wind vector $\vec{v} = (u, v, w)$ in the meteorological coordinate system (East-North-Up positive) can be determined as following: The 3D wind vector $\vec{v}_g$ in the geodetic coordinate system is the reason for the vector difference between the ground speed $\vec{v}_{gs}$ (in the geodetic coordinate system, oriented as North-East-Down positive, Luftfahrtnorm, 1970) and the air flow vector $\vec{v}_a$ (observed in the aerodynamic coordinate system).

$$\vec{v}_g = \vec{v}_{gs} + \vec{v}_a \tag{3.2}$$

The air flow vector has to be transformed into the geodetic coordinate system, and can be written as the vector sum of the true airspeed $\vec{v}_{tas}$ and the cross product of the vector

https://doi.org/10.24355/dbbs.084-201906170934-0

of angular momentum rates $\vec{\Omega}$ and the lever arm vector $\vec{s}$ describing the vector between the location of the multi-hole probe measurements and the origin of the aerodynamic coordinate system:

$$\vec{v}_g = \vec{v}_{gs} + \underline{M}_{fa}\underline{M}_{gf}(\vec{v}_{tas} + \vec{\Omega} \times \vec{s}) \tag{3.3}$$

According to Lenschow (1972), $\vec{\Omega_g}$ can be represented as:

$$\vec{\Omega_g} = \begin{bmatrix} -\dot{\Theta} \cdot sin\Psi + \dot{\Phi} \cdot cos\Theta \cdot cos\Psi \\ \dot{\Theta} \cdot cos\Psi + \dot{\Phi} \cdot cos\Theta \cdot sin\Psi \\ \dot{\Psi} - \dot{\Phi} \cdot sin\Theta \end{bmatrix} \tag{3.4}$$

with $\dot{\Theta}$, $\dot{\Phi}$ and $\dot{\Psi}$ the temporal derivatives of the Eulerian Angles. The true airspeed $\vec{v}_{tas}$ is calculated from the total pressure at the front hole measured against the static pressure port. The matrix $\underline{M}_{fa}$ describes the transformation from the aerodynamic into the aircraft-fixed coordinate system. For this, the angles of attack α and sideslip β are needed, which are derived from the pressure difference measured between the upper and the lower holes, and the left and right holes of the multi-hole sonde, respectively. The matrix $\underline{M}_{gf}$ describes the rotation from the aircraft-fixed into the geodetic coordinate system. Here, the Eulerian angles pitch Θ, bank (roll) Φ and yaw (heading, azimuth) Ψ are required. Detailed calculations for the three wind components can be found in e.g. Vörsmann (1985). Finally the wind vector has to be transformed from the geodetic (North-East-Down positive) to the meteorological coordinate system.

Altogether, the wind vector is determined by the subtraction of two vectors with large absolute values compared to the wind vector itself. A high accuracy and careful calibration of all measured data, including the angles needed for the transformation matrices between the different coordinate systems, are required to achieve acceptable error bars for straight flight legs in the range of below $0.5\,\mathrm{m\,s^{-1}}$, as shown in Pätzold (2017).

The successful application of the method for unmanned aircraft has been demonstrated by van den Kroonenberg et al. (2008). For calculation of the 3D wind vector for UAS, the lever arm vector in Eq. 3.3 is quite small and can be neglected (van den Kroonenberg et al., 2008). The plausibility of the wind vector can be checked by specific flight patterns like boxes, where the wind vector should not depend on flight parameters (Bärfuss et al., 2018). However, turns are usually excluded for calculating the wind vector. For high angles of attack and sideslip ($> 20\ ^\circ$), the multi-hole probes are not calibrated. Further, the retrieval of correct flight attitude may contain larger errors during highly dynamic maneuvers depending on INS algorithms (Hinüber et al., 2012).

3.3 Turbulence parameters

To derive turbulent fluctuations, a common way is to subtract the mean value from a time series of measurements (so called Reynolds averaging). Also a linear detrending is often applied to remove continuous changes of a parameter, e.g. the increase of temperature during a day. However, the appropriate length of averaging intervals is not always obvious (Martin and Bange, 2014), and the choice of the averaging interval strongly influences the absolute values of turbulence parameters. On the one hand, the time interval has to be long enough to include as well features on larger scales, but on the other hand, they

https://doi.org/10.24355/dbbs.084-201906170934-0

should not be too long to avoid including advection and large scale processes, which are not related to turbulent eddies (Lenschow et al., 1994). Another method for deriving turbulent fluctuations is the high pass filtering of a signal. With this technique, the absolute values of a fast sensor are eliminated, which have usually less accuracy and long-time stability, and only the fast fluctuations with frequencies above the cutoff frequency remain in the signal.
The turbulent kinetic energy TKE can be calculated with the traditional formula of Stull (1988):

$$TKE = \frac{1}{2}(\sigma_u^2 + \sigma_v^2 + \sigma_w^2) \tag{3.5}$$

Here, σ_u^2, σ_v^2 and σ_w^2 indicate the wind variances in the three directions.
The turbulence anisotropy is defined as the ratio of the horizontal to the vertical wind speed variances (Darbieu et al., 2015):

$$A = \frac{\sigma_u^2 + \sigma_v^2}{2\sigma_w^2} \tag{3.6}$$

This can be simplified assuming isotropy in horizontal direction:

$$A = \frac{\sigma_u^2 + \sigma_v^2}{2\sigma_w^2} = \frac{\sigma_v^2}{\sigma_w^2} \tag{3.7}$$

The turbulence parameters TKE and anisotropy ratio can be derived from UAS data: The turbulent kinetic energy TKE is calculated according to Eq. 3.5. A high pass Butterworth filter of third order with a frequency of 0.01 Hz was used to calculate the wind speed variances for the case study presented in Sect. 5.2. Further, isotropy in the horizontal direction was assumed, and the wind variance component parallel to the flight track σ_u^2 was replaced by σ_v^2. This method has been applied for different airborne data sets (e.g., Paluch and Baumgardner, 1989, Gultepe and Starr, 1995, Meischner et al., 2001), with the background that the dynamic behaviour of the pressure sensors can be different in dependence of the orientation to the flight track. Eq. 3.5 can then be written as

$$TKE = \frac{1}{2}(\sigma_u^2 + \sigma_v^2 + \sigma_w^2) = \sigma_v^2 + \frac{1}{2}\sigma_w^2 \tag{3.8}$$

The turbulence anisotropy is calculated according to Eq. 3.7. For the UAS data, the assumption of horizontal isotropy is applied as well ($\sigma_u^2 = \sigma_v^2$). Values around 1 indicate isotropic distribution of turbulence. Values below 1 are expected for conditions of convective mixing with strong fluctuations in the vertical component induced by rising thermals. Values exceeding 1 are attributed to an enhanced turbulence component in horizontal direction, which may be caused by wind shear or suppression of vertical movement due to stable stratification. Other definitions of the anisotropy ratio can be easily compared (e.g., Mauritsen and Svensson, 2007, Canut et al., 2016).
The parameters TKE and anisotropy are used in the study of the impact of the LLJ on turbulence (Sect. 5.2). TKE is further used as a parameter to quantify the strength and extent of far field wakes (Sect. 5.3).
Turbulence is produced at a length scale of several 100 m, depending on the ABL height and thermal stratification (boundary layer depth). The other limit of the inertial subrange

https://doi.org/10.24355/dbbs.084-201906170934-0

is dissipation at a length scale of typically few mm. According to Kolmogorov (1941), the energy density of turbulence decays with a slope of -5/3 for isotropic turbulence. Commonly, the quality of turbulence measurements is verified by analysing the power spectra of the wind components. Assuming isotropic turbulence, the squared data of wind fluctuations multiplied by the frequency f in Hz should follow the $k^{-5/3}$ power law of Kolmogorov (1941), with $k = 2 \cdot \pi \cdot f$.
Power spectra are applied in Sect. 5.4 to revise the quality of turbulent humidity fluctuations.

3.4 Latent heat fluxes

For quantifying moisture transport from the surface into the atmosphere, a commonly acknowledged method is the eddy covariance technique. The turbulent fluxes of latent heat are calculated under the assumption that vertical transport takes place via turbulent eddies. For calculating the latent heat flux, accurate measurements of the fast fluctuations of the vertical component of wind speed and humidity are therefore necessary.
For deriving turbulent fluxes of latent heat, the method of correlation is applied. The latent heat flux E can be calculated according to the following formula:

$$E = L \cdot \rho \cdot \overline{w'm'} \tag{3.9}$$

Here, L is the evaporation heat, ρ the air density, m' denotes the fluctuations of the water vapour mixing ratio and w' the fluctuations of the vertical wind speed component. The term $\overline{w'm'}$ is the cross correlation of the two fluctuations. The latent heat flux is therefore the amount of energy transferred into the atmosphere by turbulent vertical mixing of humid air masses. The eddies transporting the latent heat contain different sizes from the ABL depth down to dissipation, decaying along an energy cascade within the inertial subrange.
The calculation of latent heat fluxes is applied in Sect. 5.4 for flights with the Do-128 and Helipod.

3.5 Eddy dissipation rate

The eddy dissipation rate ϵ is a measure for the decay of the kinetic energy $\mathrm{E}_{kin}(\mathrm{r})=\frac{1}{2}V^2(r)$ of an eddy of size r with the speed $\mathrm{V}=2\pi\cdot\ \mathrm{r}\cdot\tau_r^{-1}$. Here, τ_r denotes the rotation period. Assuming that the kinetic energy of an eddy is dissipated within the rotation period, the eddy dissipation rate can be defined as following:

$$\epsilon = \frac{E_{kin}(r)}{\tau_r} \tag{3.10}$$

https://doi.org/10.24355/dbbs.084-201906170934-0

The eddy dissipation rate ϵ can be calculated from airborne data via the structure function $D_v(r)$, which is a measure of autocorrelation in a flow of wind speed V depending on eddy size. It is defined as in Tatarskii (1971):

$$D_v(r) = \frac{1}{N-n} \sum_{i=1}^{N-n} [V(x_i) - V(x_i + r)]^2 \tag{3.11}$$

Here, x is the spatial coordinate, N is the number of data points, r is the spatial distance corresponding to the eddy size, and n is the number of data points that belong to a distance r. The structure function can be applied assuming local isotropic and homogeneous turbulence within the inertial subrange.
The structure function is related to the turbulent kinetic energy TKE for isotropic turbulence, and can be calculated as well with the following formula, where σ_V is the wind speed variance and ρ_V is the autocorrelation function:

$$D_v(r) = 2\sigma_V^2[1 - \rho_V(r)] \tag{3.12}$$

In the inertial subrange, the structure function is related to the eddy dissipation rate ϵ and the radius r according to Kolmogorov (1941)

$$D_v(r) = \beta\epsilon^{2/3} r^{2/3} \tag{3.13}$$

The Kolmogorov constant β equals 2.
The eddy dissipation rate is used in airborne engineering applications, e.g. research on aircraft wake vortices. Unlike the parameter TKE, it represents a well-defined parameter for atmospheric turbulence, which does not depend on the averaging method and sampling length as explicitly as the TKE. However, in the field of meteorology, TKE is more commonly applied.
In this treatise, mainly TKE is used to quantify turbulence (Sect. 5.2 and Sect. 5.3). The eddy dissipation rate is used in Sect. 5.5 to estimate how long it takes for particles in the residual layer to be mixed down to the surface by only taking into account turbulent eddy transport.

3.6 Synchronisation of high resolution data

The derivation of some meteorological parameters need the combination of different measurements (see for example humidity and wind for latent heat fluxes calculation in Sect. 3.4 above) or with different response times (e.g. temperature or humidity, see Sect. 3.1). Therefore it is essential to synchronize the basic measurements in order to provide nominal accuracies. This can be done by maximizing the covariance of the fluctuations of the signals of the two sensors for various temporal offsets. The time shift resulting in the highest correlation is then the delay time between the two sensors.
The method of correlation means that the time series of two parameters are combined element by element. The cross correlation can be used to derive the time shift between two time series. The cross correlation provides the agreement of the two signals depending on the time shift. The method was applied in this treatise to derive the time shift between two fast humidity sensors (see Sect. 5.4).

https://doi.org/10.24355/dbbs.084-201906170934-0

The synchronisation between a humidity sensor and the wind speed vector is commonly done by maximizing the covariance between the hygrometer data and the vertical wind speed component, which is proportional to the latent heat flux introduced in the following section. Favourable for the synchronisation is a large variability in the signals (changes of altitude, and high fluctuations), facilitating to derive a high correlation.

https://doi.org/10.24355/dbbs.084-201906170934-0

4 Specific sensors (S) and techniques for boundary layer studies

Generally there is a large number of different and complementary meteorological sensors that are used for airborne applications. Among these instruments, this section will focus on new techniques for humidity and for meteorological and aerosol miniaturized payloads. They were operated during the field research studies described in Chapt. 5. As mentioned at the beginning of the treatise, the objectives concern the physical processes and properties of the atmospheric boundary layer investigated at the work group "Airborne Meteorology and Measurement Techniques".

4.1 LICOR water vapour sensor - S1

As presented in Sect. 1.3.2 above, the working principle of the LICOR sensor series for water vapour and carbon dioxide is recalled. They are based on the absorption of near infrared (NIR) radiation by water vapour (H_2O) and carbon dioxide (CO_2). The radiation source is a small lamp with broadband emissions in the NIR spectral range. The radiation is focussed on a filter wheel with narrow bandpass filters of different wavelengths, rotating at a speed of 150 Hz. The wavelength of 2590 nm is absorbed by water vapour but not by CO_2, the wavelength of 4260 nm by CO_2, but not by water vapour, and the wavelength of 3950 nm serves as a reference, where neither carbon dioxide nor water vapour have absorption bands. The narrow band-pass filtered radiation then passes the measurement cell of 12.5 cm length, where the ambient air either passes passively (open path sensor) or is pumped through (closed path sensor), and partly absorbs radiation depending on the number density of water molecules, as well as on CO_2 number density. The detector on the other side of the measurement cell is a thermopile, additionally cooled by Peltier elements. The system is described more in detail in Licor (2014).
The LICOR sensors are available as open path sensors (LI-7500, and the newer LI-7500A), and as closed path sensor (LI7200). On the Helipod, a LI-7500 is permanently installed. During a humidity test flight with the Do-128 aircraft, three different LICOR systems were available (open path LI-7500 with serial number 75H-0775, open path LI-7500A with serial number 75H-2287, and closed-path LI-7200 with serial number 72H-0584, the latter contributed from the Alfred Wegener Institute for Polar and Marine Research). The two open path sensors were covered by a metal grid to enforce turbulent mixing and to avoid gradients of concentration in the measurement cell. The three LICOR sensors were installed additionally to the standard meteorological instrumentation on the nose boom (LI-7500A, in the following called Li1), in the cabin directly under the roof (LI-7200, called Li2), with a backward facing inlet and a flow controller sampling the air near the LI-7500 (called Li3) on the roof (see Fig. 4.1). All sensors were oriented along the aircraft. The sensors were not purged with nitrogen or dried air.

https://doi.org/10.24355/dbbs.084-201906170934-0

Figure 4.1: The three LICOR sensors integrated into the Do-128 during the humidity sensor intercomparison flight on 23 October 2015: (a) LI7200 in the cabin with an inlet near the LICOR sensor on the roof, (b) LI7500A on the nose boom, (c) LI7500 on the roof , and (d) the Do-128 equipped with additional sensors during the flight (last photo courtesy of Uwe Bethke).

In the following, the time shift between the different sensors is determined.
The stainless steel inlet to the Li2 sensor had a length l_1 of 350 mm, an inner diameter of 9.6 mm, resulting in an area of A_1=7.24·10^{-5}m^2. A volume flow controller provided a flow of Q=15 l min^{-1}=2.5·10^{-4} m^3 s^{-1}. For the tube, the airspeed is therefore $v_1 = \frac{Q}{A_1}$=3.45 m s^{-1}. This results in a time delay $\Delta t_1 = \frac{l_1}{v_1} =$ 0.1 s. Similar calculations are applied for the nylon tube of length l_2 = 400 mm and inner diameter of 8 mm, guiding the air from the inlet to the sensor, which results in an additional time delay of 0.03 s. Additionally, the time for exchanging the air of the measurement cell with an inner diameter of 25 mm and a half length of 125 mm amounts to 0.12 s. Altogether, there is a delay time of 0.25 s caused by the sampling system for the Li2.
Before calculating the latent heat fluxes with the eddy covariance method, a temporal shift of the LICOR signals was performed to obtain the highest correlation with the temporal behaviour of the Lyman-Alpha signal. The Lyman-Alpha was treated as reference. In the LICOR sensor handbook, a time delay is explained by the internal data processing. The sensor performs measurements internally with a frequency of 150 Hz. The data is processed and provided at a maximum frequency of 20 Hz. This results in a time delay of 0.185 s for the LI7500, and 0.13 s for the LI7500A and LI7200. The time shift between the Lyman-

https://doi.org/10.24355/dbbs.084-201906170934-0

Alpha and the Li1 sensor in the nose boom was 0.15 s. As stated in the LI7500A manual, an internal delay of 0.13 s is caused by data processing. The remaining small difference of 0.02 s may be explained by the sampling geometry, as the Li1 is covered by a metal grid as explained above. The time shift between the Lyman-Alpha and the Li3 sensor at the cabin roof was 0.3 s. Therefore, the delay time between the two open path sensors Li1 and Li3 amounted to 0.15 s. This can be well explained by the different internal delay times of 0.13 s for the Li1 and 0.185 s for the Li3, amounting to 0.05 s, plus additionally the distance δs of 7 m between the two sensors (Li1 installed at the nose boom, Li3 at the cabin roof) and the true airspeed v_{tas} of 70 m s^{-1}:

$$\Delta t = \frac{\Delta s}{v_{tas}} = \frac{7\,m}{70\,m\,s^{-1}} = 0.1\,s \tag{4.1}$$

The time shift between the Lyman-Alpha and the Li2 in the cabin was 0.45 s. Subtracting the values for the time shift caused by the distance (0.1 s) and the internal delay (0.13 s), this results in a time difference of 0.22 s. This delay can be explained by the tube length and flow speed for guiding the air to the measurement cell in the cabin, as calculated above.
For further calculations, the best fitting time shift correction was applied to all three LICOR sensors. The correlation between the LICOR signals and the Lyman-Alpha was better than 0.95 for the Li2 and Lyman-Alpha, and exceeding 0.8 for the Li1 and Lyman-Alpha for the part of the flight considered here. The best correlation between Li3 and Lyman-Alpha amounted to 0.6, thus was considerably lower (Fig. 5.27).
The calculations of the best fitting time delay were verified by maximizing the coherence spectra of the LICOR sensors and the Lyman-Alpha as a reference, and at the same time minimizing the phase between the two signals. This resulted in the same delay times as determined by the method of maximizing the correlation.

4.2 Miniaturized payload for UAS - S2

4.2.1 Meteorological payload

The M^{2}AV is equipped with a miniaturized turbulence measurement payload comprising a multi-hole probe for deriving the angle of attack and sideslip in the aerodynamic coordinate system, which was developed and manufactured at the Institute of Fluid Dynamics, TU Braunschweig. For the transformation of the wind vector into the meteorological coordinate system, a three-axis micro electromechanical system (MEMS) IMU developed at the Institute of Aerospace Systems of TU Braunschweig with a weight of 15 g is deployed, together with a single-antenna single-frequency GPS receiver of the company μ-blox, type SAM LS (van den Kroonenberg et al., 2008).
Further, the payload includes both a slow but accurate Pt1000 (Vaisala HMP50) and a thermocouple as fast temperature sensor, as well as a capacitive humidity sensor Vaisala humicap HMP50 (Martin et al., 2011).
The parameters measured by the M^{2}AV (profiles of temperature, humidity, wind speed and wind direction, including TKE and turbulent fluxes of sensible heat) have been validated extensively against other airborne measurements (Spiess et al., 2007), as well as in-situ measurements from a meteorological tower and remote sensing observations (Martin et

https://doi.org/10.24355/dbbs.084-201906170934-0

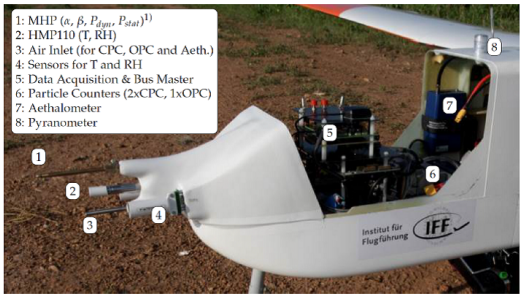

Figure 4.2: ALADINA payload in the front compartment. The different sensors are (1) multi-hole probe for deriving the static and dynamic pressure, and angle of attack and sideslip (2) temperature and humidity sensor HMP110 (3) common air inlet for all aerosol instruments (4) housing containing sensors of temperature (TSYS01, finewire) and humidity (RapidP14) (5) data acquisition system (6) particle counters (7) aethalometer (8) upward looking pyranometer. Figure from Bärfuss et al. (2018).

al., 2011, Cuxart et al., 2012). The accuracy of the wind speed is around $0.8\,\mathrm{m\,s^{-1}}$, and around 15° for wind direction (Martin et al., 2011).

The meteorological payload and data acquisition of ALADINA was originally provided by the University of Tübingen (Altstädter et al., 2015). This was replaced in 2016 by an own setup of the Institute of Flight Guidance, see Fig. 4.2 (Bärfuss et al., 2018): For positioning and attitude, a miniature MEMS based IMU and GPS system, the iμVRU of iMAR, Germany, was implemented. There are three different temperature sensors: The HMP110 (Vaisala, Finland) consisting of a Pt1000 element, the digital factory-calibrated sensor TSYS01 of IST, Switzerland, and a fast finewire sensor developed at the Institute of Flight Guidance. Compared to the formerly used finewire sensors, more robustness was achieved by adding a suitable housing. It was possible to perform more than 30 h of flight time during the first campaign in Benin, West Africa, without the need to replace the finewire sensor (Bärfuss et al., 2018). Further, the temperature sensors have been equipped with specific housings to shield them against solar radiation, and provide total pressure conditions and sufficient throughflow, adopted from the housings of temperature sensors for manned aircraft. The method of complementary filtering for the sensors of different time constants is applied (see Sect. 3.1).

For measuring humidity, two different capacitive sensors are used, the standard humidity sensor HMP110 of Vaisala, Finland (Ingleby et al., 2013), and the Rapid P14 of Innovative Sensor Technology, Switzerland, which has been characterized in detail by Wildmann et al. (2014b). Further, a multi-hole probe is installed to derive the angle of attack, sideslip, dynamic pressure and static pressure for the wind speed calculation described in Sect. 3.2. In contrast to the measurements of pressure difference between each hole and the central hole for the angle of attack and sideslip, as applied by van den Kroonenberg et al. (2008)

https://doi.org/10.24355/dbbs.084-201906170934-0

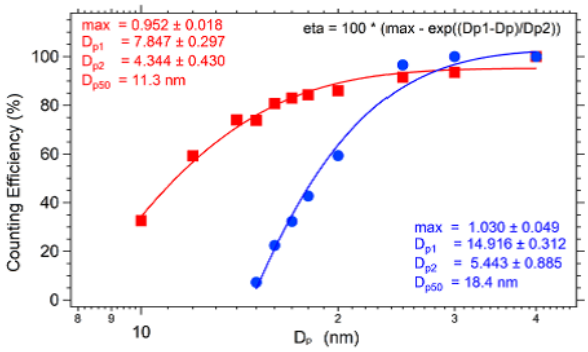

Figure 4.3: Counting efficiency of the two CPCs [%] in dependence of the particle diameter D_p [nm]. Figure from Altstädter et al. (2015)

and Wildmann et al. (2014c), pressure differences from opposite holes are measured directly, as in Corsmeier et al. (2001) and Reinemann et al. (2013). Pressure tubes with a length shorter than 200 mm are used to shift resonance effects to higher frequencies above 100 Hz.
Additionally, two silicon pyranometers EKO ML-01, EKO Instruments, Co., Japan, were implemented, one facing upwards, one facing downwards. They record broadband solar radiation in the wavelength range of 400 to 1100 nm with a response time smaller than 1 ms.

4.2.2 Aerosol payload

The main reason for the development of ALADINA was the need to study new particle formation (NPF) with high resolution on a local scale. Therefore, the payload consists of two condensation particle counters (CPC) and an optical particle counter (OPC). With a CPC it is possible to count aerosol particles from a very small diameter (in the range of several nm) up to some μm. The very small particles (in the literature called ultrafine particles or nucleation mode particles, see Kannosto et al., 2008) are an indicator that the particles formed within the atmosphere out of the gase phase (secondary aerosol), and were not emitted directly from the surface (primary aerosol).
The working principle of a CPC is the following: Aerosol particles enter the sensor and pass a chamber that is filled with saturated butanol, or in this case isopropanol vapour. This saturator is kept at a certain temperature. Then the aerosol and isopropanol vapour pass a second chamber, the condensor. There the temperature is significantly lower, and the vapour condensates on the aerosol particles, acting as condensation nuclei. The particles grow to a size of several μm (Marti et al., 1996), and can then be detected and counted by a light barrier.
In the case of ALADINA, the CPC that was selected due to its already low weight of

https://doi.org/10.24355/dbbs.084-201906170934-0

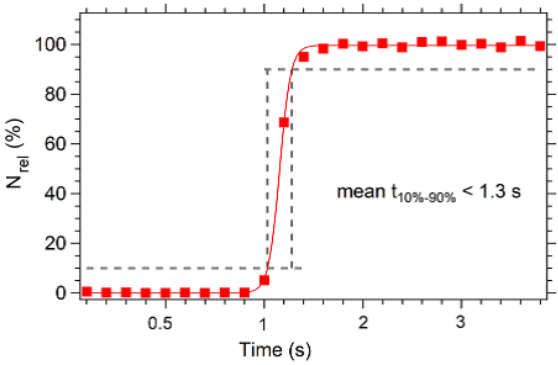

Figure 4.4: Relative counting efficiency of the CPC depending on time after the application of a sharp increase of particles. The response time for an increase of 10-90 % of the signal is 1.3 s. Figure from Altstädter et al. (2015)

around 900 g is the handheld model TSI3007 (TSI, USA). It was further miniaturized by the project partners at TROPOS in Leipzig, by removing the housing and display, strapping down the system to the vital parts (a pump for well-defined air flow, optical unit with saturator, condensor and detector), which were not modified. The temperature difference was adjusted in a way that for the first CPC, called CPC1, a lower detection threshold of 11 nm was obtained (N_{11}), and for the second CPC, called CPC2, a diameter of 18 nm (N_{18}). The calibration curves with the detection efficieny depending on particle size are provided in Fig. 4.3. A counting efficiency of 50% was defined as the detection threshold. The difference between the CPC readings reveals the particle concentration in the size range between 11 and 18 nm (ΔN). The CPCs and their counting efficiencies were calibrated in the laboratory of TROPOS with silver particles of specified diameter. For later applications, the lower detection threshold diameters were set to 5 and 10 nm (Platis et al., 2015). The response time was reduced from 9 s given by the manufacturer in the data sheet to 1.3 s (Fig. 4.4) by increasing the volume flow rate from 0.10 to 0.16 l min^{-1} (Altstädter et al., 2015).

The optical particle counter (OPC) GT-526 of Met One Instruments, USA, provides the particle number concentration for larger particles, with a diameter in the size range of visible light. There are six particle size channels, corresponding to a diameter of 300 nm, to 10 μm. Mie scattering strongly depends on the scattering diameter. Therefore, the measured scattering intensity is a function of particle size. Using particles of known size allows to calibrate the signal of the instrument.

For further studies, a black carbon (BC) sensor MicroAeth AE51, AethLabs, USA, was included in the instrumentation (Bärfuss et al., 2018). It measures the BC mass concentration in the range of 0-1 mg m^{-3} with a resolution of 1 ng m^{-3}. The sensor is sensitive

https://doi.org/10.24355/dbbs.084-201906170934-0

to vibrations, therefore data are low-pass filtered during post-processing. The accuracy is around $\pm$ 0.2 μg m^{-3}.

4.3 Wind lidar - S3

The Institute of Flight Guidance owns a wind lidar of type "Wind Cube WLS8-8" (Leosphere, France) operating at a wavelength of 1.5 μm. The detailed description of a similar system can be found in Wächter et al. (2009). Laser pulses are emitted consecutively along the four directions 0 °, 90 °, 180 ° and 270 ° with a cone angle of 15 °. The Doppler shift of the backscattered signals along the line of sight is determined automatically. Data along one direction is available every 7 s, a full rotation takes 28 s. The system retrieves the vertical and horizontal wind speed and wind direction, therefore the full 3D wind vector with the components u, v and w in the meteorological coordinate system. The measurement principle is based on the Doppler shift for the radial data of the four directions. The averages over 10 min intervals as well as data with a temporal resolution of 7 s are provided as standard files. The system covers the altitude between 40 m and 500 m with a vertical resolution of 20 m. The wind speed accuracy for the mean wind is given as 0.5 m s^{-1} by the manufacturer. Remote sensing observations provide the advantage of reaching higher altitudes compared to in situ cup anemometers on a meteorological tower. The disadvantage consists of data gaps caused by unfavourable conditions like rain, low clouds or fog (Emeis et al., 2007).
However, for the wind lidar described here, the turbulent kinetic energy TKE calculated as in Eq. 3.5 results in a large overestimation of the horizontal wind speed variance (Newman et al., 2016). This can be explained by the different and rather large air volumes that are sampled consecutively.

https://doi.org/10.24355/dbbs.084-201906170934-0

5 Scientific results from field research studies

In this chapter, five research studies are presented. They are based on projects of the author while conducting research at the Institute of Flight Guidance, TU Braunschweig. It is recalled that they concern the characterization of the low-level atmospheric boundary layer and the formation of new particles within the atmosphere. As reported in the bibliography section, the results are published in Altstädter et al. (2015, 2018a), Canut et al. (2016), Emeis et al. (2016), Lampert et al. (2015, 2016, 2018a,b), Platis et al. (2015, 2018), Siedersleben et al. (2018a,b) The results were obtained from measurements carried out during specific field experiments with the platforms and sensors presented in Chapt. 2 and Chapt. 4, with the corresponding references labelled in brackets in the section title.

5.1 Low-level jet statistics and its importance for wind energy (S3)

As described in Sect. 1.3.1, an increase in wind speed below the rated speed of a wind turbine will lead to an increase in the annual energy production. Therefore, atmospheric features contributing to an enhanced wind speed at altitudes of wind turbines are of particular interest for wind energy. One such phenomenon is the low-level jet (LLJ), which can generally be observed during the night (Blackadar, 1957, Mahrt et al., 1979, Stull, 1988) at many locations worldwide, and frequently develops in the North German Plain as well (Kraus et al., 1985, Wittich et al., 1986, Gross, 2012).
In this section, a one-year data set of wind lidar (Sect. 4.3) is analysed with respect to the LLJ. The results of the following case study have been published in Lampert et al. (2015).

5.1.1 LLJ definition

In the literature, different definitions of the LLJ exist, depending on the measurement site and typical wind speed of the LLJ, as well as on the available instrumentation (Banta, 2008). In this study, mainly the criteria of Baas et al. (2009) are used to identify cases of a LLJ occurrence for vertical profiles of the horizontal wind speed averaged over a 10 min interval. The profiles were inspected individually to determine the exact start and end time of the LLJ occurrence. Due to the large variability in the wind speed profiles, automated routines have to be checked carefully (Emeis, 2014) to make sure they fullfil the following criteria (see Fig. 5.1):

- The maximum wind speed is at least $2\,\mathrm{m\,s^{-1}}$ and 25 % higher than the minimum wind speed above (Baas et al., 2009).

https://doi.org/10.24355/dbbs.084-201906170934-0

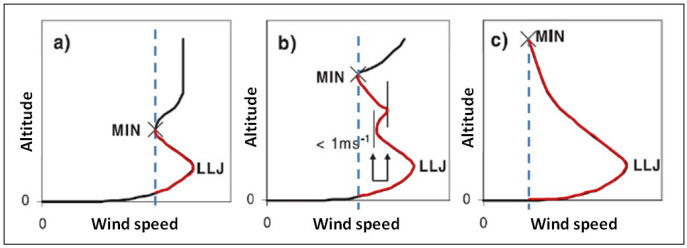

Figure 5.1: Definition of the LLJ according to the first three criteria in Sect. 5.1.1. The figure has been adapted from Baas et al. (2009)

- A wind speed minimum is not taken into account if the wind speed above increases less than 1 m s^{-1} and then decreases again below the first minimum wind speed (Baas et al., 2009)
- If no explicit minimum is available in the profile, the lowest wind speed above the maximum wind speed is used as minimum (Baas et al., 2009).
- At least three consecutive vertical profiles must fullfil the first three criteria, so that a LLJ persists for 30 min at least. In the definition of Baas et al. (2009), the criteria have to be met even for 1 h to define a LLJ. However, they used vertical profiles with a temporal resolution of 30 min.
- If a profile is classified as LLJ according to the criteria above, all altitudes below the wind speed minimum for which the wind speed is higher than the minimum wind speed are included as LLJ (see Fig. 5.1).
- There is explicitly no temporal constraint, as the LLJ may occur not only during the night, but less frequently during the day as well. This is different from e.g. the definition of Emeis (2014).

5.1.2 Location of the study

For the year-round observations that are used here to analyse the LLJ, Braunschweig airport (ICAO identifier EDVE, 10 ° 33.27' E, 52 ° 19.15' N, 91 m altitude AMSL) in the North German Plain was chosen as a typical location in the North German Plain and due to its proximity to the Institute of Flight Guidance. Braunschweig is located about 50 km North of the nearest low mountain range (Harz mountains with the maximum elevation, Brocken, of 1141 m) and about 250 km South of the Baltic and North Sea. It is located about 60 km East of Hanover, where another study about LLJ statistics by Emeis (2014) is based. Within Braunschweig, the site is located at the periphery in the North East of the city. During the prevailing westerly wind direction, the site is not influenced by the main city plume. However, for southerly wind directions, the site could be influenced by

https://doi.org/10.24355/dbbs.084-201906170934-0

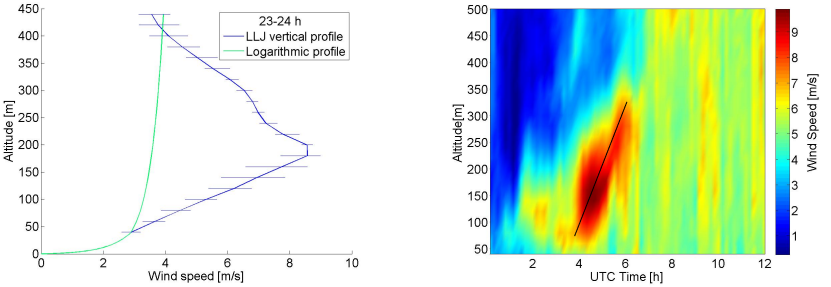

Figure 5.2: Examples of typical LLJ observations: (a) Vertical profile of the LLJ averaged over 1 h on 13 December 2013, 23:00-24:00 UTC, and logarithmic profile of the wind speed, assuming 0 m s^{-1} at ground and the observed wind speed at 40 m altitude. The horizontal error bars indicate the wind speed variability based on the 10 min averages. (b) Time series of the wind speed averaged over 10 min on 17 June 2013, 0:00 – 12:00 UTC. The wind speed is colour coded, the shift of the maximum wind speed with altitude is illustrated with a black line. Figures from Lampert et al. (2015).

the urban boundary layer, which has an impact on the wind profiles (Emeis, 2004) and affects LLJ properties (Wang et al., 2007, Kallistratova et al., 2009).

5.1.3 Analysis of LLJ events

For twelve months, the Lidar WLS8-8 was operated continuously at the site described above (1 June 2013 to 31 May 2014) The data availability based on 10 min intervals was 93.5 % (Lampert et al., 2015). A typical example of a vertical profile of the horizontal wind speed and a time series of the wind speed are shown in Fig. 5.2. The vertical profile exhibits a linear increase of the wind speed up to the maximum, as described in Banta et al. (2002). It can be seen that the logarithmic extrapolation of the wind speed from the wind speed value at 40 m altitude (green line in Fig. 5.2, Justus and Mihilai, 1976) is not appropriate and underestimates the wind speed at the altitudes of the LLJ maximum. The temporal evolution contains examples of both cases, an increase of the altitude of the wind speed maximum (Fig. 5.2), as in (e.g., Banta, 2008, Storm et al., 2009), as well as a decrease of the altitude with the wind speed maximum with time, as in the classical theory of the afternoon transition (Shapiro and Fedorovich, 2010). An overview of the annual distribution of LLJ events is given in Fig. 5.3. It can be seen that most LLJ events were observed during summer, especially in July. This is in agreement with the theory that the formation of the LLJ is more likely for strong temperature inversions, which build up mainly in summer. Furthermore, LLJ events frequently occur in “clusters” over several consecutive days. This feature can be related to the occurrence of favorable circulation patterns, as described in Emeis (2014). The most frequent maximum wind speed of all LLJ events was between 4 and 9 m s^{-1}, more precisely, for a Gaussian distribution, 65 %

https://doi.org/10.24355/dbbs.084-201906170934-0

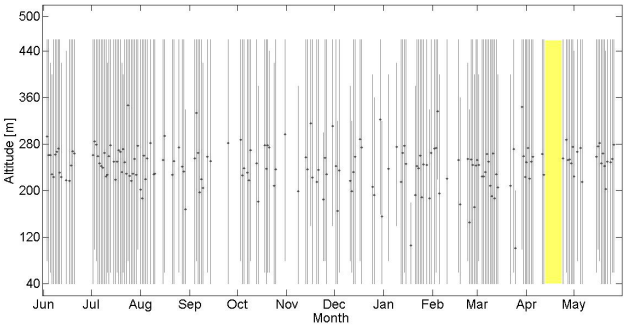

Figure 5.3: Distribution of LLJ events for the twelve month period. The dots indicate the altitude of the maximum wind speed. The vertical bars show the altitudes where the wind was classified as a LLJ. Yellow is a time span of instrument failure. It can be seen that the LLJ occurred more frequently in summer. Figure from Lampert et al. (2015).

of all events fell in the range of 3.7 to 8.9 $\mathrm{m\,s^{-1}}$ (see Fig. 5.4a). Very strong wind speed maxima exceeding 12 $\mathrm{m\,s^{-1}}$ were observed in less than 1 % of all events. The altitude of the maximum wind speed was located between 80 and 380 m, with the most likely, but not very pronounced maximum at 200 to 220 m altitude (see Fig. 5.4b).

The average wind shear for all LLJ events was 0.03 $\mathrm{s^{-1}}$ for the altitude between the lower starting point of the LLJ and the wind speed maximum. Assuming a wind speed of 0 $\mathrm{m\,s^{-1}}$ at ground, the average wind shear results in a value of 0.05 $\mathrm{s^{-1}}$. The maximum wind shear observed for this data set was 0.2 $\mathrm{s^{-1}}$. The wind shear values during LLJ events near Braunschweig are in agreement with the typical values between 0.02 and 0.1 $\mathrm{s^{-1}}$ as recorded by Emeis (2014).

This is not only of interest for wind turbines, but for departing and landing air traffic as well. The maximum wind shear that was encountered is not dangerous for flight safety according to the hazard potential limits identified by Krauspe et al. (1983), but may nevertheless increase the pilots' workload during landing.

5.1.4 LLJ impact on the Weibull wind speed distribution

It is recalled that the scale and shape factors of the Weibull wind speed distribution are calculated according to Eq. 1.6. The scale factor λ is directly related to the mean wind speed, therefore high values indicate higher wind speed. The shape factor κ is related to wind speed variance. Higher values indicate higher turbulence. They are summarized in Table 5.1. It can be seen that generally the scale parameter λ increases with altitude. This is according to the expectations, as it is an indicator of the mean wind speed at the corresponding altitude. Also the most probable wind speed, which is the maximum value

https://doi.org/10.24355/dbbs.084-201906170934-0

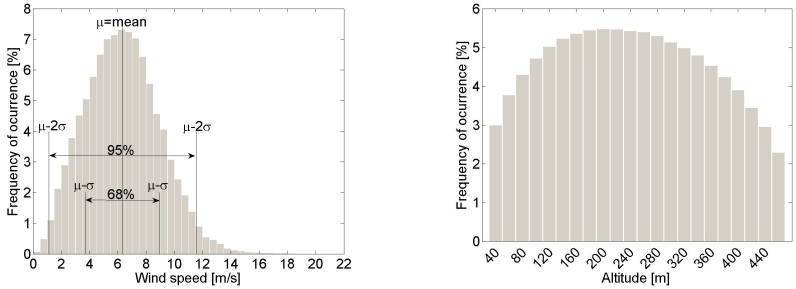

Figure 5.4: (a) Frequency of occurrence of LLJ events by wind speed. (b) Frequency of occurrence of LLJ events by altitude intervals.

of the Weibull distribution and the most likely wind speed, increases with altitude. The contribution of LLJ profiles to the Weibull distribution increases from around 5 % at 40 m to a maximum of around 8.8 % at around 200 m altitude and then decreases again. The LLJ is therefore typically centered at an altitude range which is of particular interest for wind energy. The shape parameter κ, which is an indicator of wind speed variance (Justus and Mihilai, 1976), reaches maximum values of 2.42 at an altitude around 100 to 140 m. This is below the LLJ core height. The results are in agreement with Emeis (2014), who reports higher altitudes of the shape factor maximum for flat terrain and lower altitudes for orographically inhomogeneous areas.
The dimensionless shape factor κ exhibits values larger than 2, a value which is often assumed for Europe (Rayleigh distribution, Burton et al., 2011). Higher values of the shape factor are common for tropical regions (Gasch and Twele, 2005, Indhumathy et al., 2014). Compared to the scale factor determined in Northern Germany (e.g., Gasch and Twele, 2005, Emeis, 2014), the observed values were slightly higher. The values for the scale factor λ, which is directly related to the mean wind speed, were lowest in summer (6 to 7 m s^{-1}) and highest in winter (8 to 9 m s^{-1}). The reason is the specific situation of cyclones in this particular year.

The influence of the LLJ is normally not quantified in a data set of wind distribution. To make the effect visible, the Weibull distribution was calculated for different altitudes, and the wind speed classified as LLJ was marked in magenta (Fig. 5.5). It can be seen that the LLJ shifts the wind speed distribution slightly to higher wind speed situations.

https://doi.org/10.24355/dbbs.084-201906170934-0

Table 5.1: Weibull parameters and influence of the LLJ for all altitudes. The LLJ contribution was not determined for the highest two altitudes.

Altitude $[m]$	Most probable wind speed $[m\,s^{-1}]$	shape parameter $[-]$	scale parameter $[m\,s^{-1}]$	LLJ contribution [%]
40	4.06	2.17	5.38	5.26
60	4.65	2.31	5.95	6.13
80	5.16	2.40	6.46	7.00
100	5.56	2.42	6.93	7.65
120	5.90	2.42	7.36	8.11
140	6.21	2.42	7.74	8.46
160	6.44	2.39	8.08	8.66
180	6.63	2.36	8.38	8.80
200	6.80	2.32	8.66	8.84
220	6.92	2.29	8.89	8.81
240	7.03	2.26	9.10	8.76
260	7.11	2.23	9.29	8.75
280	7.19	2.20	9.47	8.67
300	7.22	2.16	9.62	8.48
320	7.25	2.13	9.76	8.34
340	7.26	2.10	9.89	8.10
360	7.27	2.07	10.00	7.76
380	7.27	2.04	10.11	7.37
400	7.26	2.02	10.19	6.90
420	7.22	1.99	10.23	6.27
440	7.14	1.97	10.21	5.56
460	7.08	1.96	10.21	4.50
480	7.02	1.94	10.21	-
500	6.93	1.92	10.19	-

https://doi.org/10.24355/dbbs.084-201906170934-0

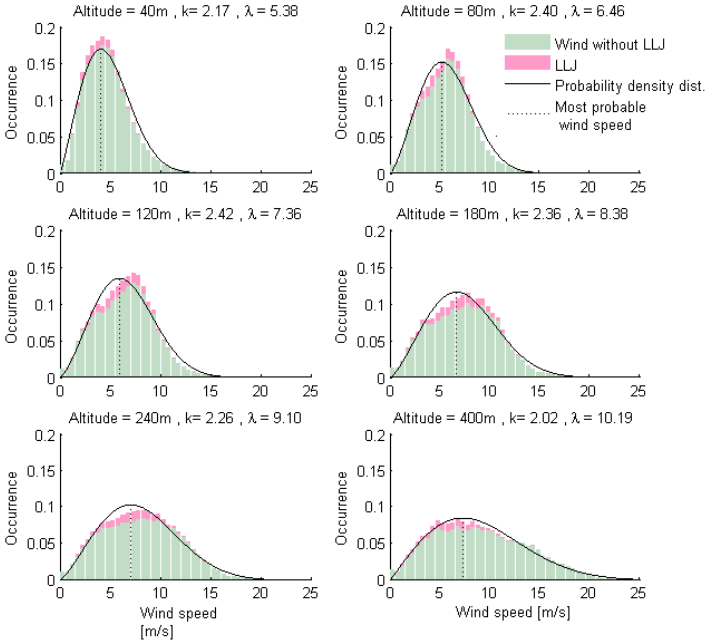

Figure 5.5: The Weibull wind speed distribution for different altitudes. Marked in magenta are the contributions of the LLJ profiles. Figure from Lampert et al. (2015).

https://doi.org/10.24355/dbbs.084-201906170934-0

5.1.5 Intra-annual variability of the Weibull distribution

An example of the scale and shape factor at a specific altitude of 120 m is shown in Fig. 5.6. A large variability for the scale and shape factor can be seen, depending over which time (month, season or year) the average was calculated. Therefore, to determine the expected annual output of wind turbines, it is not enough to extrapolate a data set covering less than a year of data. Assuming the Rayleigh distribution, this results in an underestimation of the scale parameter of 7 % at 40 m altitude and 17 % at an altitude of 100 to 140 m. According to Emeis (2001), this leads to an underestimation of the annual power output of wind turbines in the range of 6 to 15 %. For the scale factor, the underestimation of the power output based on a data set of one month only can be even more pronounced: For the altitude of 80 m, the maximum difference of λ between the monthly value and the annual value was around 0.5 m s^{-1}. The relative uncertainty of 8 % results in an underestimation of the wind energy output around 24 % (Emeis, 2001). Although the majority of LLJ events occur during the night above land, where the power consumption is at minimum, this might be of interest for the renewable energy mix, as solar power output is zero during the night. Above the North Sea, stable conditions and the development of LLJs can be expected presumably in spring and summer during the day (see Sect. 5.3).

5.1.6 Summary: Importance of LLJ for wind energy

The overall importance of the LLJ for wind energy consists in the fact that the LLJ shifts the wind speed to higher values at the altitude range of interest for wind energy applications. The LLJ contributes around 4 to 8.8% to the Weibull distribution for different altitudes at the measurement site Braunschweig in the North German Plains. There are high seasonal differences of the wind speed distribution, therefore a wind data set of a full year is required to estimate the potential of a site for wind energy (Lampert et al., 2015).

https://doi.org/10.24355/dbbs.084-201906170934-0

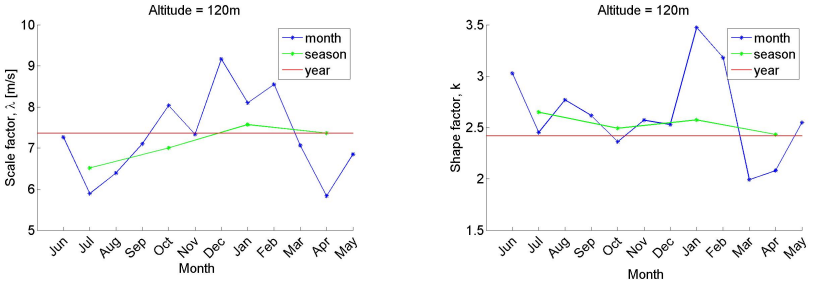

Figure 5.6: (a) The scale factor λ and (b) the shape factor κ of the Weibull wind speed distribution. Blue dots indicate the values calculated for each month. Green dots are calculated for each meteorological season. The red line shows the average for the whole year. Figures from Lampert et al. (2015).

https://doi.org/10.24355/dbbs.084-201906170934-0

5.2 Low-level jet and turbulence anisotropy (P3, S2)

The potential impact of the LLJ on engineering applications like air traffic during take-off and landing and especially wind energy has been described in the previous section. However, the LLJ has implications for different meteorological parameters as well. In this section, changes of turbulence parameters during the afternoon-evening transition are studied for particular days. They were observed with the M^2AV (Sect. 2.3) and the meteorological payload described in Sect. 4.2. Further it is shown how these parameters are altered under the influence of an LLJ. The results have been published by Lampert et al. (2016). A comparison of turbulence properties derived from an ultrasonic anemometer on a tethered balloon and the M^2AV is included in Canut et al. (2016).

5.2.1 Location, instrumentation and modeling

The large field experiment BLLAST (Boundary-Layer Late Afternoon and Sunset Turbulence) to study the afternoon and evening transition (AET) of the ABL from convectively mixed to stably stratified has been conducted in Southern France in summer 2011 (Lothon et al., 2014). Extensive ground-based instrumentation was available or explicitly set up near Lannemezan, located around 20 km North of the Pyrenee mountains. For this case study, data of the following instruments were analysed: radiosondes launched four times per day, frequent radiosondes providing hourly profiles of the ABL (Legain et al., 2013), an ultra-high frequency (UHF) radar for measurements of wind and potential temperature, and a 60 m tower. Embedded in this measurement network, four flights with the M^2AV were performed during the AET on a particular day, 2 July 2011 (see locations in Fig. 5.7). The flights started around 14:30, 16:30, 18:30 and 20:30 UTC, which corresponds to the same solar time as Greenwhich due to the similar geographical longitude. Sunset was at 19:42 UTC. The exact times of the flight are provided in Tab. 5.2.

The M^2AV flight patterns consisted of vertical profiles and horizontal race tracks with 1 km side length flown repeatedly at different altitudes within the ABL (see flight track in Fig. 5.7b). Three legs were flown at an altitude of 300 and 250 m each, and two legs at 200 m, then the whole pattern was repeated three times for each flight. Only during the last flight, the altitudes of the race track patterns were reduced by 50 m, as the ABL heigth was lower. The race track pattern was oriented in East-West direction. The individual straight legs were analysed concerning turbulence properties.

Modeling results provided by the Universitat de les Illes Balears, Palma de Mallorca, Spain, were used to relate and deeper understand the observations. The model used for the studies is the mesoscale model MesoNH (Lafore et al., 1998, Jiménez and Cuxart, 2014). They used two nested domains, the inner one centered at the observation site Lannemezan, with a high spatial resolution (400 x 400 m horizontal resolution, 3 m vertical resolution near the surface, and coarser resolution above). At the lateral boundaries and for initialisation, the model is driven by 6-hourly data of the European Centre for Medium-Range Weather Forecast (ECMWF). The simulation was started 3 days before the case study, and was able to reproduce well the atmospheric features.

https://doi.org/10.24355/dbbs.084-201906170934-0

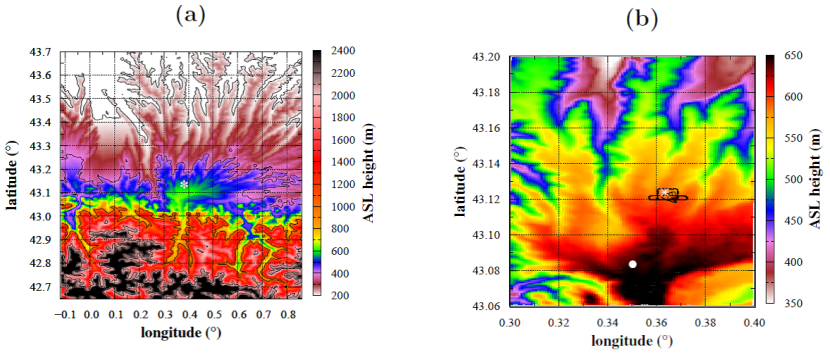

Figure 5.7: (a) The inner domain of MesoNH including the Pyrenee mountains and foothills. Lannemezan is located at the plateau coloured in green, with the Aure valley ath the South. Topographic lines at 200, 400, 1000 and 2000 m are shown. (b) Zoom of the first picture showing the location of the measurement site with the 60 m tower, UHF radar and radiosounding station (asterisk), the measurement site for frequent radiosondes and UHF radar (dot), and M^{2}AV flight track (black line). Figure from Lampert et al. (2016).

Table 5.2: Takeoff and landing for the M^{2}AV flights on 2 July 2011.

Flight	takeoff [UTC]	landing [UTC]
1	14:31	15:14
2	16:36	16:59
3	18:23	19:04
4	20:26	21:10

5.2.2 Meteorological conditions

The measurement site in Southern France on 2 July 2011 was influenced by a weak anticyclone over Great Britain and lower pressure in the Western Mediterranean. Therefore a weak flow in North-East to East-North-East direction was observed at low altitudes. At the same time, a plain-mountain circulation system persisted, resulting in northerly wind direction during the day at the Pyrenee foothills (Fig. 5.8a). There was a pronounced up-valley wind in the Aure valley South of Lannemezan. After sunset, at 20:30 UTC, a down-valley flow developed, but did not yet reach the foothills and Lannemezan, where the wind direction was East-North-East (Fig. 5.8b). At 21:30, the mountain to valley wind combined with the Easterly wind at the measurement site, resulting in a wind maximum, an LLJ (Fig 5.8c), which persisted until midnight (Fig. 5.8d). The model results of the wind speed at 100 m agree well with the local measurements of the wind vector at the 60 m tower (red arrow in Fig. 5.8). The agreement of simulations and observations is further shown in the time series in Fig. 5.9.

https://doi.org/10.24355/dbbs.084-201906170934-0

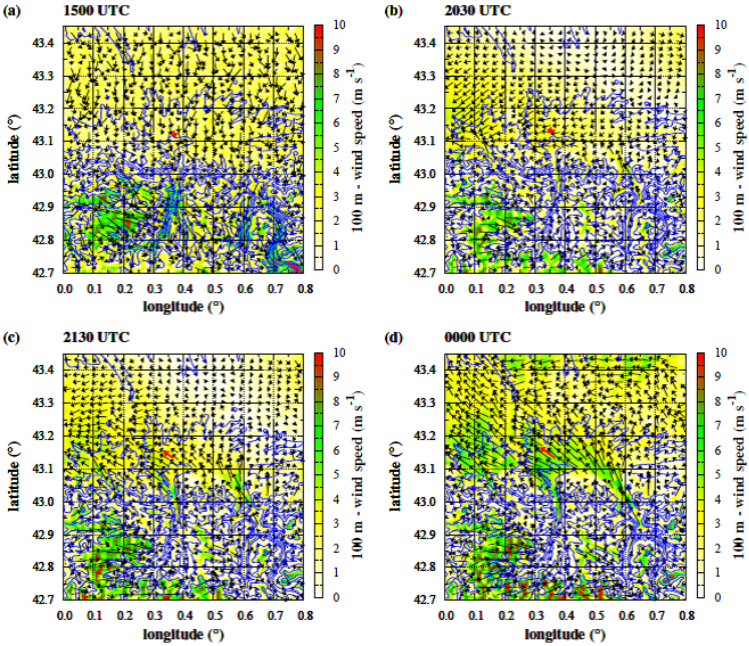

Figure 5.8: Development of the wind field at 100 m altitude from (a) 15:00, (b) 20:30, (c) 21:30 to (d) 24:00 UTC on 2 July 2011, as provided by the model MesoNH. The red arrow indicates the wind vector recorded at the 60 m tower. Figure from Lampert et al. (2016).

5.2.3 Development of meteorological parameters during the AET

The temporal development from 14:00 UTC to midnight on 2 July for the parameters wind speed, wind direction, temperature and TKE, observed by different methods and model output near ground show the typical behaviour as expected during the AET: A decrease in temperature, low wind speed until sunset, and a change in wind direction around sunset (Fig. 5.9). TKE decreases during the AET, but increases after sunset, caused by the development of the LLJ.

Observed profiles of the wind speed, wind direction and potential temperature, as well as the corresponding model results for the time steps of the M^2AV flights between 15:00 and 21:10 UTC are shown in Fig. 5.10. The potential temperature reveals a convectively well-mixed layer during the afternoon. A ground-based temperature inversion starts to build up at around 19:00 UTC, slightly before sunset (Fig. 5.10c, right panel). A strong temperature inversion exceeding 4 K is observed at 21:00 UTC (Fig. 5.10d, right panel). The wind direction changes from prevailingly North (Fig. 5.10a to c, middle panels) to

https://doi.org/10.24355/dbbs.084-201906170934-0

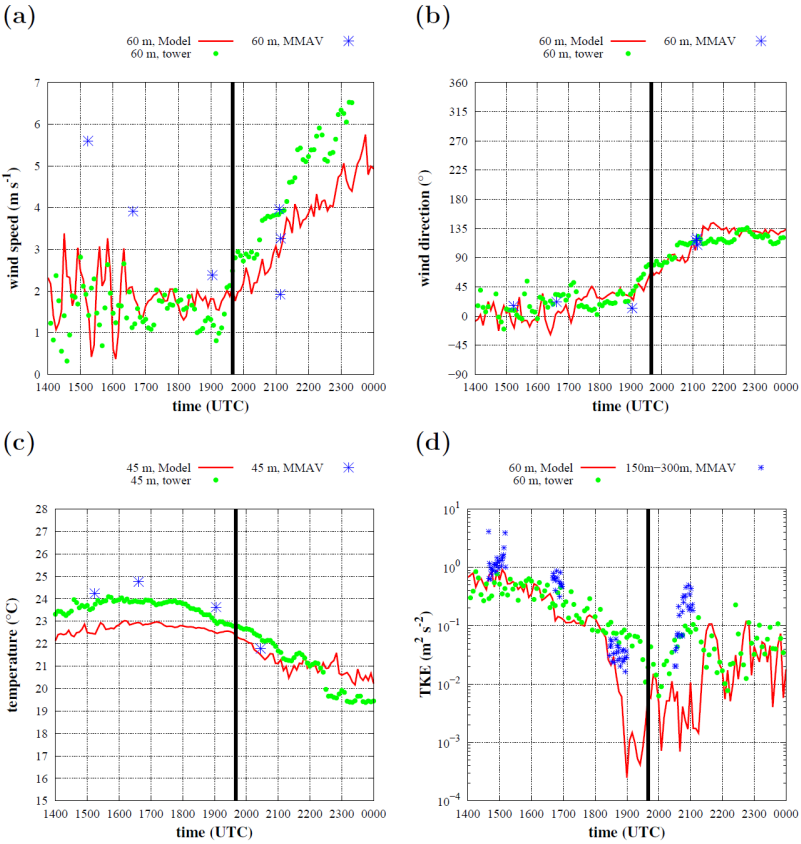

Figure 5.9: Modelled and observed time series for (a) wind speed (in $\mathrm{m\,s^{-1}}$), (b) wind direction (in °), (c) temperature (in °C) and (d) TKE (in $\mathrm{m^2\,s^{-2}}$) from 14:00 UTC until midnight on 2 July 2011. Tower observations are in green circles, model results in red lines and M^2AV data in blue asterisks. The temporal evolution of wind and temperature data from M^2AV is constructed with the values of the vertical profiles taken at the corresponding height of the tower measurements. For TKE, all the M^2AV legs where TKE is derived, at 150 m, 200 m, 250 m and 300 m AGL, are included in the plot. The time of sunset is represented with a black vertical line. Figure from Lampert et al. (2016).

East (Fig. 5.10d, middle panel). The wind speed (Fig. 5.10, left panels) is low near ground throughout the observation period. However, after 21:00 UTC, an LLJ profile develops

https://doi.org/10.24355/dbbs.084-201906170934-0

(Fig. 5.10d, left panel). It is captured by all observational data after 21:00 UTC, and it is present in the numerical observations, but not as pronounced as observed.

https://doi.org/10.24355/dbbs.084-201906170934-0

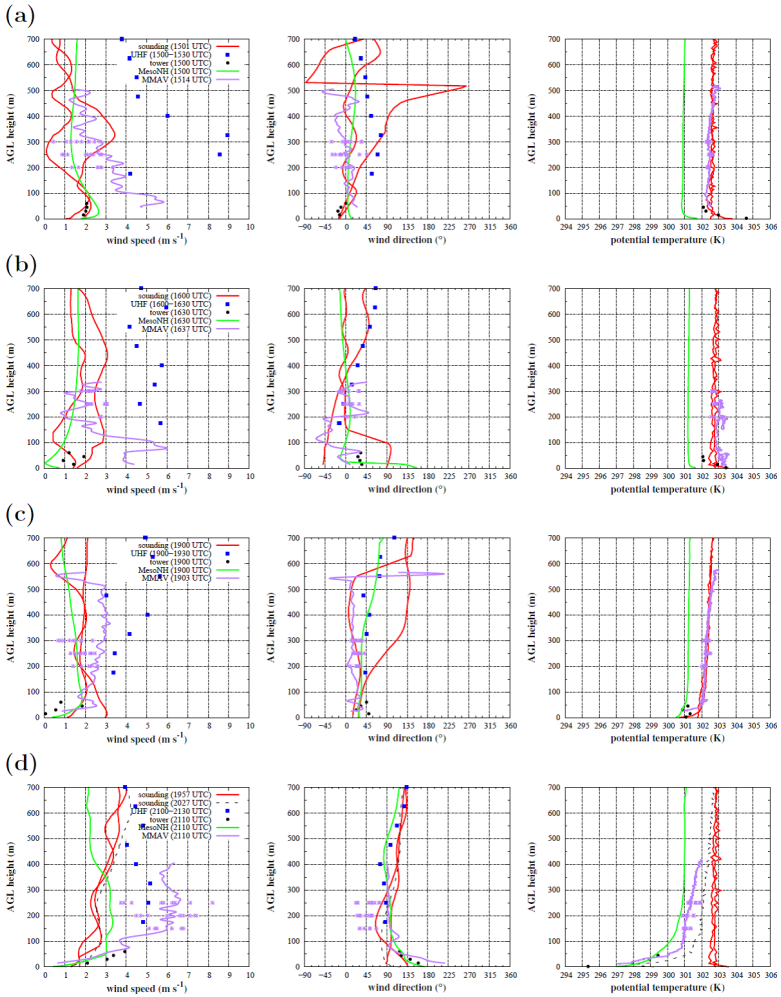

Figure 5.10: Vertical profiles of wind speed, wind direction and potential temperature at different instants during the M^{2}AV flights (a) around 15:00 UTC, (b) around 16:30 UTC, (c) around 19:00 UTC, and (d) around 21:10 UTC. Simulation results obtained with MesoNH are shown together with data of radiosounding, 60-m tower and M^{2}AV. Figure from Lampert et al. (2016).

https://doi.org/10.24355/dbbs.084-201906170934-0

5.2.4 LLJ effects on turbulence parameters

The observations and model output for the profiles of TKE are summarized in Fig. 5.11. For the M^2AV, the TKE values of each straight flight of 1 km length are provided, which show considerable variability. This is caused by small-scale inhomogeneities of the underlying surface, as well as properties of convection. However, altogether, it can be seen that the TKE is highest during the first flight around 15:00 UTC (red asterisks) and decreases slightly until 16:30 UTC (blue asterisks). At 19:00 UTC, TKE has decreased an order of magnitude (green asterisks), indicating very low turbulence under stable conditions. The TKE values are in good agreement with the tower measurements (dots in same colours), which are available up to 60 m altitude. However, TKE values are enhanced again at 21:00 UTC at the altitudes of the M^2AV observations (150 to 250 m), a feature that is not captured by the tower measurements. This is the consequence of the LLJ, which is apparent in the profiles of wind speed (Fig. 5.10). The numerical simulations reproduce well the TKE at 15:00 and 16:30 UTC, providing the link between the slightly smaller TKE values near ground and at the altitudes of the flights (solid lines in red and blue). However, for stable conditions at 19:00 UTC (green line), the modelled TKE values are one order of magnitude lower. There is an increase in TKE during the LLJ event in the simulations (black line), but the values are more than one order of magnitude lower compared to the observations.

The temporal development of the anisotropy ratio is displayed in Fig. 5.12. At noon and during the early afternoon, the anisotropy, defined according to Eq. 3.7 as the ratio of the horizontal wind speed variance divided by the vertical wind speed variance, has values slightly below 1, indicating convective conditions. This changes gradually with the decreasing solar radiation, reaching values above 1 at around 18:00 UTC. Both observations and numerical simulations show the same behaviour. After sunset, the tower observations reveal a further slight increase in anisotropy. The airborne measurements obtained at the altitudes of the LLJ show even higher values of the anisotropy ratio. The measurements confirm the results of Mason and Thomson (1987), that eddies are suppressed in vertical direction and elongated along the wind direction. The model results with a spatial resolution of 10 km (red), however, do not capture the effect of the LLJ on the anisotropy.

To underline that the enhanced anisotropy was induced by the LLJ on this particular day, a comparison with the previous day is done (see Fig. 5.13). On 1 July 2011, similar synoptic conditions were present. However, in contrast to the day of interest for this study, a LLJ was not observed. A large difference is obvious in the vertical component of the wind speed variance after sunset: For the observations of the day without LLJ (black line in Fig. 5.13b), the wind speed variance was about a factor of 3 higher than for the day with the LLJ (green line). For the time that the LLJ was observed with the M^2AV, the horizontal component (green line, Fig. 5.13a) of the wind speed variance was enhanced compared to the observations without a LLJ on the previous day (black line).

Turbulence properties derived from a balloon-borne sonic anemometer agree well with turbulence properties obtained by airborne manned and unmanned systems at the same altitude (Canut et al., 2016). However, there are large differences in turbulence properties at ground and within the ABL (Canut et al., 2016), which makes it necessary to perform measurements in the lowermost few 100 m to understand the processes and perform validations of numerical simulations.

https://doi.org/10.24355/dbbs.084-201906170934-0

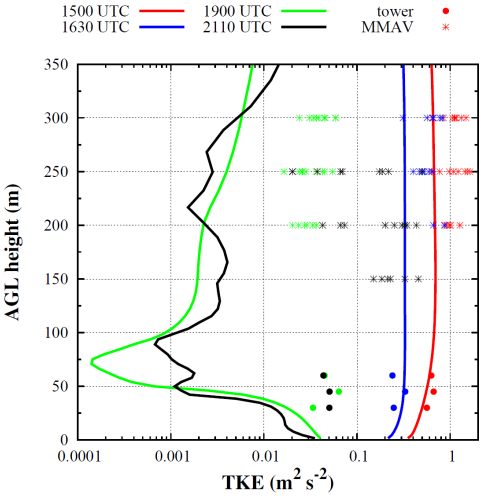

Figure 5.11: Vertical profiles of the simulated TKE (in lines) at different instants during the M^{2}AV flights (see legend). 60-m tower (in dots) and M^{2}AV (in asterisk) observations are included. Note the logarithmic scale on the x-axis. For M^{2}AV, $\sigma_u^2 = \sigma_v^2$ is assumed. Figure from Lampert et al. (2016).

5.2.5 Summary: Effect of the LLJ on turbulence parameters

In this section it was confirmed that TKE decreases during the AET. However, under stable conditions, turbulence is increased by the presence of a LLJ. Especially the horizontal wind speed component has a higher variability, as the horizontal wind speed is enhanced. The anisotropy ratio reveals that the variability of the vertical wind speed is low, as the stable stratification suppresses vertical motions. Observational and modelling results of this case study are published in Lampert et al. (2016) and in Canut et al. (2016).

https://doi.org/10.24355/dbbs.084-201906170934-0

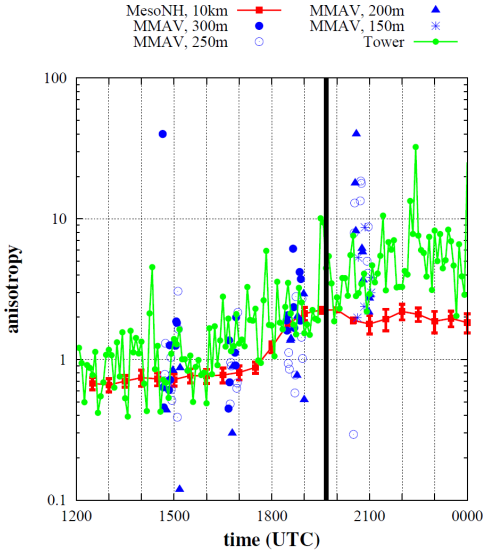

Figure 5.12: Time series of the anisotropy computed from different sources: M^{2}AV flight observations at 150 m, 200 m, 250 m and 300 m AGL during the four flights, each symbol representing a particular height (in blue); tower measurements at 60 m AGL every 5 min covering the afternoon-evening transition (in green); model results averaged between 150 m and 300 m to be close to the altitudes of the M^{2}AV observations considering a spatial area of 10 km x 10 km centered at Lannemezan (in red). The time of sunset is represented with a black vertical line. Note the logarithmic scale on the y-axis. For M^{2}AV, $\sigma_u^2 = \sigma_v^2$ is assumed. Figure from Lampert et al. (2016).

https://doi.org/10.24355/dbbs.084-201906170934-0

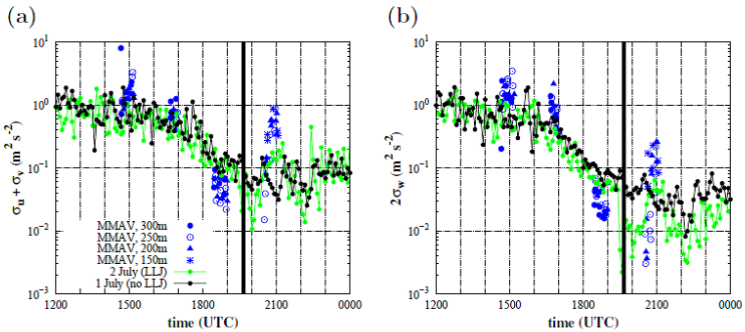

Figure 5.13: Time series of (a) horizontal and (b) vertical component of the wind speed variance. 60 m tower measurements for two consecutive days, 1 and 2 July 2011, are provided (black and green lines, respectively). The time of sunset is represented with a black vertical line. Note the logarithmic scale on the y-axis. For M^{2}AV, $\sigma_u^2 = \sigma_v^2$ is assumed. Figure from Lampert et al. (2016).

https://doi.org/10.24355/dbbs.084-201906170934-0

5.3 Far field wakes behind offshore wind parks (P1)

In this section, observations of far field wakes downstream of offshore wind parks are analysed and interpreted. They were obtained during the WIPAFF project with the instrumented Do128-6 aircraft (see Sect. 2.1). Results are published in (Emeis et al., 2016, Platis et al., 2018, Siedersleben et al., 2018a,b, Lampert et al., 2018b).

5.3.1 Overview WIPAFF project

As introduced in Sect. 1.3.1, satellite images of sea surface properties suggest the presence of wakes behind wind farms with an extension up to several 10 km. This phenomenon is of interest for three reasons: First, the lower wind speed in the lee of wind parks reduces the energy output of other downstream wind parks. Second, changes in the wind field may have an impact on the local climate. A stably stratified ABL may be modified mechanically by the motion of the rotor blades, with changes in temperature and moisture distribution. As air masses rise at the enhanced surface roughness elements represented by wind parks, these vertical motions can induce a different pattern of cloud formation. Third, the reduced wind speed in the wakes induces less forcing on the water surface, and there is increased shear due to the wake turbulence. This may modify the stratification and mixing processes of the water column, with an impact on circulation patterns in the North Sea. The coupling with the ocean has not yet been investigated in detail. The far field wake phenomenon was addressed by the project WIPAFF (Wind Park Far Field). *In situ* measurements, analyses of satellite images and mesoscale simulations were used to investigate the wake effects in dependence of the meteorological conditions. The project was led by KIT (Karlsruhe Institute of Technology) contributing with Weather Research and Forecasting (WRF) modelling, the author and the Institute of Flight Guidance were responsible for the airborne measurement campaign and the analyses of remote sensing information, the Institute of Environmental Physics of the University of Tübingen performed meteorological data analyses, the Helmholtz Center for Material and Coastal Research contributed with the analysis of satellite images, and the UL/DEWI Group (Deutsches Windenergie-Institut) participated with industry models for wind energy applications and analyses of ground-based meteorological measurements. During five campaigns at different seasons of the year, 41 measurement flights of 3.5 to 4 h duration were performed with the Do-128 above the German Bight, starting from Wilhelmshaven, Borkum or Husum. An overview of the flights is provided in Fig. 5.14.

https://doi.org/10.24355/dbbs.084-201906170934-0

Flight code	Date (dd.mm.yyyy)	Start Time (UTC)	End Time (UTC)	WS (m s^{-1})	Wind dir (°)	Wake length (km)	Atmospheric stratification
September							
Flight 1	06.09.2016	14:13	17:20	7	190	25	stable
Flight 2	07.09.2016	09:25	13:00	4	210	20	stable
Flight 3	07.09.2016	10:00	14:00	4	190	at least 10	stable
Flight 4	08.09.2016	10:38	14:25	8	120	at least 40	stable
Flight 5	09.09.2016	10:54	14:50	6	240	at least 45	stable
Flight 6	09.09.2016	15:43	19:17	6	250	at least 5	unstable
Flight 7	**10.09.2016**	**07:30**	**11:30**	**7**	**190**	**45**	**stable**
Flight 8	10.09.2016	12:05	16:00	4	190	at least 20	stable
March–April							
Flight 1	30.03.2017	15:57	19:02	15	240	70	stable
Flight 2	31.03.2017	15:36	19:00	13	180	50	stable
Flight 3	05.04.2017	15:42	16:34	14	310	10	neutral
Flight 4	06.04.2017	15:29	18:22	8	310	at least 10	unstable
Flight 5	09.04.2017	12:36	16:07	7	220	at least 50	stable
Flight 6	09.04.2017	16:32	20:12	4	200	n.a.	stable
Flight 7	11.04.2017	11:25	15:10	8	300	5	unstable
Flight 8	11.04.2017	16:12	20:04	8	240–280	25	neutral
Flight 9	13.04.2017	13:35	17:39	16	290	10	neutral
May–June							
Flight 1	17.05.2017	12:35	16:28	8	110	n.a.	stable
Flight 2	17.05.2017	17:16	21:22	12	120	55	stable
Flight 3	23.05.2017	15:42	16:34	5	250	at least 25	stable
Flight 4	23.05.2017	13:18	17:15	11	310	at least 35	neutral
Flight 5	24.05.2017	07:40	11:34	8	300	n.a.	unstable
Flight 6	24.05.2017	12:13	16:11	9	270	5	unstable
Flight 7	27.05.2017	09:57	13:58	10	150	at least 50	stable
Flight 8	27.05.2017	14:39	18:36	12	140	55	stable
Flight 9	31.05.2017	09:58	13:46	8	290	2	unstable
Flight 10	31.05.2017	15:00	18:50	9	290	0	unstable
Flight 11	01.06.2017	08:55	12:54	6	300	0	unstable
Flight 12	02.06.2017	08:55	12:40	4	170	at least 15	stable
August							
Flight 1	08.08.2017	10:35	14:35	9	80	at least 35	stable
Flight 2	08.08.2017	15:06	19:07	14	80	at least 55	stable
Flight 3	09.08.2017	10:34	14:37	15	210	n.a.	unstable
Flight 4	09.08.2017	15:09	19:05	13	240	n.a.	unstable
Flight 5	10.08.2017	12:49	16:54	5	330	n.a.	unstable
Flight 6	14.08.2017	12:08	16:07	8	150	at least 35	neutral
Flight 7	14.08.2017	16:40	20:31	7	120	50	stable
Flight 8	15.08.2017	09:22	13:15	8	180	30	stable
Flight 9	17.08.2017	08:06	12:10	12	160	40	stable
October							
Flight 1	14.10.2017	14:59	18:40	15	260	n.a.	stable
Flight 2	15.10.2017	09:05	13:09	14	200	n.a.	unstable
Flight 3	15.10.2017	13:52	17:50	13	190	at least 25	stable

Figure 5.14: Overview of the flights performed during the WIPAFF campaign. Besides date and time of each flight, the prevailing meteorological conditions (wind speed, wind direction, atmospheric stability) and the observed wake length are provided. For wake lengths longer than the final leg, a wake length of "at least" the specific distance is given. For flight patterns other than meanders at hub height, e.g. flights above the wind park, the wake lenght is not available (n.a.). The flight in bold letters is used for the studies of Platis et al. (2018) and Siedersleben et al. (2018b). Table from Platis et al. (2018).

https://doi.org/10.24355/dbbs.084-201906170934-0

5.3.2 Wind parks and flight pattern

For the investigation of far field wakes, basically the downstream flow of two different wind parks were chosen. The wind park *Godewind* was a suitable study object during westerly and south-westerly flow, as there were no other wind parks located downstream within the next 50 km. The wind park *Amrumbank West*, in direct vicinity of the wind parks *Nordsee Ost* and *Meerwind Süd Ost* was investigated for wind from East to South, with long wakes developing above the water surface (Fig. 5.15). Permission to operate in the Danish or Dutch air space were not requested. Cases with wind direction from North and North-West were studied as well, but no long wakes developed due to prevailingly unstable conditions with cold air mass advection. In the following case studies, measurements were performed in the lee of the wind park *Amrumbank West*. It consists of an ensemble of 80 wind turbines of type Siemens SWT-3.6-120 with a hub height of 90 m and a rotor diameter of 120 m. Each turbine has a nominal power output of 3.78 MW. The wind turbines are arranged in a regular rectangular array, with a longitudinal extent of around 9 km and a latitudinal extent of around 4 km.

In order to investigate the direct impact of wind parks on the downstream wind field, different flight patterns were developed: For analysing the far field wake properties, a meander pattern was applied. The undisturbed flow upstream of the wind park was probed on sections both perpendicular and parallel to the mean wind direction. Then meteorological and surface properties were recorded downstream at hub height. The individual legs were oriented perpendicular to the wind direction at distances of 5, 15, 25, 35, 45, and up to 55 km (see example in Fig. 5.15).

For quantifying the wake impact in the vertical, a second flight pattern probed the air at the same distance (5 km downstream the wind park) at various altitudes, from the minimum possible flight altitude of 60 m, the hub height of 90 m, the altitude of the blade tips 120 m, then 150 m and finally 200 m. The legs were oriented perpendicular to the mean wind direction.

For investigating the changes in the flow field around and above a wind park, a grid pattern at constant altitude consisting of legs parallel and perpendicular to the mean wind direction were performed. During the measurement campaign and with ongoing data evaluation, this pattern was refined to repeating three legs at constant altitude perpendicular to the wind direction as often as possible, one upstream of the wind park, one directly above the wind park, and one 5 km downstream of the wind park to obtain sufficient data for statistically relevant information on turbulent fluxes.

All flight patterns were complemented by performing vertical profiles on the way from the airport to the measurement area and back, as well as after completing a pattern.

https://doi.org/10.24355/dbbs.084-201906170934-0

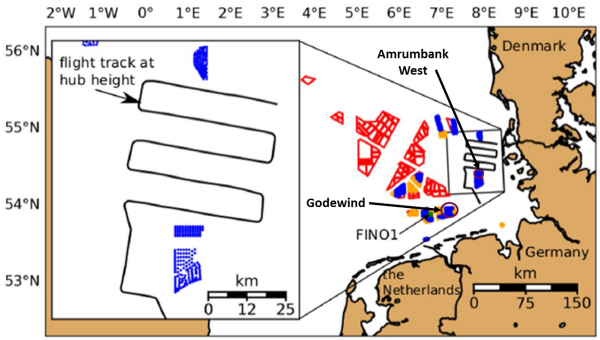

Figure 5.15: Map of offshore wind parks in the German Bight at the end of 2017. Operational wind parks are indicated in blue on the right, wind parks under construction are shown in orange, and planned wind parks are provided as red polygons. The objects of study, the wind parks *Godewind* and *Amrumbank West*, are indicated as purple circles and by arrows. The flight track of the Do-128 aircraft for a measurement flight behind the wind park Amrumbank West on 10 September 2016 is given as black line. In the enlarged picture, individual wind turbines are represented as blue asterisks. The wind direction was from 190°. Picture from Platis et al. (2018)

5.3.3 Observations and analyses of the far field wake

Altogether, wakes with a length of at least 10 km were observed during 27 different measurement flights. The airborne observations on 10 September 2016 are an example of a long far field wake extending beyond 45 km downwind of the wind park *Amrumbank West*. The flight was conducted from 7:30 to 11:30 UTC. The wind direction was from South. Therefore, air masses heated up above land were advected above the colder North Sea with a sea surface temperature of around 19° C. This results in stable stratification, enabling the formation of long wakes.

Fig. 5.16 shows the measurements of different parameters: Panel (a) provides the wind speed measured by the aircraft along the flight track and linearly interpolated across the flight track. There is a pronounced wind speed gradient from the West (wind speed around 9 m s^{-1}, red colour) towards the East and the German coast (wind speed around 7-8 m s^{-1}, green to yellow colour). However, directly downstream of the wind park, a significant reduction of the wind speed to values around 5-6 m s^{-1} is visible. The wind speed deficit recovers with distance, but is still present at a distance of 45 km.

Panel (b) shows the sea surface reflectance obtained by laser scanner. In the wake downstream of the wind park, the reflectance is strongly enhanced. This is caused by a smoother sea surface. A more rough surface provides a higher scatter of laser reflections, which results in weaker signals scattered back to the detector. The smoother surface in the wake

https://doi.org/10.24355/dbbs.084-201906170934-0

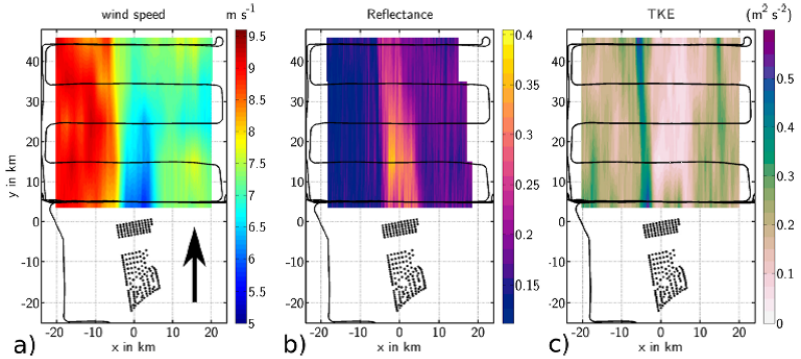

Figure 5.16: Airborne observations of the far field wake during a measurement flight downwind of the wind park *Amrumbank West* on 10 September 2016. Individual wind turbines are represented as black asterisks. The wind direction from 190° is indicated as a black arrow. The meander flight track is shown as a black line. (a) Wind speed, indicating the reduced wind speed downstream of the wind park (b) reflectance of the sea surface recorded by laser scanner, representing a smoother sea surface in the wake, (c) turbulent kinetic energy providing evidence of strongly enhanced turbulence at the western edge of the wake, and decreased turbulence at hub height within the wake (Platis et al., 2018)

can be expected due to less forcing of waves by wind drag, and is in agreement with SAR satellite observations showing evidence of modified surface properties downstream of wind parks.

Panel (c) displays the TKE. Here, the picture of the wake is more complex. On the western edge of the wind park, a strong increase of turbulence is observed. The crew clearly felt enhanced aircraft vibrations during the measurement flight. The increase of TKE is less pronounced on the eastern edge. This asymmetry may be caused by the different geometry of the wind park and density of wind turbines. They are arranged in a sharper contour in the West. Further, the wind speed gradient from the area directly next to and within the wake is stronger in the West. This may be the reason for stronger turbulent mixing. Within the zone of decelerated wind speed, the TKE is lower than outside the wakes.

5.3.4 Validation of WRF model simulations

Mesoscale modelling results obtained with WRF were validated with the observations (Siedersleben et al., 2018a,b). For the numerical simulations, three nested domains with a horizontal grid side of 15, 5 and 1.6 km were driven by ECMWF initial and lateral conditions. The representation of specific atmospheric and radiative processes is described in Siedersleben et al. (2018a). The parameterization of the wind park of Fitch et al. (2012)

https://doi.org/10.24355/dbbs.084-201906170934-0

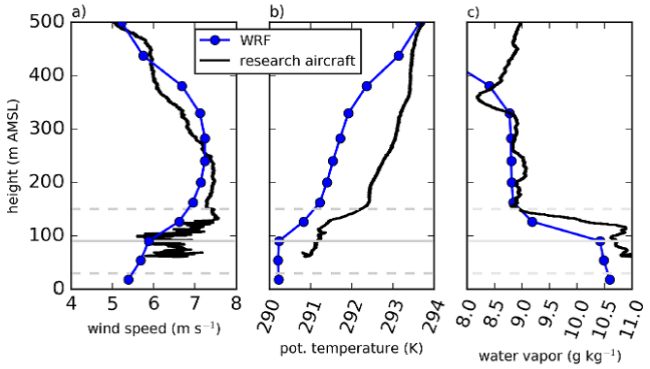

Figure 5.17: WRF simulations and airborne profiles of (a) wind speed, (b) potential temperature and (c) water vapour mixing ratio on 10 September 2016 at 08:00 UTC. (Siedersleben et al., 2018a)

is used, which includes the extraction of turbulent kinetic energy from the flow, and the wind park as a source of turbulence. With this parameterization, the atmospheric features observed in the wind park far field were well reproduced by the simulations (Siedersleben et al., 2018a). Therefore, WRF simulations were found to be a valid tool for analysing larger areas and the impact of far field wakes in wind park clusters that are being constructed. Although progress has been made for some studies investigating sites above land (Baas et al., 2018), very stable stratifications and associated LLJs are still difficult to reproduce correctly in numerical simulations (Sandu et al., 2013). This was found to be the weak point of the simulations. It can be seen in Fig. 5.17 that the model provides too low values of potential temperature and does not represent the stable stratification below hub height correctly (Siedersleben et al., 2018a, Lampert et al., 2018b). The general shape of the wind speed profile and the water vapour mixing ratio (up to an altitude of 400 m) agree well. The deviation of the potential temperature results from the coastal effect, and the non-equilibrium state of the ABL after the transition from the land surface to the open water.

5.3.5 Potential impact on local climate

The potential impact of wind parks on climate has been assessed by different studies. Observed changes in surface air temperature patterns have been reported for large onshore wind parks (Baidya and Traiteur, 2010, Zhou et al., 2012). Also numerical simulations suggest a systematic climate impact of wind parks, e.g. changes in precipitation patterns (Fiedler and Bukovsky, 2011), and a modification of atmospheric stability (Fitch et al., 2013, Lu and Porté-Agel, 2015). Other studies indicate that the climatic impact is weaker than the natural climate interannual variability (Vautard et al., 2014).

https://doi.org/10.24355/dbbs.084-201906170934-0

Airborne observations and mesoscale simulations confirmed that far field wakes were visible in an increased potential temperature and decreased water vapour mixing ratio for 5 out of 30 measurement flights in the far field of wakes at hub height (Fig. 5.18). For the analyses, the systematic temperature offset mentioned in Sect. 5.3.4 has been corrected with measured values. These wakes observed in the potential temperature and water vapour mixing ratio occurred only when a stable stratification was present at the altitude of the rotor blades or below. In these cases, warmer and drier air from above is mixed downwards and produces the changes in the wake properties (Siedersleben et al., 2018b).
During unstable stratification, enhanced cloud formation directly above the wind parks was observed during two flights (11 April 2017, 14 October 2017), which were transported downstream. The small cloud patches were difficult to discern, especially when other cloud layers above were present as well. Fig. 5.19 shows typical sky impressions during stable (left) and unstable conditions with cloud formation (right). For a systematic evaluation, the turbulent fluxes of sensible and latent heat upstream, above and downstream of a wind park are currently analysed.

5.3.6 Summary: Observations of far field wakes behind wind parks

For stable ABL stratifications, downstream wakes were observed by airborne measurements up to a distance of 55 km. Within the wake, a reduction of wind speed and a changed surface reflectivity were measured. At the edges of the wakes, there was enhanced turbulence. The first systematic airborne measurements in the far field of offshore wind parks are analysed by Emeis et al. (2016) and Platis et al. (2018). Under stable conditions within the altitude range of the rotor blades, air from above is mixed downwards by the motion of the wind turbines, resulting in a drier and warmer wake compared to the undisturbed boundary layer (Siedersleben et al., 2018b). Analyses of the airborne measurements in combination with WRF results show that an improvement of the simulations is needed to correctly represent upwind profiles of potential temperature (Siedersleben et al., 2018a). Further, the prediction of the energy output of a wind park for LLJ events requires the knowledge of wind speed profiles (Lampert et al., 2018b).

https://doi.org/10.24355/dbbs.084-201906170934-0

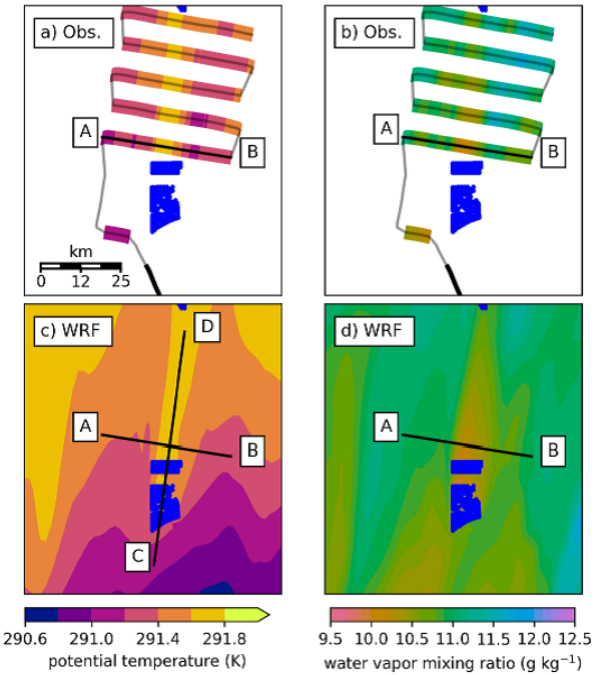

Figure 5.18: Airborne observations and WRF results of the measurement flight at hub height on 10 September 2016. (a) measurements of potential temperature (b) measurements of the water vapour mixing ratio (c) WRF simulations of potential temperature (d) WRF simulations of the water vapour mixing ratio. The individual wind turbines are indicated as blue dots. The cross section A-B was flown several times at different altitudes. (Siedersleben et al., 2018b)

https://doi.org/10.24355/dbbs.084-201906170934-0

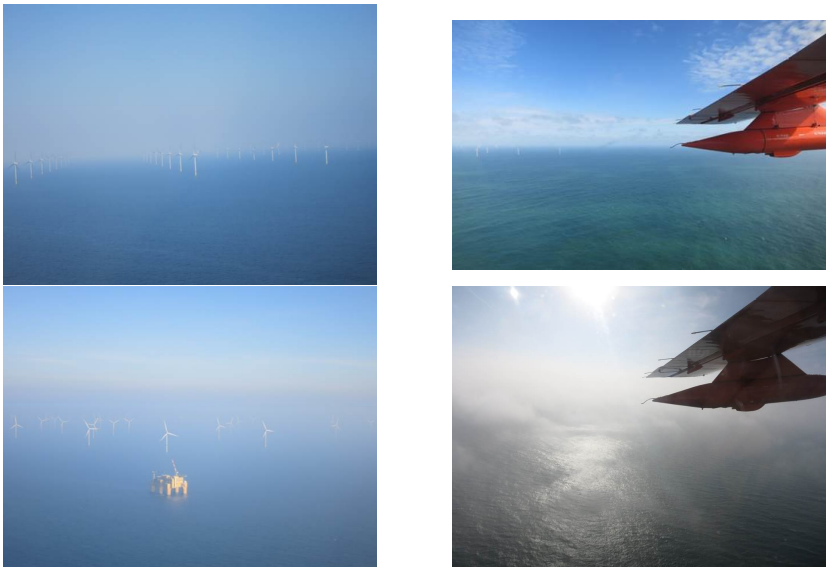

Figure 5.19: Photos obtained during the measurement flights on 9 April 2017 and 15 October 2017 under stable conditions (left) and on 11 April 2017 and 14 October 2017 under unstable conditions (right).

https://doi.org/10.24355/dbbs.084-201906170934-0

5.4 Fast humidity sensors for airborne latent heat fluxes (P1, P2, S1)

Latent heat fluxes are a measure of vertical moisture transport within the ABL. For these calculations, high frequency observations of humidity and vertical wind speed are needed (see Sect. 3.4).
The Institute of Flight Guidance is still operating two functional Lyman Alpha fast humidity sensors, one implemented in the Do-128 (P1, Sect. 2.1), the other in the Helipod (P2, Sect. 2.2). However, these sensors may quickly reach the end of their lifetime, and no spare parts or repair kits are available any more. The characterisation of such a sensor is of high importance for other research aircraft as well, e.g. the Polar 5 of the Alfred Wegener Institute, to make it possible to derive latent heat fluxes (Tetzlaff et al., 2015). Therefore, an alternative airborne humidity sensor with short response time has to be found to replace the Lyman Alpha in the future for airborne applications. Most important is the ability of the sensor to capture fast fluctuations with a spectral behaviour in agreement with Kolmogorov theory up to frequencies significantly exceeding 1 Hz. Long-term drift can be compensated by complementary filtering the signal with the output of another sensor with lower resolution but higher absolute accuracy (Sect. 3.1). The suitability of the LICOR hygrometers (Sect. 4.1) for airborne applications was investigated for different vibrational conditions. For this purpose, the spectral behaviour of Lyman Alpha and LICOR humidity sensors was analysed during a flight with the Do-128 and the Helipod. Further, the necessary measurement frequency for retrieving airborne latent heat fluxes for the specific flight and atmospheric conditions was retrieved. The results of two airborne experiments in Northern Germany and over the Lena River Delta are first presented in the following section. Then the data will be analysed and interpreted with the objective to retrieve the reliability of the fast humidity parameters. The results are published in Lampert et al. (2018a).

5.4.1 Airborne experiments

Do128 humidity intercomparison flight in Northern Germany

To find a suitable replacement in case of failure of the fast Lyman Alpha sensor, a humidity intercomparison flight was performed with the Do-128 (P1, see Sect. 2.1), additionally equipped with three LICOR sensors at different positions within the aircraft (S1, see Sect. 4.1). It is recalled that Li1 in the following refers to the open path LI-7500A, Li2 refers to the closed-path LI-7200, and Li3 refers to the closed-path LI-7500. All three LICOR sensors were factory calibrated before the flight. To analyse the impact of vibrations, acceleration sensors of type M355B04/03/02 and M356B18 of the company PCB Piezotronics Inc., US, were integrated along the x-axis (perpendicular to flight direction) and z-axis (upward directed) of the LICOR sensors. For the Li2, another acceleration sensor in y-direction (in flight direction along the aircraft and the sensors) was available.
The measurement flight on 23 October 2015 (see Fig. 5.20) was conducted above different terrain, including areas dominated by forest, by agricultural farmland, and above open water North of the East Frisian Islands at constant altitudes. For the analysis, the flight was sub-divided into six straight and level legs D1-D6 of 10 km length above terrain as homogeneous as possible (two each above forest, agricultural land and open water), which

https://doi.org/10.24355/dbbs.084-201906170934-0

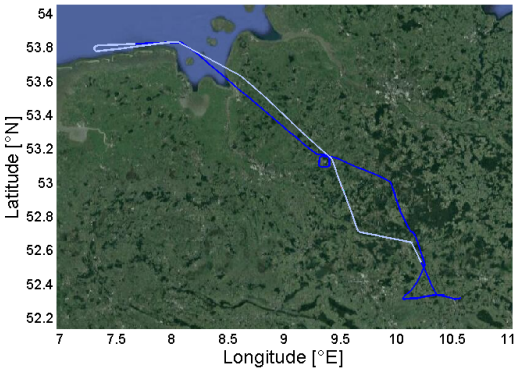

Figure 5.20: Flight track of the Do-128 aircraft in Northern Germany for the humidity comparison on 23 October 2015. Figure from Lampert et al. (2018a)

fullfill the requirements of Lenschow et al. (1994) for the sampling length. D1 above forest at an altitude of 430 m above mean sea level, D2 above agricultural land at an altitude of 430 m, D3 above agricultural land at 220 m altitude, D4 and D5 above open water at 100 m altitude, and D6 above forests at 270 m altitude. Apart from these short legs, a longer part of the flight was used for the sensor comparison (indicated in white in the flight track, Fig. 5.20). The part that was used for the instrumental comparison is shaded in grey in the time series of the measurements in Fig. 5.21. The flight took place under varying cloud conditions, mostly overcast with a cloud bottom at an altitude of around 1000 m. Above land, a neutrally stratified boundary layer was observed up to an altitude of around 1000 m, with a strong increase in potential temperature of 6 K at the altitude range from 1000 m to 1200 m. However, above the North Sea, the atmosphere was stably stratified. Therefore, significant latent heat fluxes were only observed above land. The latent heat fluxes were in the range of 100 $W m^{-2}$ above two of the sections. Above the North Sea, the latent heat fluxes were very small and even negative due to the stable stratification.

For synchronisation of the four fast humidity sensors (Lyman Alpha, Li1, Li2, Li3) onboard the Do128 located at different places, the time signal of the Lyman Alpha was used as reference (see Sect. 3.6). As mentioned in Sect. 4.1, the Lyman Alpha and the Li1 are located at the nose boom, the Li3 at the cabin roof, and the inlet of the Li2 is close to the Li3 on the cabin roof.

In Fig. 5.21, the time series of the altitude (a), the vertical wind speed (b), the water vapour mixing ratio of the five hygrometers (Humicap, Lyman Alpha, and three LICOR sensors, (c), the potential temperature (d), and a flag indicating invalid data (e) are displayed. There are several striking features: The stable stratification above the North Sea can be identified by the time interval of reduced turbulence before 13:00. Only during

https://doi.org/10.24355/dbbs.084-201906170934-0

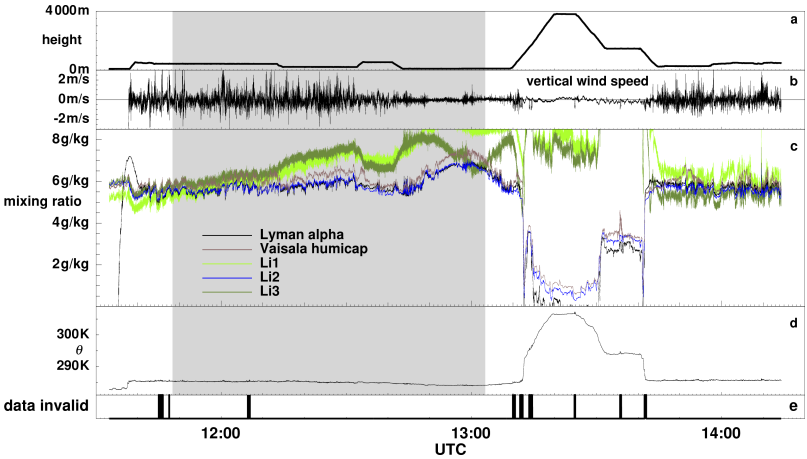

Figure 5.21: Overview of the flight with the Do128 on 23 October 2015. Subplot (a) shows the height, (b) the vertical wind speed, indicating the strength of atmospheric turbulence. Subplot (c) shows the time series of the mixing ratio measured by Lyman Alpha (black), Vaisala Humicap (purple), closed-path Li2 (blue), open-path Li1 at the nose boom (bright green), and closed-path Li3 on the cabin roof (olive). Subplot (d) provides the potential temperature. Subplot (e) shows the periods of invalid data, e.g. when radio communication disturbed the signals. For the spectral analysis, the part of the data shaded in grey were used, excluding segments with invalid data, e.g. disturbance by radio communication. Figure from Lampert et al. (2018a).

higher altitudes above the ABL, the turbulent fluctuations are less. The time series of the five hygrometers (c) differ significantly. The mixing ratio recorded by the Lyman Alpha sensor starts at very low values, as the system needs time to warm up. The Li1 and Li3 sensor have higher turbulent fluctuations than the Li2 and Lyman Alpha. Further, these two sensors exhibit a slowly drifting signal with time, which is most obvious during the time of the climb and flights at higher altitudes starting at around 13:15 UTC, showing a large disagreement with the other sensors. These effects will be analysed in detail in Sect. 5.4.2.

Helipod humidity intercomparison flight in the Lena River Delta, Siberia

A measurement campaign at the Lena River Delta, Siberia, was organised in 2014 by Prof. Dr. Torsten Sachs of the German Research Centre for Geosciences (GFZ). In a collaboration with the Institute of Flight Guidance, the Helipod was used for airborne flux measurements of methane, carbon dioxide, as well as sensible and latent heat. The Li3 deployed on the Helipod was factory calibrated before the measurement campaign, and

https://doi.org/10.24355/dbbs.084-201906170934-0

the signal of the Lyman Alpha was calibrated to the Li3 in the post processing.
Altogether, the campaign was divided into three parts during different seasons, with a total of seven flights with a duration between 1.5 and 2.5 h each. The first two flights were conducted in April, another three flights in May and June, and the last two flights in August. During the measurement flights, the Helipod was attached to a Russian Mi-8 helicopter by a 30 m rope. The flights were performed at a true airspeed of 40 m s^{-1} from the Research Station Samoylov Island in the Lena Delta, Siberia.
For the time period 29 April to 9 September 2014, an eddy covariance station was set up at Samoylov Station, and the latent heat fluxes of the flights in May/June and August can be compared to these continuous reference values.
The climate of the Lena Delta can be characterized as continental Arctic with a low mean temperature of -14.7° C and a low mean summer precipitation of 137 mm (Sachs et al., 2008). The annually averaged surface temperature of the permafrost soil is around -10° C, and the permafrost reaches a depth up to 600 m (Boike et al., 2008). The surface melting period starts around the beginning of June, and the vegetation period is restricted to mid June until mid September (Boike et al., 2008). The Western part of the Lena Delta is regularly flooded by the Lena River in spring, the Eastern part, located at slightly higher altitudes of 10 to 16 m above sea level, is only partly under water. It is characterized by wet polygonal tundra structures (Boike et al., 2008). In spring, typical values of the latent heat fluxes in the Lena Delta are around 10 to 12 W m^{-2}, for summer around 40 to 44 W m^{-2} (Langer et al., 2011).
The overall aim of the Helipod measurements was to study greenhouse gas emissions on a scale of up to 100 km to investigate the spatial variability, and to analyse, how representative are the continuous emission measurements on local scales on a climatically relevant sub-regional scale.
The Helipod flight used for the spectral analysis took place on 14 August 2014, when seasonal thawing of the active layer on top of the permafrost was still in progress. The roundtrip flight pattern followed a 100 km horizontal leg at 100 m altitude in north-western direction with vertical profiles up to 1500 m altitude at both ends of the leg. The atmosphere was neutrally stratified in the lowermost 150 m, then slightly stable up to 1000 m (increase in potential temperature smaller than 1 K from the surface up to that altitude), and the ABL top was evident by an increase in potential temperature at 1000 m altitude. On that day, there were conditions nearly free of clouds at the beginning, with a near-surface air temperature around 17 °C and southerly wind with a speed of 5 m s^{-1} near ground. The mean wind speed at the altitude of the Helipod transects was 8 m s^{-1}, and the mean wind direction at that altitude was 180 °. For this instrumental intercomparison, the first long flight transect from Samoylov Station to Arga-Muora is analysed (Fig. 5.22). On the way back, short rain showers were encountered. Fig. 5.23 shows the time series of the altitude (a), the vertical wind speed (b), the water vapour mixing ratio derived from Lyman Alpha, Li3 and Humicap (c), potential temperature (d) and a flag for valid data (e).
In the time series of the water vapour mixing ratio, the measurements of the Lyman Alpha and the Li3 agree within ± 0.1 g kg^{-1}, except during climb and descent and a rain shower shortly after 8:00 UTC, indicated with the invalid data flag. The Humicap hygrometer follows the temporal behaviour of the other sensors, but has a constant offset of around -0.5 g kg^{-1} during the entire flight. Further a flight segment of 10 km length obtained on

https://doi.org/10.24355/dbbs.084-201906170934-0

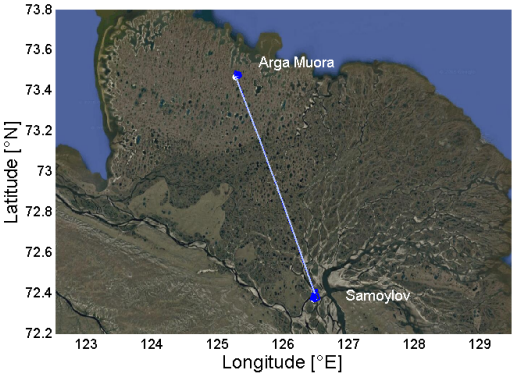

Figure 5.22: Flight track of the Helipod in the Lena Delta for the three measurement flight on 14 August 2014. The flight started at Samoylov Station and went towards Arga-Muora in the North-West. The part of the flight used for the instrumental intercomparison is displayed in white. Figure from Lampert et al. (2018a)

22 April 2014 is used to demonstrate the impact of the sampling frequency.

https://doi.org/10.24355/dbbs.084-201906170934-0

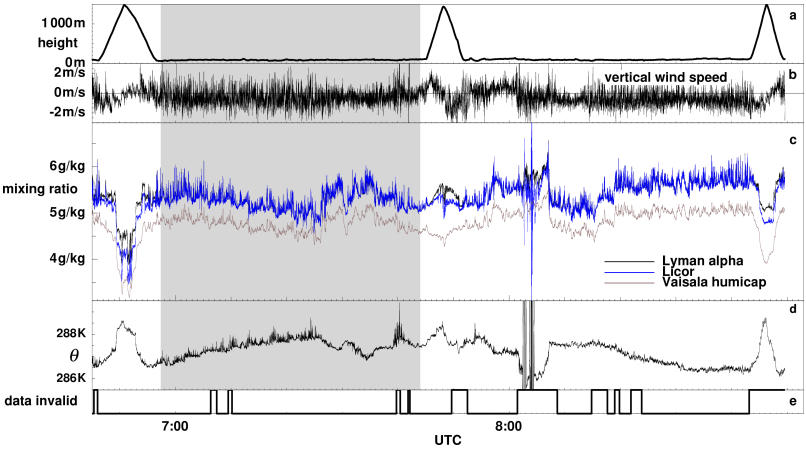

Figure 5.23: Overview of the flight with the Helipod on 14 August 2014. Subplot (a) shows the altitude, (b) the vertical wind speed, indicating the strength of atmospheric turbulence. Subplot (c) shows the time series of the mixing ratio measured by Lyman Alpha (black), Vaisala Humicap (purple) and the open-path Li3 (blue). Subplot (d) represents the potential temperature. Subplot (e) shows the parts of the flight with data that was excluded from the analysis for various reasons (e.g. impact of rain). For the spectral analysis, the part of the data shaded in grey were used, excluding segments indicated in the last plot. Figure from Lampert et al. (2018a)

5.4.2 Analysis and interpretation of vibrations, humidity spectra and latent heat fluxes

Impact of vibrations on the LICOR sensors

The time series of the mixing ratio for the Do128 flight (see Fig. 5.21 above) shows the general behaviour of the LICOR sensors, the slow Humicap and the fast Lyman Alpha sensor. The time periods affected by radio communication were excluded for further analyses, as they occasionally induce artificial spikes on the Lyman Alpha sensor. The data used for calculating the spectra are shaded in grey. They were chosen to exclude the flights at higher altitude, where the signal of the Lyman Alpha differs significantly from the other sensors. Under these different pressure conditions, a different sensitivity range would be necessary, which was not adapted during the flight. For the data of the LICOR sensors, different effects can be observed:

- The signals of the open path sensors Li1 and Li3 contain a higher level of noise compared to the closed path Li2 system and the signal of the Lyman Alpha.

https://doi.org/10.24355/dbbs.084-201906170934-0

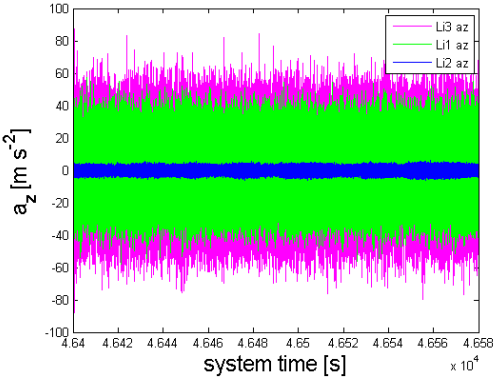

Figure 5.24: Time series of the accelerations in z direction of the three LICOR sensors during a flight section of 3 min duration on 23 October 2013, illustrating the vibrations the LICOR sensors were exposed to. The flight section took place above agricultural land at 220 m altitude. The acceleration measurements of this flight section are representative for other flight sections at different, but constant altitude. The acceleration measurements at the Li1 are shown in green, at the Li2 in blue, and at the Li3 in magenta. Figure from Lampert et al. (2018a)

- Changes in altitude affect the signals of Li1 and Li3, and the absolute values of the mixing ratio do not follow the behaviour of the Li2 and the Humicap. This might be caused by changing vibration environments due to different power settings.

- There is a general slow drift in the signal of the open path sensors Li1 and Li3, which does not follow the trend of the closed path Li2 sensor, the signal of Lyman Alpha, and Humicap.

Differences are apparent in the time series of the vibrations (Fig. 5.24): The amplitude of acceleration in z-direction is around $50\,\mathrm{m\,s^{-2}}$ for the Li3, around $40\,\mathrm{m\,s^{-2}}$ for the Li1 and around $3\,\mathrm{m\,s^{-2}}$ for the Li2 sensor. The example shows a small flight section of 3 min, but is representative for sections of this length at constant altitude.
The acceleration spectra for all three sensors in y- and z-direction (along sensor and aircraft axis, and vertical direction) as well as x-direction (perpendicular to sensor and flight direction) for the Li2 sensor are shown in Fig. 5.25 for a short flight section of 3 min. Strong and sharp vibration peaks at distinguished frequencies were recorded at the locations of all sensors, and there are differences in the broadband features.
Generally, the acceleration at high frequencies (exceeding 200 Hz) is several orders of magnitude lower for the Li2 sensor compared to the Li1 and Li3 sensors. This feature gets more pronounced for frequencies exceeding 1000 Hz. The amplitude of vibrations con-

https://doi.org/10.24355/dbbs.084-201906170934-0

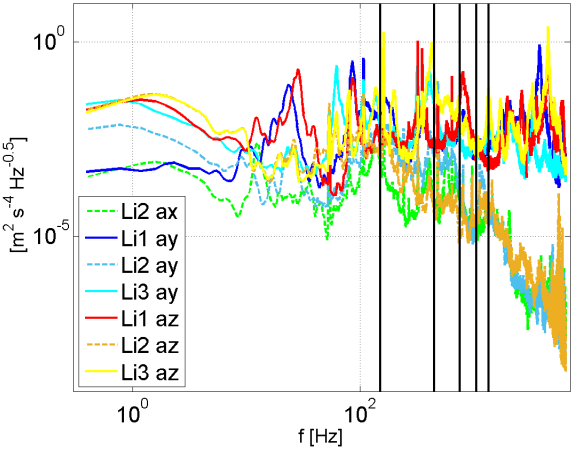

Figure 5.25: Acceleration spectra measured at the three humidity sensors Li1, Li2 and Li3 during the Do128 flight on 23 October 2015 for the same flight section as in Fig.5.24. The colours blue and red indicate the accelerations of Li1 (y and z direction, respectively), the colours cyan and yellow indicate the accelerations of Li3 (y and z direction, respectively), and the dashed lines in green, bright blue and ocher indicate the accelerations of Li2 (x, y and z direction). The vertical black bars indicate the critical frequencies of 150 Hz and odd harmonics of 450, 750, 1050 and 1350 Hz according to the manufacturer. Figure from Lampert et al. (2018a)

tained within individual peaks is higher for the Li1 and Li3 sensor compared to the Li2 sensor. In Fig. 5.25, the critical frequencies of 150 Hz and higher harmonics, as specified by the manufacturer, are indicated by vertical black lines. Especially around 450 Hz it can be seen that the vibration level of the Li3 is more than an order of magnitude higher than the vibration level of the Li1. This feature is observed during all flight legs analysed here, persistent throughout each flight leg. The high level of vibrations at the critical frequencies and potential impact on the internal signal processing could be an explanation for the different humidity spectra shown in the following.

Spectral characterisation of hygrometers

The above mentioned properties of the sensors are reflected in the spectra of the water vapour mixing ratio, shown in Fig. 5.26 for each humidity signal. The sloped lines represent the -5/3 drop-off expected in the inertial subrange. Between 0.003 and 0.3 Hz all sensors follow the Kolmogorov prediction (Kolmogorov, 1941), and those of the Lyman

https://doi.org/10.24355/dbbs.084-201906170934-0

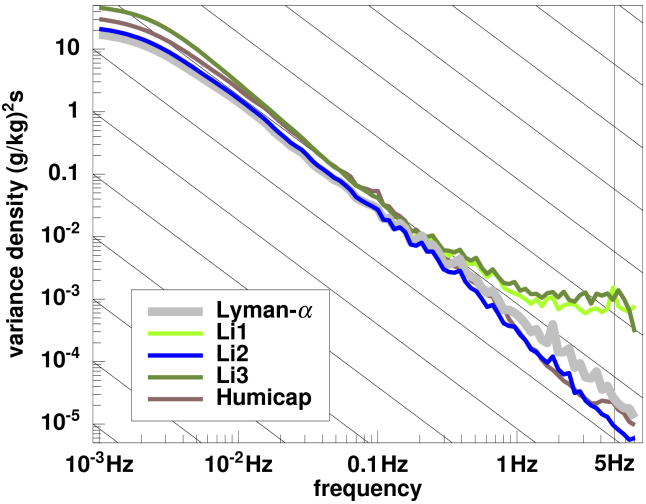

Figure 5.26: Powerspectra (variance density) of the different humidity sensors on the Do128, Li1 in bright green, Li2 in blue, Li3 in olive, Lyman Alpha in grey, Humicap in purple. The spectra are averaged over the data of the time series shaded in grey in Fig.5.21. The lines have the slope of -5/3 according to Kolmogorov theory. Figure from Lampert et al. (2018a)

Alpha and Li2 remain constant for a further decade, while Li1 and Li3 level off indicating a substantial level of white noise superimposed on the humidity signal. The Humicap spectrum gradually decreases slightly faster.

Overall, the Lyman Alpha spectrum most closely behaves as expected from theory, and the Li2 spectrum is very similar but drops off marginally faster beyond 1 Hz. This behaviour can be attributed to somewhat increased dampening due to longer inlet tubes in comparison to those for the Lyman Alpha.

At low frequencies, the Vaisala Humicap and even more the Li3 sensor show higher variances. It will be shown in the following that this variance is differently correlated with the vertical wind velocity, which has implications for the flux calculation.

As the Lyman Alpha humidity sensor has been used widely in turbulence studies over decades, it is taken as a reference to compare the behaviour of the other sensors. Cospectra between each of these other sensors and the Lyman Alpha are calculated.

Based on the grey shaded data set of Fig. 5.21, Fig. 5.27 shows the coherence and the phase of the different LICOR sensors with the Lyman Alpha. Li2 provides the best coherence with Lyman Alpha, virtually equal to one over a large frequency range of three decades. It only drops off for frequencies beyond 1 Hz due to the spatial separation of the two sensors. No phase difference is observed over the same frequency range. In the phase spectrum the

https://doi.org/10.24355/dbbs.084-201906170934-0

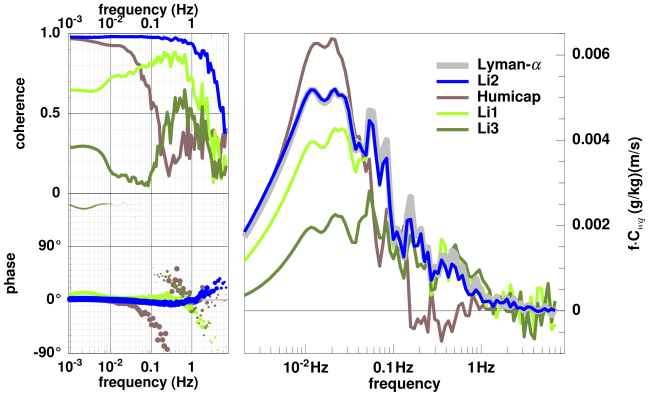

Figure 5.27: Left: Phase and coherence of the different LICOR humidity sensors on the Do128 related to the Lyman Alpha sensor, with the same colour code as in Fig. 5.26. In the diagram of phase shift, higher coherence is represented by larger dot size. Right: Cospectra of humidity from the different sensors and vertical wind speed on the Do128, multiplied by the frequency. The area under the curves is proportional to the humidity fluxes. The data are averaged over the data of the time series shaded in grey in Fig. 5.21. Figure from Lampert et al. (2018a)

coherence is coded in the thickness of the dots, as a phase can only be interpreted if a significant coherence between the signals is present. The marginally positive phase between Li2 and Lyman Alpha is a result of the advancement of the Li2 signal over 0.315 s. This constant shift can only approximate the more complex difference in the high-frequency response behaviour between Li2 and Lyman Alpha due to spacing and tubing. A smaller advancement, however, leads to reduced coherence and a trailing phase shift of Li2 for frequencies below 1 Hz. The other two LICOR sensors (Li1 and Li3) have far less coherence with the Lyman Alpha. At low frequencies this reflects the drift of both vibration affected sensors, and at high frequencies the noise fades more coherence that might exist. Note that for all three LICOR sensors the coherence inversely correlates with the amount of vibration the sensors are exposed to. The response behaviour of the Vaisala Humicap is more complex. At low frequencies (< 0.01 Hz) the signal agrees reasonably well with the Lyman Alpha. Then the coherence decreases with increasing frequency. The phase shift disappears around 0.4 Hz, but the level of coherence remains lower. To assess the sensor behaviour on the moisture flux calculation, Figure 5.27 (right) shows the covariance of the vertical wind speed and the different humidity sensors after correction of the time lag. The spectra are multiplied by the frequency, thus the area below the curves is proportional to the humidity flux. Flux estimates based on Li2 and Lyman Alpha reasonably agree, but those calculated by the vibration affected LICOR sensors are too low, most pronounced for Li3. The Humicap shows an interesting behaviour: overestimation on a scale of minutes

https://doi.org/10.24355/dbbs.084-201906170934-0

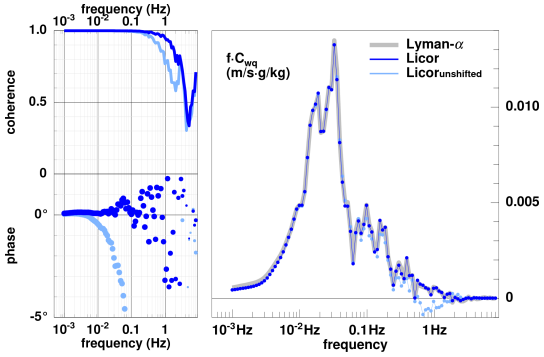

Figure 5.28: Phase shift and coherence spectra of the shifted (darker blue) and unshifted (light blue) signal of the LICOR sensor on the Helipod (left) and cospectra of humidity from the different sensors and vertical wind speed multiplied by the frequency (right) on the Helipod flight. The area under the curves is proportional to the humidity fluxes. The flight part indicated in the time series in Fig. 5.23 in grey was used. Figure from Lampert et al. (2018a)

(0.02 Hz) and underestimation for higher frequencies, both of which compensate to a certain degree. This behaviour seems to be a specific property of the Vaisala Humicap sensor. The latent heat flux determined with the Humicap amounts to 95% of the reference value determined with the Lyman Alpha. Thus, for moderate conditions (10-20°C, humidity values typical for midlatitudes), the Humicap can be used for determining airborne latent heat fluxes with an acceptable error bar below 5%. However, the response function of the Humicap is asymmetric, with a different response time for decreasing and increasing humidity (Sect. 3.1), and the response time becomes significantly slower for cold conditions like in the Arctic, where the sensor is not suitable for deriving latent heat fluxes.

For the Helipod flight, Fig. 5.28 (left) shows the spectra of coherence and phase of the LI7500 signal (with and without time correction) against the Lyman Alpha. For a frequency of up to 3 Hz, the coherence for the time corrected signal is higher than 0.8, and the phase shift around 0 °, thus the agreement of the two signals is high. The plot on the right represents the humidity flux for both sensors, i.e. the covariance spectra of the humidity and the vertical wind speed component. The areas under the curves are again proportional to the humidity fluxes. The Lyman Alpha and LICOR signals agree perfectly in the frequency range up to 2 Hz. For higher frequencies, the humidity flux is negligible anyway. The effect of the time correction for the humidity fluxes can be seen for frequencies exceeding 0.2 Hz: There are differences in the area under the lines representing the time corrected and uncorrected values. The overall effect is in the range of few percent. As the LI7500 used on the Helipod flew on the Do128 as well (Li3), the excellent agreement with the Lyman Alpha here demonstrates that the vibrations of the Do128 are the main reason

https://doi.org/10.24355/dbbs.084-201906170934-0

for poor performance there. The vibrations depend on the location within the aircraft, and on the applied insulation against vibrations.

Latent heat fluxes and necessary measurement frequency

For the Do128 flight, humidity fluxes as calculated by the five different hygrometers was compared. In Fig. 5.29 the integrated covariance spectra (called ogives, see e.g. Sievers et al., 2015) are shown, normalised by the integral of the cospectrum of w and the Lyman Alpha humidity. With the closed-path Li2, 98.1% of the Lyman Alpha value is reached, the small high frequency loss is due to different sensor spacing and tubing. The vibration affected open-path LICOR sensors reach 47% and 83% of the Lyman Alpha value of latent heat fluxes, which is not suitable for measurements.
It can be concluded from Fig. 5.27 and Fig. 5.28 that the fluxes for frequencies exceeding 2 Hz are negligible for these specific flight conditions, an air speed of 70 m s^{-1}, altitude of 200 - 400 m (Do128 flight), and altitudes of 100 m and at a lower true air speed of 40 m s^{-1} (Helipod flight) and the specific surface properties. This is different to flux measurements near ground, where high resolution sampling and close sensor spacing are essential (Caughey et al., 1979, Kaimal and Finnigan, 1994, Bange et al., 2002). The scale of eddies corresponding to the frequency of 1 Hz and the airspeed of 70 m s^{-1} is around 70 m. Contributions from eddies smaller than the size of few 10 m are negligible. This information is visible in the cospectra and in the ogive functions. Therefore, the sampling frequency of 20 Hz is sufficient for airborne turbulent humidity fluxes.
To further demonstrate the measurement frequency necessary for calculating turbulent fluxes of latent heat and capture the relevant small scales contributing to the overall result, the data were filtered. The wind and Lyman Alpha humidity data are available at a frequency of 500 Hz. Different cutoff frequencies were applied for the low pass Butterworth filter, and then the latent heat fluxes for the same flight section were calculated. The results are provided in the following two tables.

Table 5.3: Turbulent latent heat fluxes W m^{-2} of Helipod after filtering the humidity and wind data with different low pass cutoff frequencies between 500 Hz (unfiltered data) and 2 Hz.

Cutoff frequency [Hz]	500	200	100	50	10	5	2
Leg A1	11.2	11.2	11.2	11.2	11.2	11.2	11
Leg A2	10.3	10.3	10.3	10.3	10.3	10.3	10.1
Leg A3	2.4	2.4	2.4	2.4	2.5	2.5	2.3
Leg A4	11.7	11.7	11.7	11.7	11.8	11.8	11.6
Leg A5	16.2	16.2	16.2	16.2	16.2	16.2	16

From the tables it can be deduced that there is almost no change in the latent heat fluxes for a low pass frequency larger than 5 Hz. Also for the data filtered with 2 Hz, only a slight reduction of the calculated latent heat fluxes below 9% was observed. For data with lower temporal resolution (below 1 Hz), the calculated latent heat fluxes decreased significantly. Therefore it seems necessary to employ a humidity sensor with an effective measurement frequency of at least 5 Hz. This criterion is fulfilled by the LICOR sensors, which should be

https://doi.org/10.24355/dbbs.084-201906170934-0

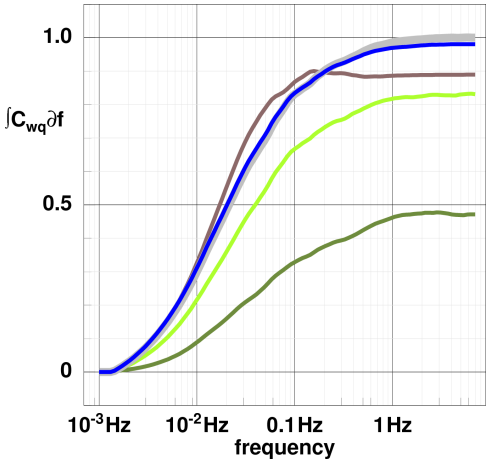

Figure 5.29: Ogive functions (integral over the latent heat fluxes) for the Do128 flight on 23 October 2015. The colours indicate the same humidity sensors as in Fig. 5.26. Figure from Lampert et al. (2018a)

Table 5.4: Turbulent latent heat fluxes in $\mathrm{W\,m^{-2}}$ of Helipod after filtering the humidity and wind data with different low pass cutoff frequencies between 1 Hz and 0.01 Hz.

Cutoff frequency [Hz]	1	0.5	0.2	0.1	0.05	0.02	0.01
Leg A1	10.5	9.6	8.1	5.7	3.5	2.7	1.8
Leg A2	9.6	8.7	6.3	3.2	0.8	-0.1	0.4
Leg A3	1.8	0.6	-2.7	-7.1	-10.4	-11.3	-12.9
Leg A4	11.1	10	6.1	1.2	-1.7	-2.2	-2.6
Leg A5	15.7	14.6	10.5	4.7	-1.7	-4.8	-3.8

an adequate replacement for the Lyman Alpha sensor from the point of view of temporal resolution. For the air speed of $40\,\mathrm{m\,s^{-1}}$, the measurement frequency of 5 Hz corresponds to a horizontal scale of around 8 m. This indicates that turbulent humidity fluctuations do play a role in the scale of meters for a flight altitude of 100 m. No significant contributions to the latent heat fluxes is transported into the atmosphere on smaller scales.

5.4.3 Recommendation for airborne applications of LICOR sensors

For calculating turbulent fluxes, the best temporal correlation of the sensors has to be determined first. The time shifts that were determined are not negligible and have to be

https://doi.org/10.24355/dbbs.084-201906170934-0

taken into account. This is a standard procedure in the flux community (Moore, 1986). Time delays for the LICOR sensors are partly caused by internal processing, partly by different locations of the sensors and tube lengths.
For the Do128 application, three different LICOR sensors were subject to different vibration levels. For the Li1 and Li3 sensors, installed without particular insulation agains vibrations, the correlation with the Lyman Alpha signal was significantly lower than for the Li2 sensor, which was installed isolated against vibrations. The covariance spectra of the vibration affected humidity measurements of the Li1 and Li3 sensors resulted in larger deviations of the latent heat fluxes compared to the latent heat fluxes based on the Lyman Alpha sensor. The vibration-isolated Li2 sensor showing high correlation with the Lyman Alpha sensor resulted in comparable latent heat fluxes. However, the spectral behaviour of the vibrations had no direct linear impact on the humidity spectra of the Li1 and Li3 sensors, but the relationship is more complex. This is currently subject to more detailed investigations.
For the Helipod application with lower vibrations, the humidity fluxes derived from the Lyman Alpha and the open-path LICOR sensor (Li3) agreed very well after careful sensor calibration to absolute values, and correction of the time lag. Altogether, both open-path and closed-path LICOR sensors are suitable high-resolution hygrometers for airborne applications, if the vibrations are low, e.g. by installing the sensors isolated against vibrations. In summary, some precautions have to be taken for employing a LICOR sensor for airborne turbulent humidity flux measurements. Especially the level of vibrations and its impact on the measurements should be evaluated critically, and the spectra of the measurements should be checked for plausibility. Especially for small fluxes, the relative error might be significant. Generally the temporal resolution of the LICOR sensors of 20 Hz is sufficient for humidity flux calculations, as the contribution of frequencies above approximately 2 Hz is negligible, so an oversampling of factor 10 for a sufficient amplitude retrieval is provided. Slight rain had a negative impact on the signals of both the Lyman Alpha and the LICOR sensors as installed on the Helipod.

5.4.4 Summary: Airborne application of LICOR hygrometers for latent heat fluxes

Both the open-path and closed-path LICOR hygrometers are suitable for airborne measurements of latent heat fluxes, if they are installed insulated against vibrations. In this case, the spectral behaviour agrees well with the Lyman Alpha. Therefore LICOR sensors can be used as an alternative to replace the standard Lyman Alpha hygrometer. Vibrations have a strong impact on the absolute signal of the sensors, which cannot be corrected. Besides vibrations, rain and condensing conditions should be avoided, as the signal of the LICOR sensors is strongly affected. The sampling frequency necessary for deriving latent heat fluxes, depending on amospheric conditions, altitude and air speed, was around 2-5 Hz in the observed cases. The LICOR sensors with a frequency of 20 Hz therefore comply with the required sampling frequency. The results are published in Lampert et al. (2018a).

https://doi.org/10.24355/dbbs.084-201906170934-0

5.5 New particle formation (P4, S2)

There is still large uncertainty about the mechanisms that lead to new particle formation (NPF) events. The hypothesis to be investigated with ALADINA was that new particles form in the residual layer above the ground-based inversion during the morning transition, and can only be measured by ground-based observatories when turbulent mixing is enabled to transport downwards the freshly formed particles. Therefore, events of NPF may be underestimated by analysing ground-based observations alone. Further, NPF events were observed during untypical conditions, with overcast sky and low concentrations of precursor gases measured at ground. In this section, three different cases are presented where NPF was initiated in the residual layer. In one case, the newly formed particles were not detected by ground-based instruments at all, published by Altstädter et al. (2015). The second case describes a typical situation favorable for NPF, where NPF started above the ground-based inversion and was mixed to the surface, published by Platis et al. (2015). During the third case, NPF took place sporadically in cloud gaps, and intermittent observations of nucleation mode particles were observed at ground (Altstädter et al., 2018a).

5.5.1 Location and instrumentation of the study site

The ALADINA measurements presented here were performed at the air chemistry observatory of TROPOS in Melpitz, around 40 km North-East of Leipzig (Altstädter et al., 2015). The first case was observed on 9 October 2013, the second on 4 April 2014, and the third on 21 June 2015, therefore during different seasons. The site is surrounded by flat grass and agricultural land (Spindler et al., 2013). The measurement site is characteristic for rural continental air masses (Herrmann et al., 2006). As Melpitz belongs to the Global Atmosphere Watch (GAW), European Monitoring and Evaluation Programme (EMEP) and Aerosols, Clouds, and Trace gases Research InfraStructure (ACTRIS) networks, permanent extensive instrumentation for aerosol, trace gases and meteorological parameters is available (Wehner et al., 2010). This provides the ideal background for embedding the airborne ALADINA observations.
The following data were used for the analysis: Meteorological data of temperature, humidity, wind and radiation provide the basic background information. Aerosol instruments include several condensation particle counters with different lower detection threshold diameter. Further, a NAIS (Neutral Cluster and Air Ion Spectrometer, Kulmala et al., 2007) and TSMPS (Twin Differential Mobility Particle Sizer, Wiedensohler et al., 2012) are used for the data interpretation. These instruments provide scans of the aerosol number concentration for the size range 3 nm to 10 μm (TSMPS, every 20 min) and 0.8 to 40 nm (NAIS, every 3 min). The phenomenon of NPF has been analysed in detail based on the Melpitz data (e.g., Siebert et al., 2004, Wehner et al., 2007). Typically, NPF was observed during the morning transition in spring and summer (Birmili and Wiedensohler, 2000, Birmili et al., 2001). On average, about every third day provides favorable conditions for the effect to be observed (Jaatinen et al., 2009).

5.5.2 NPF in the residual layer only

A first demonstration of the ALADINA system was performed in October 2013 (Altstädter et al., 2015). On 9 October 2013, a vertical profile obtained at 08:37 UTC revealed the fol-

https://doi.org/10.24355/dbbs.084-201906170934-0

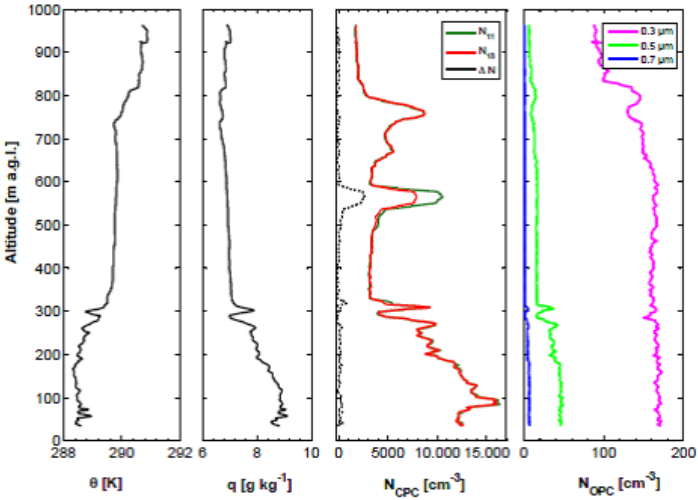

Figure 5.30: Vertical profile obtained on 9 October 2013, 08:37 UTC. The subplots show (a) the potential temperature [K], (b) the water vapour mixing ratio q $[g\,kg^{-1}]$, (c) the number concentration of the two CPC (N11 and N18) as well as the difference ΔN $[cm^{-3}]$, (d) the number concentration measured by the OPC $[cm^{-3}]$. Figure from Altstädter et al. (2015).

lowing atmospheric situation: The atmospheric boundary layer was neutrally stratified up to an altitude of around 300 m with the potential temperature almost constant (Fig. 5.30). At 300 m, a small temperature inversion can be seen. Below the temperature inversion, the water vapour mixing ratio is higher compared to the values above the inversion. Further, the particle number concentration below the inversion is enhanced. The two CPCs with different lower detection threshold diameter, as shown in Fig. 4.3, are in good agreement. This means that no particles in the nucleation mode were present. However, at an altitude of around 550-600 m, the particle number concentration of the two CPCs reveal a significant difference of 2000 cm^{-3}. Therefore, within a confined vertical altitude range, an NPF event was recorded. No correlation with the parameters temperature and humidity were observed in this case. At ground, no NPF events were evident, as can be seen in Fig. 5.31. The highest total particle number concentration was observed in the size range around 30 to 100 nm diameter during the whole day (Fig. 5.31).

https://doi.org/10.24355/dbbs.084-201906170934-0

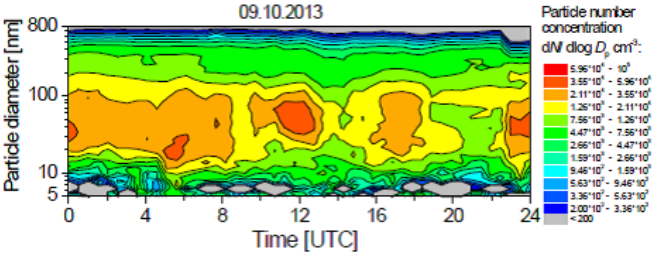

Figure 5.31: Time series of the aerosol size distribution measured with a TSMPS on 9 October 2013. In the size range of small particles, no enhanced concentrations were recorded. Figure from Altstädter et al. (2015).

5.5.3 NPF and downward mixing

The process of freshly formed particles mixed downwards was observed by consecutive profiling on another measurement day, 3 April 2014 (Platis et al., 2015). ALADINA measurements were performed under almost cloud free conditions with wind speed below 4 m s^{-1}. Therefore, the measurements took place under favorable conditions for NPF (see Sect. 1.2.3), making the observation of a "banana shape" aerosol size distribution in the daily development very likely (Heintzenberg et al., 2007). The temporal development of the potential temperature shows a typical morning transition (Wildmann et al., 2015) from a stably stratified boundary layer with a strong temperature inversion of 10 K in the lowermost 200 m (Fig. 5.32, dark blue line) to a turbulently mixed ABL. At 10:37 UTC, the mixing processes penetrated from ground into the residual layer, and the temperature inversion at 200 m altitude was heated and dissolved completely.

The development of the CPC profiles of total aerosol number concentrations are presented in Fig. 5.33. The black line (CPC1) represents the number concentration for particles with a diameter exceeding 5 nm, the red one for particles with a diameter exceeding 10 nm (CPC2). At the beginning of the measurements, the particle number concentrations agree rather well. At 09:29 UTC, the concentrations of the CPC observing smaller particles (black line) are clearly enhanced at an altitude of around 400 m. For the next time steps, the concentration differences of the two CPCs are more pronounced. From 10:04 UTC on, the freshly formed particles appear to spread down, reaching a lower altitude of 300 m. At 10:36 UTC, the new particles are mixed down throughout the former temperature inversion to the ground. At the same time, ground-based observations showed evidence of enhanced particle number concentrations in the nucleation mode particle size range (Fig. 5.34). Simultaneously, the ground-based SO_2 concentration increased as well. This emphasizes the hypothesis that NPF processes take place at higher altitudes, without local sources of precursor gases.

For NPF, photochemical processes in the RL were enabled by high solar irradiance, and an enhanced concentration of SO_2 was available for NPF, which was not present near ground in the stable ABL. To prove that the observed NPF at ground can be explained by

https://doi.org/10.24355/dbbs.084-201906170934-0

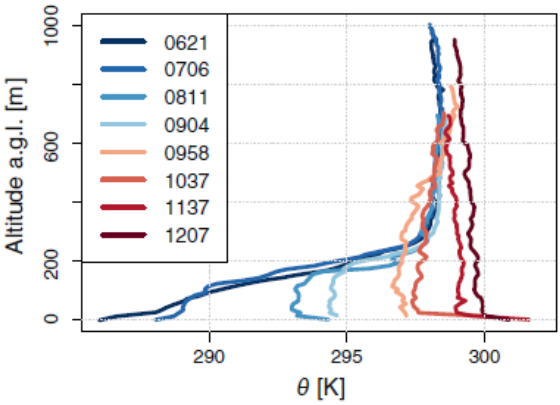

Figure 5.32: Vertical profiles of potential temperature [K] during the morning transition observed on 3 April 2014 between 06:21 UTC and 12:07 UTC. Figure from Platis et al. (2015).

the vertical downward transport of freshly formed particles, and no additional horizontal advection is needed to reach the observed number concentrations, the method of Wehner et al. (2010) can be applied:
The mean eddy dissipation rate for the altitude interval 200 to 600 m was calculated as described in Sect. 3.5, resulting in a value of approximately $\bar{\epsilon} = 10^{-3}\, m^2\, s^{-3}$. The time τ_{mix} which is needed for mixing down particles from an alitude z =500 m by turbulent transport can then be estimated as

$$\tau_{mix} \approx (\frac{z^2}{\bar{\epsilon}})^{1/3} \approx 630\, s \approx 10\, min \tag{5.1}$$

This is in agreement with the observations of a fast increase of both nucleation mode particles and SO_2. In contrast, local NPF events initiated near the surface would take a longer time due to the typical growth rate of around a few nm per hour (Kulmala et al., 2004). However, this does not explain the fast increase of particles in the size range of 5 to 10 nm observed at ground (Fig. 5.34).

5.5.4 NPF with sporadic downward transport

During the third case, ALADINA measurements were performed on 21 June 2015. The sky was overcast with low-level stratocumulus cloud at altitudes around 500-2300 m as indicated by continuous Ceilometer observations. Cloud gaps occurred irregularly. The concentrations of the most important precursor gas SO_2 were in the range of 0.8 - 1.6 $\mu g\, m^{-3}$ for most of the day, in contrast to a background value of 4 - 7 $\mu g\, m^{-3}$ and a concentration up to 10.5 $\mu g\, m^{-3}$ during the NPF event for the second case (Sect. 5.5.3). Therefore, the

https://doi.org/10.24355/dbbs.084-201906170934-0

atmospheric conditions would be classified as unfavorable, thus the observation of NPF with ground-based instruments highly unlikely. However, other studies confirm that there is a broad range of conditions where NPF occurs, it seems not to be limited by single factors like enhanced concentration of precursor gases or low condensation sink (Rose et al., 2015). ALADINA repeated profiles observed a high variability of the NPF number concentration (Fig. 5.35). Within 13 min, the number concentration in the nucleation mode size range varied between 5000 cm^{-3} and 16000 cm^{-3} at an altitude above 450 m. This high temporal variability is confirmed by ground-based observations (Fig. 5.36.) Small bursts of NPF are evident around 08:15 UTC and later again sporadically at 10:00-15:00 UTC. As interpretation, it seems that at cloud edges, an enhanced concentration of freshly formed aerosols was observed in the residual layer. They were mixed down intermittently, resulting in the so-called "apple" type of NPF events.

5.5.5 Summary: New particle formation and thermodynamic structure

In this section it was shown how the formation of new particles and the thermodynamic structure are related. The observations served to verify the hypothesis that NPF is a phenomenon occurring aloft, with processes initiated in the residual layer. Three cases were analysed, one where no NPF at all was observed at ground level, one where the NPF was recorded at ground more than 1 h after the observation of NPF aloft, when the vertical mixing throughout the ABL allowed the vertical exchange down to the surface, and one under unfavorable conditions, when only intermittent NPF was observed at ground.
According to the observations, new particles may form within the residual layer above a stably stratified or well-mixed ABL under a large variety of atmospheric conditions: not only during conditions classified as "favourable", when an enhanced concentration of precursor gases, high solar radiation, and only few pre-existing coarse mode particles are available. Instead, NPF was observed under "unfavourable" conditions with overcast sky and low concentration of precursor gases. In all these cases, new particle formation was initiated aloft, a process which cannot be monitored directly near ground. Only when the thermodynamically stable layer is heated up to allow vertical mixing processes between the surface and the residual layer, the particles are transported down and can then be detected by routine observatories and aerosol monitoring networks. This may underestimate the importance of NPF as an aerosol source. The results are published in Platis et al. (2015), Altstädter et al. (2015, 2018a).

https://doi.org/10.24355/dbbs.084-201906170934-0

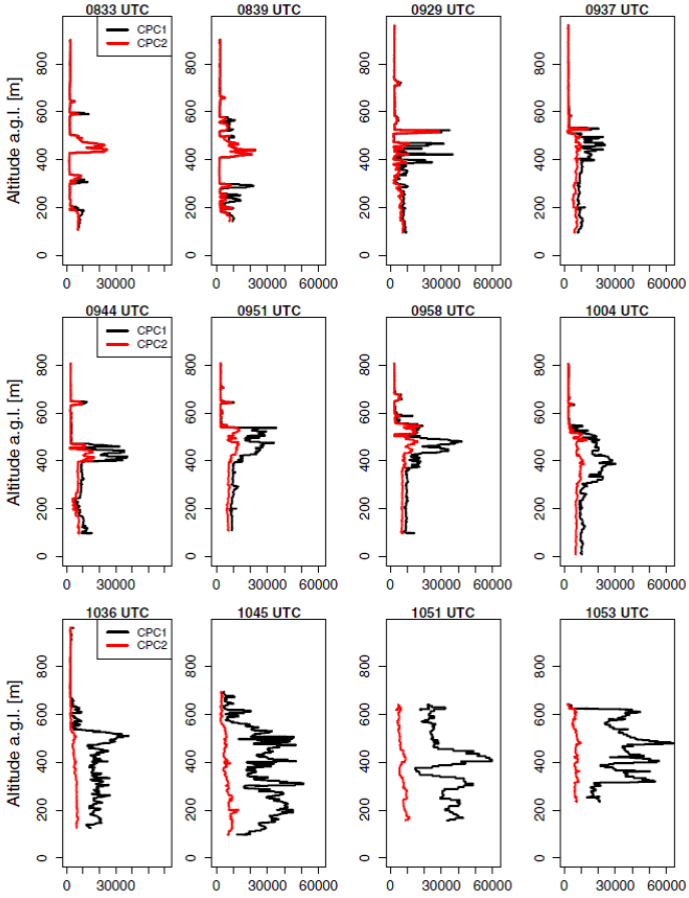

Figure 5.33: Vertical profiles of number concentrations observed between 08:33 and 10:53 UTC. The difference between CPC1 and CPC2 indicates the number concentrations of freshly formed particles in the size range from 5 to 10 nm. The NPF event is initiated at around 400 to 500 m altitude and then spreads downwards. Figure from Platis et al. (2015).

https://doi.org/10.24355/dbbs.084-201906170934-0

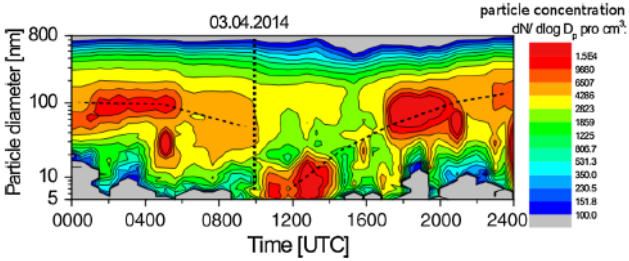

Figure 5.34: Time series of the aerosol size distribution measured with TSMPS on 3 April 2014. Enhanced concentrations of freshly formed particles were recorded simultaneously to the ALADINA observations of particles mixed downwards. The vertical black line indicates the time when the rest of the inversion was broken up by convective mixing. The dashed lines show the evolution of the maximum aerosol concentrations, indicating a growing process after the NPF event. Figure from Platis et al. (2015).

https://doi.org/10.24355/dbbs.084-201906170934-0

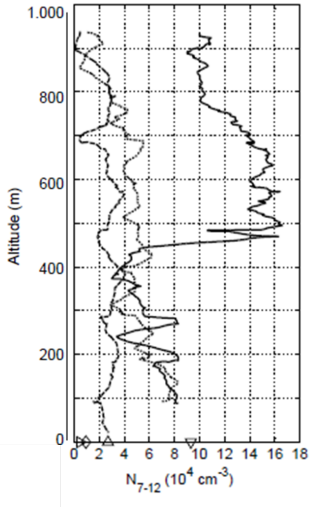

Figure 5.35: Vertical profiles of freshly formed particles with a diameter of 7-12 nm on 21 June 2015. The ALADINA observations were obtained at 08:13 UTC (solid line), 08:20 UTC (dotted line) and 08:26 UTC (dashed line), and from ground-based TSMPS data (triangles). Figure from Altstädter et al. (2018a).

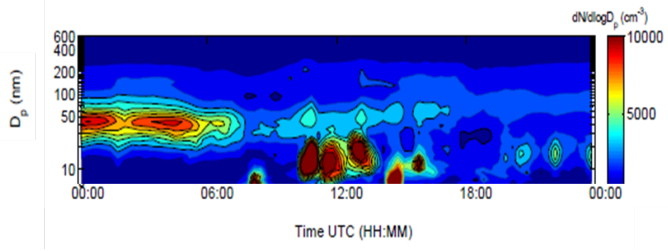

Figure 5.36: Time series of the aerosol size distribution measured with TSMPS on 21 June 2015. Enhanced concentrations of freshly formed particles were recorded intermittantly. Figure from Altstädter et al. (2018a).

https://doi.org/10.24355/dbbs.084-201906170934-0

6 Outlook: Future techniques for airborne meteorological research

In Chapter 5, several case studies covering current meteorological research projects have been presented. However, limitations from the point of view of technology and operation have to be overcome in the future to achieve substantial progress in the field of airborne meteorology.
In the bibliography, the publications providing the basis for the habilitation treatise are indicated in bold letters.

6.1 Potential of meteorological research with unmanned aerial systems

6.1.1 Intelligent UAS

With increasing experience in UAS handling, more sophisticated and reliable UAS techniques, and further development of miniaturized sensors, a strong impact of UAS based research can be expected. Smart systems are being developed, with the capabilities to fly not only automatically with an autopilot system, but autonomously, taking onboard decisions like collision avoidance. Operational meteorological survey flights are close to reality in remote areas like the polar regions (e.g., Cassano et al., 2016). This poses new challenges for the safe integration into the airspace.

6.1.2 UAS payload modifications

Different payloads can be installed for specific applications, with a rapidly growing spectrum at the transition from research to commercial applications. This opens new possibilities, like in the field of emission surveillance (Villa et al., 2017). Also for ALADINA, the range of applications is broadening. Measurements with an aethalometer have been used to study the small-scale and short-time vertical and horizontal variability of black carbon in Benin, West Africa (Altstädter et al., 2018b), a region with strong increase of anthropogenic aerosol which may contribute to local modifications of globally changing climate, and particularly to the monsoon circulation (Knippertz et al., 2015). Versatile UAS like ALADINA allow modifications depending on the conditions expected during specific operations. In 2017, the system described in Sect. 2.4 was again substantially modified for a measurement campaign in Ny-Ålesund, Svalbard. Because of the cold temperature of around -20° C expected on average in April, the payload bay is insulated passively and heated actively with heating foils. For more flexibility during field trips, it is now possible to choose between external power supply and battery power. To reduce the time between landing and standstill on the smooth runway of the airport, brakes were implemented to

https://doi.org/10.24355/dbbs.084-201906170934-0

the landing gear.

6.1.3 UAS for replacing other techniques

Meteorological UAS have the potential to contribute to and partly replace routine measurements like radio soundings, at least up to a certain altitude. Comparisons of radiosonde and UAS profiles in the ABL have shown good agreement of the data under a wide range of conditions, proving the reliability of the miniaturised sensors and the flight trajectories. Typically, the UAS reach a much higher spatial resolution. Two examples are shown in Fig. 6.1. Different systems for measuring the relative humidity and potential temperature were used almost simultaneously at the same places, in this case the meteorological observatory of the German Meteorological Service in Lindenberg near Berlin (Martin et al., 2011), and above sea ice in the Weddell Sea, Antactic (Jonassen et al., 2015). First ideas to combine a balloon borne payload for ascent with an autopilot controlled return glider for descent have been demonstrated by Kräuchi and Philipona (2016). In the near future they will play a key role in special research activities, like local studies of ABL phenomena. UAS provide the advantage of a controlled trajectory, enabling the investigation of interesting phenomena for research and weather forecast applications, independent of the mean wind speed and direction. However, limitations imposed by high wind speed and poor visibililty for takeoff and landing, as well as for the flight, have to be overcome.

6.1.4 New methods for measuring meteorological parameters

A lot of research remains to do for further qualification of UAS as reliable measurement platforms. Still an open question is the high-resolution determination of the 3D wind vector from multicopter systems. In principle, it should be possible to use the regulator and autopilot commands stabilizing the system against wind impact. This method has been applied to estimate the mean wind speed and wind direction (Brosy et al., 2017, Palomaki et al., 2017), but not yet for the complete wind vector, which is limited by the accuracy of inertial navigation system (INS) derived angles. Further, the interaction of platform and measurement payload should be critically evaluated. On the one hand, positive effects and additional tools can arise from a deep knowledge of the platform and its behaviour in the atmosphere. As an example, it is possible to retrieve the vertical wind speed component with high accuracy from measurements with glider aeroplanes (Pätzold, 2017). On the other hand, modifications of the atmosphere performed by the carrier platform can interfere with the measurement signal.

Fig. 6.2 shows raw data profiles of temperature (left) and relative humidity (right) obtained with the quadrocopter ALICE during a mission onboard of Polarstern. For the ascent, the temperature fluctuations are much less pronounced than during the descent. In this case, the disturbance of the rotor blades can be seen in the data.

6.1.5 Legal aspects

Legal aspects of UAS operation are an important topic, which can accelerate or prevent the massive routine use of UAS in the future. With an increasing number of UAS applica-

https://doi.org/10.24355/dbbs.084-201906170934-0

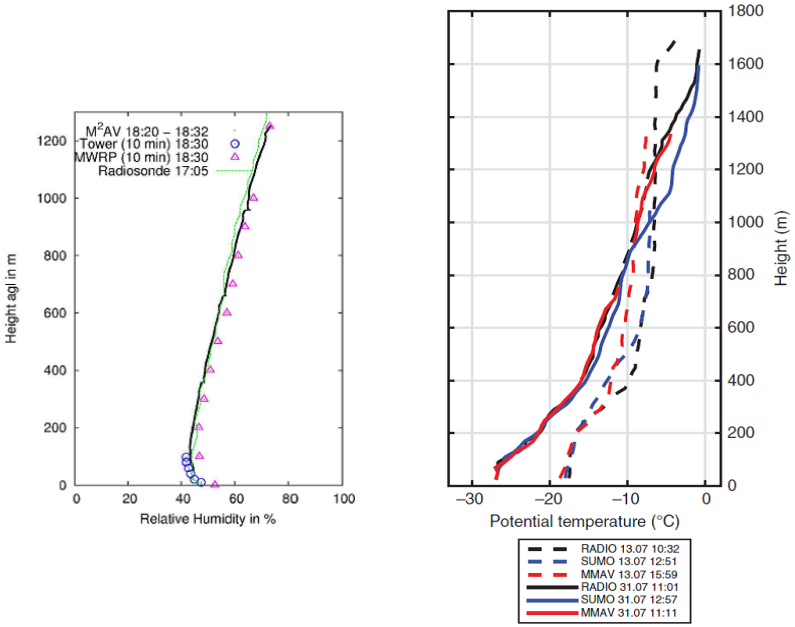

Figure 6.1: Atmospheric profiles of (a) relative humidity [%] (Figure from Martin et al., 2011) and (b) potential temperature [°C] (Figure from Jonassen et al., 2015) obtained with radiosonde, UAS and other instrumentation. The relative humidity was recorded on 21 July 2009 at the observatory of the German Meteorological Service in Lindenberg with the M^2AV, a radiosonde, a 100 m tower and a micro wave radio profiler (MWRP). The potential temperature profiles were recorded on 13 and 31 July 2013 above sea ice in the Weddell Sea, Antarctic, with the M^2AV, the UAS SUMO and radiosounding.

https://doi.org/10.24355/dbbs.084-201906170934-0

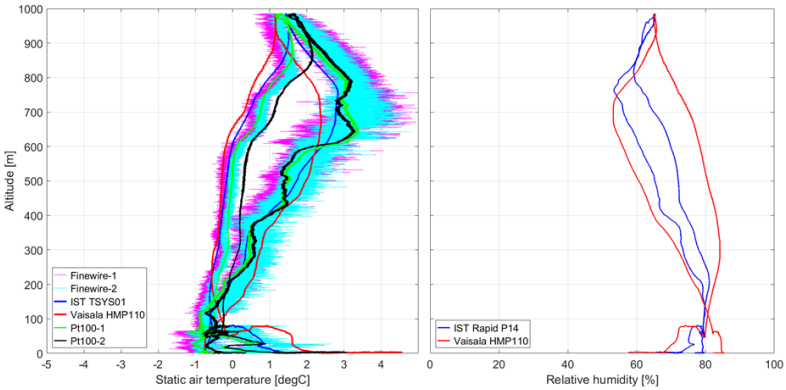

Figure 6.2: Raw data profiles of temperature and relative humidity obtained with the quadrocopter ALICE. The fine wire temperature sensors exhibit different turbulence properties during ascent and descent, as they experience the disturbance of the atmosphere by the rotor blades during descent.

tions by private persons, companies, authorities, emergency forces and research institutes, regulations are required to guarantee safety in the airspace and on ground, and protect personal rights. Generally, the harmonization of the very different regulations for UAS operation in Europe is planned by the EASA (European Aviation Safety Agency). The upper limit of 25 kg maximum take-off weight without the need of airworthiness certification is very likely to remain in the near future. It is planned to register and identify each UAS for obtaining a flight permission. There are currently two controversal tendencies of evolution:

On the one hand, more and stricter criteria need to be met to allow UAS operations. Visual surveillance by a ground-based observer is currently required by legislation in many countries with dense population (e.g. Norway, USA, France), with few exceptions e.g. in the high Arctic. Also in the near future, flights under the control of a safety pilot will be mandatory, for both uncontrolled air space and restricted areas. The procedures to obtain a flight permission in Germany until April 2017 have been described in Sect. 2.3.3. Even more documentation is required for operation of UAS in the size and weight class of ALADINA in some other countried. E.g. in Norway the regulations discriminate between operations in the categories *Visual Line Of Sight* (VLOS) below 400 ft, *Extended Visual Line of Sight* (EVLOS) above 400 ft and *Beyond Line Of Sight* (BLOS). The typical altitude of operations for ALADINA up to an altitude of 1000 m is classified as BLOS. Further, the weight class of ALADINA falls into the category Remote Operations 2 (RO2) and requires a permission from the Civil Aviation Authority (CAA). To obtain this, specific documents have to be provided: an operation manual with information about the system, radio frequencies, safety features, maintenance routines, training, checklists, risk analysis, naming responsib-

https://doi.org/10.24355/dbbs.084-201906170934-0

ilities as operating manager, technical manager and quality control manager, an insurance certificate, pilot's proficiency exam with questions about e.g. UAS technical terms, technical, operational and legal aspects, air space regulations, meteorology and physiology.
On the other hand, since April 2017, there have been fundamental changes in the German legislation. According to the Luftverordnung LuftVO§21, it is possible for public authorities, including universities, to fly beyond line of sight without the permission of the federal state aviation authorities. Also the obligation to pass an official written pilot's exam is explicitly not required for staff of these authorities. It is now requested to coordinate the planned flights with air traffic control to issue a NOTAM, and to obtain the permission of the nature protection agency, if flights are planned in a protection area. For other applications, a risk assessment is necessary to determine if it is possible to perform UAS operations. These new regulations are currently being established, and documents should be prepared several months in advance of the planned mission.

6.2 Dynamic calibration of fast H_2O sensors for research aircraft

As humidity plays a key role in atmospheric research, and latent heat fluxes require the use of a sensor with short response time, the development of a dynamic calibration procedure is mandatory. In Sect. 5.4 it was shown that even for a good agreement of absolute humidity values, sensors can have a different dynamic behaviour, which has an impact on the spectra. The qualification of fast humidity sensors should include a setup to determine the response to a sharp change in humidity (important for transfer functions that can be represented by a first-order delay element, PT1), as well as to sinusoidal changes in the frequency range of interest for airborne meteorology (around 0.1 to 20 Hz). The challenge is to design a calibration system that can be controlled with an accuracy higher than the accuracy of the humidity sensors. The aim is to be able to control changes to the system with an accuracy of around 1 % for relative humidity, 1 % for absolute humidity, and 0.15 K for the dew point temperature. One possibility is to realize the calibration system as an adiabatic process by e.g. using a cylinder as control volume with the sensors integrated inside, which is expanded and compressed quickly by actuating a piston. The position of the piston has to be measured precisely, as the accuracy of the volume determines the accuracy of the temperature by the ideal gas equation. Calibration at low temperatures can be realized by first expanding the volume and then stimulating the sinusoidal oscillations, or by putting the whole setup into a climate chamber with lower temperatures. However, the relative humidity should not exceed 95 % to avoid condensing conditions. A disadvantage of the setup is that the air speed is probably not high enough for the dew point mirror to obtain the full measurement speed (Fahey et al., 2014).
The PTB Braunschweig recently developed a new, highly specialized metrological hygrometer concept (Buchholz et al., 2017) with the research center of Jülich for water vapour measurements on the HALO research aircraft (Krautstrunk and Giez, 2012), called Hygrometer for Atmospheric Investigations (HAI). This complex multi-channel system offers fast, highly precise, absolute, reliable, redundant measurements based on a calibration-free TDLAS system and corresponding data processing procedure, which was metrologically validated on the national primary humidity standards. However, HAI's mechanical dimensions and weight, and its specific adaptation to HALO, precludes its usage on smaller

https://doi.org/10.24355/dbbs.084-201906170934-0

aircraft such as the IBUF (Sect. 2.1) or the Polar 5/6 of the Alfred Wegener Institute, low and slow flying aircraft that are much more suited for the specific needs of the atmospheric flux community than HALO. As it is of special importance to quantify turbulent fluxes of latent heat with high accuracy and defined uncertainties, and no fully suitable instrument, neither commercial nor academic, is currently available for such measurements, a new open-path instrument should be developed with a special design focus on high-frequency (> 200 Hz raw data frequency) measurements of fine atmospheric water vapour structures. Such an instrument should be linked to the international metrological water vapour scale via a direct validation at a primary metrological humidity standard.

6.3 Meteorological data for future mobility and energy supply

A profound understanding of atmospheric processes combined with a large availability of high quality meteorological data leads to impoved weather forecast and nowcast models. Specific products can be processed with high benefit for modern society in various fields. Besides personal advantages in daily life by providing a better and everywhere available weather forecast, these products can be used to enhance future mobility and energy supply. Especially airborne traffic has increased in the past decades and will very likely continue to increase in the next decades (Eurocontrol, 2013). More than other transport vehicles like rail, ship and road, aviation is directly dependent on weather. Fog, thunderstorms and icing conditions cause delays and even cancelled flights. Further, atmospheric phenomena like wakes behind aircraft limit the capacity of airports (Holzäpfel et al., 2012). At some airports with a frequent occurrence of strong LLJs, such forecasts are part of the weather analysis, and warnings are issued to pilots to improve safety during approach and landing (Kaplan et al., 2000). In the future, this information could be provided even in real time to the cockpit for pilots in situations of high work load (e.g. approach to wind parks, rescue missions in mountaineous terrain).

As described in Sect. 6.1, in the future, the approved and reliable meteorological data base of radiosounding will be complemented by more flexible UAS soundings, which allow to prescribe the trajectory, and perform measurements along particular flight trajectories which are of scientific or forecasting interest, e.g. to probe the air in an approaching frontal system. This flexible probing may enhance the weather forecasting significantly, and enable better prediction possibilities for aviation.

With the power supply depending more and more on renewable energy, the weather plays a more important role to control and plan the complex network structure with flexible feed-in from various sources. In case of accurate forecasts of the nocturnal LLJ, the power output of wind parks can be estimated more realistically. For some regions with a pronounced and regular LLJ, this forecast is already available (Storm et al., 2009). With increasing power produced by offshore wind parks, the security and stability of the power supply system crucially depend on the precise forecast of near-future power output. This requires reliable data and validation of simulations. Especially for the planned construction of superclusters covering the North Sea, the impact and interactions of the whole clusters need to be quantified. For the rare cases of wind speed exceeding $25\,\mathrm{m\,s^{-1}}$, each wind turbine is currently stopped to avoid damage. However, this sudden drop in power output can be detrimental for net stability, and engineering solutions have to be developed to

https://doi.org/10.24355/dbbs.084-201906170934-0

avoid these situations, based on the knowledge of the wind field and dynamics of passing frontal systems.

6.4 Future choice of appropriate airborne platforms

For the multiple aims of airborne meteorological applications, various platforms equipped with different sensors and technology are available, and can be rented or used upon the decision of a scientific advisory board (e.g. EUFAR). For realistically planning future airborne meteorological projects, a tool addressing different aspects that are important for the measurements from a logistical, operational, financial and scientific point of view would be helpful. For example, a future application is the measurement of trace gases in remote regions. For limited space on a ship, a vertical takeoff and landing (VTOL) system may be a good option that enables takeoff and landing like a multicopter on a very confined area, but allows straight and level flight like fixed-wing aircraft, and therefore the 3D wind speed calculation. The envelope of weight and balance is more constraint compared to the other systems.
A closer collaboration of research institutes and operators of the manifold airborne platforms could be stimulated by making transparent the conditions of use and timelines of the platforms that are in use. UAS would benefit from an easily exchangeable modular system and flexible data acquisition systems to adapt additional sensors. For example, for ALADINA it should be possible to remove the whole front system with the aerosol payload and substitute it with e.g. sensors for measuring greenhouse gases or aerial photographic mapping. At IFF, the future perspective is to operate a variety of platforms as presented in Chapt. 2 with compatible data acquisition, data format, interfaces, and finally software for data processing. Out of these versatile systems, the appropriate platform can be chosen for own investigations. Further, the diversity of systems easy to modify can be offered to partners and external scientists as test bed to qualify new sensors. The future vision is to set up an online tool for facilitating access to airborne platforms of different size and capabilities, including unmanned systems. As a start, it could be coordinated for the area of Braunschweig by the Aeronautics Research Centre Niedersachsen (NFL).

https://doi.org/10.24355/dbbs.084-201906170934-0

Bibliography

Abdou, K., Parker, D.J., Brooks, B., Kalthoff, N., and Lebel, T.: The diurnal cycle of lower boundary-layer wind in the West African monsoon, Q.J.R. Meteorol. Soc., 136 (s1), 66-76, 2010.

Acevedo, O., and Fitzjarrald, D.R.: The Early Evening Surface-Layer Transition: Temporal and Spatial Variability, J. Atmos. Sci., 58, 2650-2667, 2001.

Altstädter, B., Platis, A., Wehner, B., Scholtz, A., Wildmann, N., Hermann, M., Käthner, R., Baars, H., Bange, J., and Lampert, A.: ALADINA – an unmanned research aircraft for observing vertical and horizontal distributions of ultrafine particles within the atmospheric boundary layer, Atmos. Meas. Tech., 8, 1627–1639, 2015.

Altstädter, B., Platis, A., Jähn, M., Baars, H., Lückerath, J., Held, A., Lampert, A., Bange, J., Hermann, M., and Wehner, B.: Airborne observations of newly formed boundary layer aerosol particles under cloudy conditions, submitted to Atmos. Chem. Phys., 2018.

Altstädter, B., Ebus, F., Deetz, K., Vogel, B., Babić, K., Dione, C., Pacifico, F., Jambert, C., Bärfuss, K., Pätzold, F., Lampert, A., Adler, B., Kalthoff, N., and Lohou, F.: Vertical inhomogeneity of black carbon measured with the UAS ALADINA in the boundary layer over Benin during DACCIWA, in preparation for Atmos. Chem. Phys., 2018.

Angevine, W.M., Baltink, H.K., and Bosveld, F.C.: Observations Of The Morning Transition Of The Convective Boundary Layer, Bound.-Layer Meteorol., 101, 2, 209-227, 2001.

Baas P., Bosveld F.C., Klein Baltink H., Holtslag A.A.M.: A Climatology of Nocturnal Low-Level Jets at Cabauw. J. Appl. Meteor. Climatol., 48, 1627-1642, DOI: 10.1175/2009JAMC1965.1, 2009.

Baas, P., Bosveld, F.C., Lenderink, G., van Meijgaard, E., and Holtslag, A.A.M.: How to design single-column model experiments for comparison with observed nocturnal low-level jets, Q. J. R. Meteorol. Soc., 136, 671-684. DOI: 10.1002/qj.592, 2010.

Baas, P., van de Wiel, B.J.H., van der Linden, S.J.A., and Bosveld, F.C.: From Near-Neutral to Strongly Stratified: Adequately Modelling the Clear-Sky Nocturnal Boundary Layer at Cabauw, Bound.-Layer Meteorol., 166, 217-238, 2018.

Bärfuss, K., Pätzold, F., Altstädter, B., Kathe, E., Nowak, S., Bretschneider, L., Bestmann, U., and Lampert, A.: New Setup of the UAS ALADINA

https://doi.org/10.24355/dbbs.084-201906170934-0

for Measuring Boundary Layer Properties, Atmospheric Particles and Solar Radiation, Atmosphere, 9(1), 28; doi:10.3390/atmos9010028, 2018.

Bange, J., and Roth, R.: Helicopter-borne flux measurements in the nocturnal boundary layer over land - a case study, Bound.-Layer Meteorol., 92, 295-325, 1999.

Bange, J., Beyrich, F., and Engelbart, D.A.M.: Airborne measurements of turbulent fluxes during LITFASS-98: Comparison with ground measurements and remote sensing in a case study, Theor. Appl. Climatol., 73, 35-51, 2002.

Bange, J., Zittel, P., Spiess, T., Uhlenbrock, J., and Beyrich, F.: A new method for the determination of area-averaged turbulent surface fluxes from low-level flights using inverse models, Bound.-Layer Meteorol., 119, 527-561, 2006.

Banta, R.M., Newsome, R.K., Lundquist, J.K., Pichugina, Y.L., Coulter, R.L., and Mahrt, L.: Nocturnal low-level jet characteristics over Kansas during CASES-99, Bound.-Layer Meteorol., 105, 221-252, 2002.

Banta, R.M., Pichugina, Y.L., and Newsom, R.K.: Relationship between low-level jet properties and turbulence kinetic energy in the nocturnal stable boundary layer. J. Atmos. Sci., 60, 2549-2555, 2003.

Banta, R.M., Pichugina, Y.L„ and Brewer, W.A.: Turbulent velocity-variance profiles in the stable boundary layer generated by a nocturnal low-level jet. J. Atmos. Sci., 63, 2700-2719, 2006.

Banta, R.M.: Stable-boundary-layer regimes from the perspective of the low-level jet. Acta Geophysica, 56, 1, 58-87, DOI: 10.2478/s11600-007-0049-8, 2008.

Barbaro, E., Vilà-Guerau de Arellano, J., Ouwersloot, H.G., Schröter, J.S., Donovan, D.P., and Krol, M.C.: Aerosols in the convective boundary layer: Shortwave radiation effects on the coupled land-atmosphere system, J. Geophys. Res. Atmos., 119, 5845–5863, doi:10.1002/2013JD021237, 2014.

Barthelmie, R., Frandsen, S.T., Rethore, P.E., Jensen, L.: Analysis of atmospheric impacts on the development of wind turbine wakes at the Nysted wind farm, Proc. Eur. Offshore Wind Conf., Berlin 4.-6.12.2007, 2007.

Barthelmie, R.J., Hansen, K., Frandsen, S.T., Rathmann, O., Schepers, J.G., Schlez, W., Philips, J., Rados, K., Zervos, A., Politis, E.S., and Chaviaropoulos, P.K.: Modelling and Measuring Flow and Wind Turbine Wakes in Large Wind Farms Offshore, Wind Energy, 12, 431-444, 2009.

Bates, T.S., Quinn, P.K., Johnson, J.E., Corless, A., Brechtel, F.J., Stalin, S.E., Meinig, C., and Burkhart, J.F.: Measurements of atmospheric aerosol vertical distributions above Svalbard, Norway, using unmanned aerial systems (UAS), Atmos. Meas. Tech., 6, 2115-2120, 2013.

Baidya Roy, S., and Traiteur, J.J.: Impacts of wind farms on surface air temperatures, Proc. Natl. Acad. Sci. 107, 17899–17904, 2010.

https://doi.org/10.24355/dbbs.084-201906170934-0

Beare, R.J., Edwards, J.M., and Lapworth, A.J.: Simulation of the observed evening transition and nocturnal boundary layers: Large-eddy simulation, Quart. J. Roy. Meteor. Soc., 132, 81–99, 2006.

Beaton, S.P., and Spowart, M.: UV Absorption Hygrometer for Fast-Response Airborne Water Vapour Measurements, J. Atmos. Ocean. Technolog., 29, 1295-1303, 2012.

Bigg, E.: A mechanism for the formation of new particles in the atmosphere, Atmos. Res., 43, 2, 129–137, 1997.

Birmili, W., and Wiedensohler, A.: New particle formation in the continental boundary layer: Meteorological and gas phase parameter influence, Geophys. Res. Lett., 27, 3325–3328, 2000.

Birmili, W., Wiedensohler, A., Heintzenberg, J., and Lehmann, K.: Atmospheric particle number size distribution in central Europe: Statistical relations to air masses and meteorology, J. Geophys. Res., 106, 32005–32018, 2001.

Blackadar, A.K.: Boundary layer wind maxima and their significance for the growth of nocturnal inversions. Bull. Am. Met. Soc., 38, 283-290, 1957.

de Boer, G., Palo, S., Argrow, B., LoDolce, G., Mack, J., Gao, R-S., Telg, H., Trussel, C., Fromm, J., Long, C.N., Bland, G., Maslanik, J., Schmid, B., and Hock, T.: The Pilatus unmanned aircraft system for lower atmospheric research, Atmos. Meas. Tech., 9, 1845-1857, 2016.

Boiffier, J.-L., 1998: The Dynamics of Flight: The Equations, Wiley, 353 pp., 1998.

Boike, J., Wille, C., and Abnizova, A.: Climatology and summer energy and water balance of polygonal tundra in the Lena River Delta, Siberia, J. Geophys. Res.: Biogeosciences, 113, G03025,doi:10.1029/2007JG000540, 15pp., 2008.

Bonin, T., Chilson, P., Zielke, B., and Fedorovich, E.: Observations of the early evening boundary-layer transition using a small unmanned aerial system, Bound.-Layer Meteor., 146, 119–132,2013.

Bonner, W. D.: Climatology of the low level jet, Mon. Wea. Rev., 96, 833-850, 1968.

Boy M., Rannik, Ü., Lehtinen K.E.J., Tarvainen V., Hakola H., and Kulmala M.: Nucleation events in the continental boundary layer: Long-term statistical analyses of aerosol relevant characteristics, J. Geophys. Res., 108, D21, 4667, doi:10.1029/2003JD003838, 2003.

Boy M., Hellmuth O., Korhonen H., Nilsson E.D., ReVelle D., Turnipseed A., Arnold F., and Kulmala M.: MALTE – model to predict new aerosol formation in the lower troposphere, Atmos. Chem. Phys., 6, 4499-4517, 2006.

Brosy, C., Krampf, K., Zeeman, M., Wolf, B., Junkermann, W., Schäfer, K., Emeis, S., and Kunstmann, H.: Simultaneous multicopter-based air sampling and sensing of meteorological variables, Atmos. Meas. Tech., 10, 2773–2784, 2017.

https://doi.org/10.24355/dbbs.084-201906170934-0

Brümmer, B., Kirchgäßner, A., Müller, G., Schröder, D., Launiainen, J., and Vihma, T.: The BALTIMOS (BALTEX Integrated Model System) field experiments: A comprehensive atmospheric boundary layer data set for model validation over the open and ice-covered Baltic Sea, Boreal Environ. Res., 7, 371-378, 2002.

Buchholz, B., Kühnreich, B., Smit, H.G.J., and Ebert, V.: Validation of an extractive, airborne, compact TDL spectrometer for atmospheric humidity sensing by blind intercomparison, Appl. Phys. B, 110, 249-262, 2013.

Buchholz, B., Böse, N., and Ebert, V.: Absolute validation of a diode laser hygrometer via intercomparison with the German national primary water vapor standard, Appl. Phys. B, 116, 4, 883-899, 2014.

Buchholz, B.: Entwicklung, Primärvalidierung und Feldeinsatz neuartiger, kalibrierungsfreier Laser-Hygrometer für Forschungsflugzeuge, Dissertation TU Darmstadt, 265 pp., http://tuprints.ulb.tu-darmstadt.de/4020, 2014.

Buchholz, B., Afchine, A., Klein, A., Schiller, C. and Krämer, M.: HAI , a new airborne, absolute, twin dual-channel, multi-phase TDLAS-hygrometer: background, design, setup, and first flight data, Atmos. Meas. Tech., 5194, http://dx.doi.org/10.5194/amt-10-35-2017, 2017.

Buck, A. L.: Development of an improved Lyman-alpha hygrometer, Atmos. Technol., 2, 213-240, 1973.

Buck, A. L.: The variable-path Lyman-alpha hygrometer and its operating characteristics, B. Am. Meteorol. Soc., 57, 1113-1118, 1976.

Burton, T., Sharpe, D., Jenkins, N., and Bossanyi, E.: Wind energy handbook, Second Edition, Wiley: New-York, 780 pp., 2011.

Busen, R., and Buck, A.L.: A High-Performance Hygrometer for Aircraft Use: Description, Installation, and Flight Data, J. Atmos. Ocean. Technolog., 12, 73-84, 1995.

Busse, J., and Knupp, K.: Observed Characteristics of the Afternoon-Evening Boundary Layer Transition Based on Sodar and Surface Data, J. App. Meteorol. Climatol., 51, 571-582, 2012.

Canut, G., Couvreux, M., Lothon, M., Legain, D., Piguet, B., Lampert, A., Maurel, W., and Moulin, E.: Turbulence fluxes and variances measured with a sonic anemometer mounted on a tethered balloon, Atmos. Meas. Tech., 9, 4375-4386, 2016.

Cassano, J.J., Seefeldt, M.W., Palo, S., Knuth, S.L., Bradley, A.C., Herrman, P.D., Kernebone, P.A., and Logan, N.J.: Observations of the atmosphere and surface state over Terra Nova Bay, Antarctica, using unmanned aerial systems, Earth Syst. Sci. Data, 8, 115–126, 2016.

Caughey, S.J., Wyngaard, J.C., and Kaimal, J.C.: Turbulence in the evolving stable boundary layer. J. Atmos. Sci., 36, 1041–1052, 1979.

https://doi.org/10.24355/dbbs.084-201906170934-0

Chahine, M.T.: The hydrological cycle and its influence on climate, Nature, 359, 373-380, 1992.

Christiansen, M.B., and Hasager, C.B.: Wake effects of large offshore wind farms identified from satellite SAR, Remote Sens. Environ., 98, 251–268, doi:10.1016/j.rse.2005.07.009, 2005.

Coalition Agreement, 2013, *http* : *//www.fdp.de/files/*565/2009 − 203*_en_Koalitionsvertrag_*2009*.pdf*, accessed on 31 August 2016.

Coelingh, J.P., van Wijk, A.J.M., and Holtslag, A.A.M.: Analysis of wind speed observations over the North Sea, J. Wind. Eng. Industr. Aerodyn., 61, 51-69, 1996.

Conangla, L., and J. Cuxart, J.: On the turbulence in the upper part of the low-level jet: An experimental and numerical study. Bound.-Lay. Meteorol., 118, 379-400, 2006.

Corsmeier, U., Hankers, R., and Wieser, A.: Airborne turbulence measurements in the lower troposphere onboard the research aircraft Dornier 128-6, D-IBUF, Meteorol. Z., 10, 315-329, 2001.

Corsmeier, U., Kalthoff, N., Vogel, B., Hammer, M.-U., Fiedler, F., Kottmeier, C., Volz-Thomas, A., Konrad, S., Glaser, K., Neininger, B., Lehning, M., Jaeschke, W., Memmesheimer, M., Rapenglück, B., and Jakobi, G.: Ozone and PAN Formation Inside and Outside of the Berlin Plume – Process Analysis and Numerical Process Simulation, J. Atmos. Chem., 42, 289-321, 2002.

Curry, J.A., Maslanik, J., Holland, G., and Pinto, J.: Applications of Aerosondes in the Arctic, Bull. Am. Meteor. Soc., doi:10.1175/BAMS-85-12-1855, 1855-1861, 2004.

Cuxart, J., and Jiménez, M.A.: Mixing Processes in a Nocturnal Low-Level Jet: An LES Study. J. Atmos. Sci, 64, 1666-1679, 2007.

Cuxart, J., Cunillera, J., Jiménez, M. A., Martínez, D., Molinos, F., Palau, J.L.: Study of mesobeta basin flows by remote sensing, Boundary-Layer Meteorology, 143, 143-158, 2012.

Cuxart, J. Wrenger, B., Martínez-Villagrasa, D., Reuder, J., Jonassen, M.O., Jiménez, M.A., Lothon, M., Lohou, F., Hartogensis, O., Dünnermann, J., Conangla, L. and Garai, A.: Estimation of the advection effects induced by surface heterogeneities in the surface energy budget, Atmos. Chem. Phys., 16, 9489–9504, 2016.

Darbieu, C., Lohou, F., Lothon, M., Vilà-Guerau de Arellano, J., Couvreux, F., Durand, P., Pino, D., Patton, E. G., Nilsson, E., Blay-Carreras, E., and Gioli, B.: Turbulence vertical structure of the boundary layer during the afternoon transition, Atmos. Chem. Phys., 15, 10071-10086, doi:10.5194/acp-15-10071-2015, 2015.

Davies, P.A.: Development and mechanisms of the nocturnal jet, Meteorol. Appl., 239-246, 2000.

https://doi.org/10.24355/dbbs.084-201906170934-0

Dias, N.L., Gonçalves, J.E., Freire, L.S., Hasegawa, T., and Malheiros, A.L.: Obtaining Potential Virtual Temperature Profiles, Entrainment Fluxes, and Spectra from Mini Unmanned Aerial Vehicles, Boundary-Lay. Meteorol., doi 10.1007/s10546-011-9693-2, 19pp., 2012.

Dörenkämper, M., Optis, M., Monahan, A., and Steinfeld, G.: On the offshore advection of boundary-layer structures and the influence on offshore wind conditions, Bound.-Layer Meteorol., 155, 459–482, 2015.

Doyle, J.D., and Warner, T.T.: A Three-Dimensional Numerical Investigation of a Carolina Coastal Low-Level Jet during GALE IOP 2, Mon. Weather Rev., 121, 1030-1047, 1993.

Drobinski, P. Ducrocq, V., Albert, P., et al.: HyMeX, a 10 year multidisciplinary program on the Mediterranean water cycle, Bull. Amer. Meteor. Soc., early online view, DOI: 10.1175/BAMS-D-12-00242.1, 2013.

Drüe, C., and Heinemann, G.: Characteristics of intermittent turbulence in the upper stable boundary layer over Greenland, Bound.-Layer Meteorol., 124, 3, 361-381, 2007.

Ducrocq, V., Braud, I., Davolio, S., et al.: HyMeX-SOP1, the field campaign dedicated to heavy precipitation and flash flooding in the northwestern Mediterranean, Bull. Amer. Meteor. Soc., early online view, DOI: 10.1175/ BAMS-D-12-00244.1, 2013.

Eecen, P.J., Wagenaar, J.W., Stefanatos, N., Pedersen, T.F., Wagner, R., and Hansen, K.S., Final report UPWIND 2011, 1A2 Metrology, 2011.

El-Asha, S., Zhan, L., and Lungo, G.V.: Quantification of power losses due to wind turbine wake interactions through SCADA meteorological and wind LiDAR data, Wind Energy, 20, 1823-1839, 2017.

Elston, J.S., Roadman, J., Stachura, M., Argrow, B., Houston, A., and Frew, E.W. 2011: The tempest unmanned aircraft system for in situ observations of tornadic supercells: Design and VORTEX2 flight results, J. Field Rob., 28, 461–483,2011.

Elston, J., Argrow,B., Stachura, M., Weibel, D., Lawrence, D., and Pope, D.: Overview of Small Fixed-Wing Unmanned Aircraft for Meteorological Sampling, J. Atmos. Oceanic Technol., 32, 97–115, doi: 10.1175/JTECH-D-13-00236.1, 2015.

Emeis, S.: Vertical variation of frequency distributions of wind speed in and above the surface layer observed by sodar. Meteorologische Zeitschrift, 10, 2, 141-149, 2001.

Emeis, S.: Vertical wind profiles over an urban area, Meteorologische Zeitschrift, 13, 5, 353-359, 2004.

Emeis, S., Harris, M., and Banta, R.M.: Boundary-layer anemometry by optical remote sensing for wind energy applications, Meteorologische Zeitschrift, 16, 4, 337-347, 2007.

Emeis, S.: A simple analytical wind park model considering atmospheric stability, Wind Energy, 13, 459–469, 2010.

Emeis, S.: Wind speed and shear associated with low-level jets over Northern Germany. Meterologische Zeitschrift, 23, 3, 295-304, DOI: 10.1127/0941-2948/2014/0551, 2014.

https://doi.org/10.24355/dbbs.084-201906170934-0

Emeis, S., Siedersleben, S., Lampert, A., Platis, A., Bange, J., Djath, B., Schulz-Stellenfleth, J., and Neumann, T.: Exploring the wakes of large offshore wind farms, Journal of Physics: Conference Series, IOP Publishing, 753, 092014, doi:10.1088/1742-6596/753/9/092014, 2016.

Etling, D.: Theoretische Meteorologie: Eine Einführung, Springer Berlin Heidelberg, doi:10.1007/978-3-662-10430-9, 354 pp., 2002.

Eurocontrol: Challenges of Growth 2013, Task 4: European Air Traffic in 2035, http://www.eurocontrol.int/sites/default/files/article/content/documents/official-documents/reports/201306-challenges-of-growth-2013-task-4.pdf, 64 pp., 2013, accessed on 8 November 2016.

Fahey, D. W., Gao, R.-S., Möhler, O., Saathoff, H., Schiller, C., Ebert, V., Krämer, M., Peter, T., Amarouche, N., Avallone, L. M., Bauer, R., Bozóki, Z., Christensen, L. E., Davis, S. M., Durry, G., Dyroff, C., Herman, R. L., Hunsmann, S., Khaykin, S. M., Mackrodt, P., Meyer, J., Smith, J. B., Spelten, N., Troy, R. F., Vömel, H., Wagner, S., and Wienhold, F. G.: The AquaVIT-1 intercomparison of atmospheric water vapor measurement techniques, Atmos. Meas. Tech., 7, 3177-3213, doi:10.5194/amt-7-3177-2014, 2014.

Fiedler, B., and Bukovsky, M.: The effect of a giant wind farm on precipitation in a regional climate model, Environ. Res. Lett. 6, 045101, 2011.

Fitch, A.C., Olson, J.B., Lundquist, J.K., Dudhia, J., Gupta, A.K., Michalakes, J., and Barstad, I.: Local and Mesoscale Impacts of Wind Farms as Parameterized in a Mesoscale NWP Model, Mon. Wea. Rev., 140(9), 3017–3038, doi:10.1175/MWR-D-11-00352.1, 2012.

Fitch, A.C., Lundquist, J.K., and Olson, J.B.: Mesoscale influences of wind farms throughout a diurnal cycle, Mon. Weather. Rev., 141, 2173–2198, 2013.

Fitzjarrald, D.R., and Lala, G.G.: Hudson Valley Fog Environments, J. Appl. Meteorol., 28, 1303-1328, 1989.

Foken, T.: Turbulenter Energieaustausch zwischen Atmosphäre und Unterlage, Berichte des deutschen Wetterdienstes, 180, 287 pp., 1990.

Foken, T., and Falke, H.: Technical Note: Calibration device for the krypton hygrometer KH20, Atmos. Meas. Tech., 5, 1861-1867, 2012.

Foreman, R., Cañadillas, B., Neumann, T., and Emeis, S.: Measurements of heat and humidity fluxes in the wake of offshore wind turbines, J. of Renewable and Sustainable Energy, 9, 053304, 2017.

Garreaud R.D., and Muñoz, R.C.: The Low-Level Jet off the West Coast of Subtropical South America: Structure and Variability, Monthly Weather Review, 133, 2246-2261, 2005.

Gasch, R., and Twele, J.: Windkraftanlagen: Grundlagen, Entwurf, Planung und Betrieb, Vieweg+Teubner Verlag, 10.1007/978-3-322-99446-2, pp. 588, 2005.

https://doi.org/10.24355/dbbs.084-201906170934-0

Grant, A. L. M.: An observational study of the evening transition boundary-layer. Quart. J. Roy. Meteor. Soc., 123, 657–677, 1997.

Groenemeijer, P., Barthlott, C., Behrendt, A., Corsmeier, U., Handwerker, J., Kohler, M., Kottmeier, C., Mahlke, H., Pal, S., Radlach, M., Trentmann, J., Wieser, A., and Wulfmeyer, V.: Observations of Kinematics and Thermodynamic Structure Surrounding a Convective Storm Cluster over a Low Mountain Range, Monthly Weather Review, 137, 585-602, 2009.

Gross, G.: Numerical simulation of future low-level jet characteristics, Meteorologische Zeitschrift, 21, 305-311, 2012.

Gultepe, I., and Starr, D.O'C.: Dynamical Structure and Turbulence in Cirrus Clouds: Aircraft Observations during FIRE, J. Atmos. Sci., 52, 23, 4159-4182, 1995.

Gutierrez, W., Araya, G., Kiliyanpilakkil, P., Ruiz-Columbie, A., Tutkun, M., and Castillo, L.: Structural impact assessment of low level jets over wind turbines, J. Renewable Energy, 8, 023308, 15 pp., 2016.

Haala, N., Cramer, M., Weimer, F., and Trittler, M.: Performance test on UAV-based photogrammetric data collection, Proceedings of the International Archives of the Photogrammetry, Remote Sensing and Spatial Information Sciences, Zurich, Switzerland, 14-16 September 2011, XXXVIII-1/C22, 7-12, 2011.

Hankers, R.: The Equipment of a Research Aircraft with Emphasis on Meteorological Experiments, Proceedings of the 20th Annual Symposium Society of Flight Test Engineers, 18-21 September 1989, Reno, Nevada, USA, 1989.

Hansen, K.S., Barthelmie, R.J., Jensen, L.E., and Sommer, A.: The impact of turbulence intensity and atmospheric stability on power deficits due to wind turbine wakes at Horns Rev wind farm, Wind Energy, 15, 183-196, 2012.

Heintzenberg, J., Wehner, B., and Birmili, W.: 'How to find bananas in the atmospheric aerosol': new approach for analyzing atmospheric nucleation and growth events, Tellus B, 59, 273–282, doi:10.1111/j.1600-0889.2007.00249.x,2007.

Hellmuth O.: Columnar modelling of nucleation burst evolution in the convective boundary layer – first results from a feasibility study, Part III: Preliminary results on physicochemical model performance using two "clean air mass" reference scenarios, Atmos. Chem. Phys., 6, 4231-4251, 2006.

Herman, R.L., Ray, E.A., Rosenlof, K.H., Bedka, K.M., Schwartz, M.J., Read, W.G., Troy, R.F., Chin, K., Christensen, L.E., Fu, D., Stachnik, R.A., Bui, T.P., Dean-Day, J.M.: Enhanced stratospheric water vapor over the summertime continental United States and the role of overshooting convection, Atmos. Chem. Phys., 17, 6113-6124, 2017.

Herrmann, H., Brüggemann, E., Franck, U., Gnauk, T., Löschau, G., Müller, G., Plewka, A., and Spindler, G.: A source study of PM in Saxony by Size-Segregated Characterisation, J. Atmos. Chem., 55, 2, 103-130, doi:10.1007/s10874-006-9029-7, 2006.

https://doi.org/10.24355/dbbs.084-201906170934-0

Hiller, R.V., Neininger, B., Brunner, D., Gerbig, C., Bretscher, D., Künzle, T., Buchmann, N., and Eugster, W.: Aircraft based CH4 flux estimates for validation of emissions from an agriculturally dominated area in Switzerland, J. Geophys. Res. Atmos., 119, 4874-4887, doi:10.1002/2013JD020918, 2014.

Hinüber, E.V., Knedlik, S., and Bestmann, U.: Low Weight COTS based Inertial Navigation Systems with EASA Certification Potential for UAVs, General Aviation and Military Aircraft, Proceedings of the 6th UAV World Conference at AIRTEC, Frankfurt/Main, Germany, 6–8 November, 2012.

Holland, G.J., McGeer, T., and Youngren, H.: Autonomous Aerosondes for economical atmospheric soundings anywhere on the globe, B. Am. Meteorol. Soc., 73, 1987–1998, 1992.

Holland, G.J., Webster, P.J., Curry, J.A., Tyrell, G., Gauntlett, D., Brett, G., Becker, J., Hoag, R., and Vaglienti, W.: The Aerosonde Robotic Aircraft: A New Paradigm for Environmental Observations, Bull. Am. Meteor. Soc., 82, 5, 889-901, 2001.

Holzäpfel, F., and Gerz, T.: Two-Dimensional Wake Vortex Physics in the Stably Stratified Atmosphere, Aerospace Science and Technology, 3, 5, 261–270, 1999.

Holzäpfel, F.: Probabilistic Two-Phase Wake Vortex Decay and Transport Model, Journal of Aircraft, 40,2, 323–331, 2003.

Holzäpfel, F., et al.: Aircraft Wake Vortex State-of-the-Art & Research Needs, Report on the WakeNet3-Europe Project European Coordination Action for Aircraft Wake Turbulence, 201 pp., 2012.

Illingworth, S., Allen, G., Percival, CC., Hollingsworth, P., Gallagher, M., Ricketts, H., Hayes, H., Ladosz, P., Crawley, D., and Roberts, G.: Measurement of boundary layer ozone concentrations on-board a Skywalker unmanned aerial vehicle, Atmos. Sci. Let., 15, 252-258, 2014.

Indhumathy, D., Seshaiah, C.V., and Sukkiramathi, K.: Estimation of Weibull Parameters for Wind speed calculation at Kanyakumari in India, Int. J. of Innovative Research in Science, Engineering and Technology, 3, 1, ISSN: 2319-8753, 8340-8345, 2014.

Ingleby, B., Moore, D., Sloan, C., and Dunn, R.: Evolution and Accuracy of Surface Humidity Reports, J. Atmos. Ocean Tech., 30, 2025-2043, https://doi.org/10.1175/JTECH-D-12-00232.1, 2013.

IPCC, 2013: Climate Change 2013: The Physical Science Basis. Contribution of Working Group I to the Fifth Assessment Report of the Intergovernmental Panel on Climate Change [Stocker, T.F., D. Qin, G.-K. Plattner, M. Tignor, S.K. Allen, J. Boschung, A. Nauels, Y. Xia, V. Bex and P.M. Midgley (eds.)]. Cambridge University Press, Cambridge, United Kingdom and New York, NY, USA, 1535 pp, doi:10.1017/CBO9781107415324, 2013.

Jaatinen, A., Hamed, A., Joutsensaari. J., Mikkonen, S., Birmili, W., Wehner, B., Spindler, G., Wiedensohler, A., Decesari, S., Mircea, M., Facchini, M.C., Junninen, H., Kulmala, M., Lehtined, K.E.J., and Laaksonen, A.: A comparison of new particle formation

https://doi.org/10.24355/dbbs.084-201906170934-0

events in the boundary layer at three different sites in Europe, Boreal Environ. Res., 14, 481–498, 2009.

Jiménez, M.A., and Cuxart, J.: A study of the nocturnal flows generated in the north side of the Pyrenees, Atmospheric Research, 145146, 244254, doi: 10.1016/j.atmosres.2014.04.010, 2014.

Jonassen, M.O., Tisler, P., Altstädter, B., Scholtz, A., Vihma, T., Lampert, A., König-Langlo, G., and Lüpkes, C.: Application of remotely piloted aircraft systems in observing the atmospheric boundary layer over Antarctic sea ice in winter, Polar Research, 34, 25651, http://dx.doi.org/10.3402/polar.v34.25651, 2015.

Justus, C.G., and Mikhilai, A.: Height variation of wind speed and wind distribution statistics, Geophys. Res. Lett., 3, 261-264, 1976.

Kaimal, J.C., and Finnigan, J.J.: Atmospheric Boundary Layer Flows, Their Structure and Measurement, Oxford University Press, New York, 289 pp., 1994.

Kallistratova, M., Kouznetsov, R.D., Kuznetsov, D.D., Kuznetsova, I.N., Nakhaev, M., and Chirokova, G.: Summertime low-level jet characteristics measured by sodars over rural and urban areas, Meteorol. Z., 18: 3, 289-295, 2009.

Kallistratova, M.A., Kouznetsov, R.D., Kramar, V.F., and Kuznetsov, D.D.: Profiles of Wind Speed Variances within Nocturnal Low-Level Jets Observed with a Sodar, J. Atmos. Ocean. Technolog., 30, 1970-1977, 2013.

Kannosto, J., Virtanen, A., Lemmetty, M., Mäkelä, J. M., Keskinen, J., Junninen, H., Hussein, T., Aalto, P., and Kulmala, M.: Mode resolved density of atmospheric aerosol particles, Atmos. Chem. Phys., 8, 5327–5337, doi:10.5194/acp-8-5327-2008, 2008.

Kanzow, T.: The Expedition PS109 of the Research Vessel POLARSTERN to the Nordic Seas in 2017 , Berichte zur Polar- und Meeresforschung/Reports on polar and marine research, Bremerhaven, Alfred Wegener Institute for Polar and Marine Research, 715, 139 pp., $http://epic.awi.de/46164/1/BzPM_0715_2018.pdf$, 2018.

Kaplan, M.L., Lin, Y.-L., Charney, J.J., Pfeiffer, K.D., Ensley, D.B., DeCroix, D.S., and Weglarz, R.P.: A Terminal Area PBL Prediction System at Dallas – Fort Worth and Its Application in Simulating Diurnal PBL Jets, Bull. Am. Met. Soc., 81, 9, 2179-2204, 2000.

Keil A., and Wendisch M.: Bursts of Aitken mode and ultrafine particles observed at the top of continental boundary layer clouds, J. Aerosol Sci., 32, 649-660, 2001.

Klaus, D., Dorn, W., Dethloff, K., Rinke, A., and Mielke, M.: Evaluation of Two Cloud Parameterizations and Their Possible Adaptation to Arctic Climate Conditions, Atmosphere, 3, 419-450, 2012.

Knippertz, P., Coe, H., Chiu, J.C., Evans, M.J., Fink, A.H., Kalthoff, N., Liousse, C., Mari, C., Allan, R.P., Brooks, B., Danour, S., Flamant, C., Jegede, O.O., Lohou, F., and

https://doi.org/10.24355/dbbs.084-201906170934-0

Marsham, J.H.: The DACCIWA project: Dynamics-aerosol chemistry-cloud interactions in West Africa, Bull. Am. Met. Soc., 10.1175/BAMS-D-14-00108.1, 1451-1460, 2015.

Kolmogorov, A.: Local structure of turbulence in an incompressible fluid for very large Reynolds numbers, Dokl. Akad. Nauk. SSSR, 30, 299–303, 1941.

Konrad, T.G., Hill, M.L., Rowland, J.R., and Meyer, J.H.: A Small, Radio-Controlled Aircraft As A Platform For Meteorological Sensors, Johns Hopkins APL Tech. Dig., 10, 11–21, 1970.

Korhonen, P., Kulmala, M., Laaksonen, A., Viisanen, Y., McGraw, R., and Seinfeld, J.: Ternary nucleation of H_2SO_4, NH_3, and H_2O in the atmosphere, J. Geophys. Res., Atmosphere, 104, D21, 26,349–26,353, 1999.

Kottmeier, C., Lege, D., Roth, R.: Nächtliche Windmaxima in der Grenzschicht über der Norddeutschen Tiefebene, Ann. Meteorol., 16, 93-95, 1980.

Krautstrunk, M. and Giez, A.: The Transition From FALCON to HALO Era Airborne Atmospheric Research, in Atmospheric Physics, edited by U. Schumann, pp. 609–624., 2012.

Kräuchi, A. and Philipona, R.: Return glider radiosonde for in situ upper-air research measurements, Atmos. Meas. Tech., 9, 2535-2544, doi:10.5194/amt-9-2535-2016, 2016.

Kraus, H., Malcher, J., Schaller, E.: A nocturnal Low Level Jet during PUKK, Bound.-Layer Meteorol., 31, 187-195, 1985.

Krauspe, P.: Beiträge zur Längsbewegung von Flugzeugen in Windscherungen, PhD thesis TU Braunschweig, http://www.digibib.tu-bs.de/?docid=00024338, 187 pp., 1983.

van den Kroonenberg A.C., Martin T., Buschmann M., Bange J., and Vörsmann, P.: Measuring the Wind Vector Using the Autonomous Mini Aerial Vehicle M^2AV, J. Atmos. Ocean. Technolog., 25, 1969-1982, 2008.

van den Kroonenberg, A., Martin, S., Beyrich, F., and Bange, J.: Spatially-Averaged Temperature Structure Parameter Over a Heterogeneous Surface Measured by an Unmanned Aerial Vehicle, Bound.-Lay. Meteorol., 142, 55-77, 2012.

Kulmala, M., Vehkamäki, H., Petäjä, T., Dal Maso, M., Lauri, A., Kerminen, V.-M., Birmili, W., and McMurry, P. H.: Formation and growth rates of ultrafine atmospheric particles: a review of observations, Aerosol Sci., 35, 143–176, 2004.

Kulmala, M., Riipinen, I., Sipilä, M., Manninen, H.E., Petäjä, T., Junninen, H., Dal Maso, M., Mordas, G., Mirme, A., Vana, M., Hirsikko, A., Laakso, L., Harrison, R.M., Hanson, I., Leung, C., Lehtined, K.E.J., Kerminen, V.M.: Toward direct measurement of atmospheric nucleation, Science, 318, 5847, 89–92, 2007.

Lafore, J.P., Stein, J., Asencio, N., Bougeault, P., Ducrocq, V., Duron, J., Fisher, C., Héreil, P., Mascart, P., Pinty, J.P., Redelsperger, J.L., Richard, E., de Arellano, J.V.G.: The meso-NH atmospheric simulation system. Part I: adiabatic formulation and control simulation, Ann. Geophys., 16, 90109, 1998.

https://doi.org/10.24355/dbbs.084-201906170934-0

Lampert, A., Bernalte Jimenez, B., Wulff, D., and Kenull, T.: One-year observations of the wind distribution and low-level jet occurrence at Braunschweig, North German Plain, Wind Energy, 19, 10, 1807–1817, DOI: 10.1002/we.1951, 2015.

Lampert, A., Pätzold, F., Jiménez, M.A., Lobitz, L., Martin, S., Lohmann, G., Canut, G., Legain, D., Bange, J., Martínez-Villagrasa, D., and Cuxart, J.: A study of local turbulence and anisotropy during the afternoon and evening transition with an unmanned aerial system and mesoscale simulation, Atmos. Chem. Phys., 16, 8009-8021, 2016.

Lampert, A., Hartmann, J., Pätzold, F., Lobitz, L., Hecker, P., Kohnert, K., Larmanou, E., Serafimovich, A., and Sachs, T.: Comparison of Lyman-Alpha and LICOR infrared hygrometers for measuring airborne turbulent fluctuations of water vapor, Atmos. Meas. Tech. Diss., https://doi.org/10.5194/amt-2017-353, 2018.

Lampert, A., Degenhardt, J., Cañadillas, B., Siedersleben, S., Hankers, R., Rausch, T., Teichert, D., Platis, A., Bärfuss, K., Djath, B., Schulz-Stellenfleth, J., Bange, J., Neumann, T., and Emeis, S.: Low Level Jet spatial variability and wind energy production – a case study using airborne and gondola wind speed measurements, in preparation for Wind Energy, 2018.

Langer, M., Westermann, S., Muster, S., Piel, K., and Boike, J.: The surface energy balance of a polygonal tundra site in northern Siberia Part 1: Spring to fall, The Cryosphere, 5, 151–171, 2011.

Legain, D., Bousquet, O., Douffet, T., Tzanos, D., Moulin, E., Barrie, J., and Renard, J.-B.: High frequency boundary layer profiling with reusable radiosondes, Atmos. Meas. Tech., 6, 2195-2205, 2013.

Leiding, T. et al.: Standardization and comparative analysis the meteorological FINO measurement data (FINO 123). Project report, Grant number: 0325508, 2016

Lenschow, D.H.: The Measurement of Air Velocity and Temperature Using the NCAR Buffalo Aircraft Measuring System; National Center for Atmospheric Research, Boulder Colorado, NCAR-TN/EDD-74, 39 pp., 1972.

Lenschow, D.H., Li, X.S., Zhu, C.J., and Stankov, B.B.: The stably stratified boundary layer over the Great Plains. I. Mean and turbulence structure. Bound.-Layer Meteor., 42, 95-121, 1988.

Lenschow, D.H., Mann, J., and Kristensen, L: How Long is Long Enough When Measuring Fluxes and Other Turbulence Statistics?, J. Atmos. Ocean. Technolog., 11, 661-673, 1994.

Li, X.-M., and Lehner, S.: Observation of TerraSAR-X for studies on offshore wind turbine wake in near and far fields, IEEE Journal of Selected Topics in Applied Earth Observations and Remote Sensing, 6, 1757-1769, 2013.

https://doi.org/10.24355/dbbs.084-201906170934-0

Li-Cor LI-7500A Open Path CO2/H2O Gas Analyser Instruction Manual, Li-Cor Inc., *http* : *//www.kohsieh.com.tw/PDF_Files/LICOR/manual/LI* − *7500A_Manual.pdf*, 2014.

Lothon, M., Lohou, F., Pino, D., Couvreux, F., Pardyjak, E. R., Reuder, J., Vilà-Guerau de Arellano, J., Durand, P, Hartogensis, O., Legain, D., Augustin, P., Gioli, B., Lenschow, D. H., Faloona, I., Yagüe, C., Alexander, D. C., Angevine, W. M., Bargain, E, Barrié, J., Bazile, E., Bezombes, Y., Blay-Carreras, E., van de Boer, A., Boichard, J. L., Bourdon, A., Butet, A., Campistron, B., de Coster, O., Cuxart, J., Dabas, A., Darbieu, C., Deboudt, K., Delbarre, H., Derrien, S., Flament, P., Fourmentin, M., Garai, A., Gibert, F., Graf, A., Groebner, J., Guichard, F., Jiménez, M. A., Jonassen, M., van den Kroonenberg, A., Magliulo, V., Martin, S., Martinez, D., Mastrorillo, L., Moene, A. F., Molinos, F., Moulin, E., Pietersen, H. P., Piguet, B., Pique, E., Romàn-Cascòn, C., Rufin-Soler, C., Saïd, F., Sastre-Marugàn, M., Seity, Y., Steeneveld, G. J., Toscano, P., Traullé, O., Tzanos, D., Wacker, S., Wildmann, N., and Zaldei, A.: The BLLAST field experiment: Boundary-Layer Late Afternoon and Sunset Turbulence, Atmos. Chem. Phys., 14, 10931-10960, doi:10.5194/acp-14-10931-2014, 2014.

Lu, H., and Porté-Agel, F.: On the impact of wind farms on a convective atmospheric boundary layer, Bound.-Layer Meteorol. 157, 81–96, 2015.

Luftfahrtnorm: LN 9300, Blatt 1, Flugmechanik. Normenstelle Luftfahrt, Leinfelden, Germany, 42 pp., 1970.

Luhar, A.K.: Estimating Variances of Horizontal Wind Fluctuations in Stable Conditions, Bound.-Layer Meteorol., 135, 301-311, 2010.

Lyubovtseva, L., Sogacheva, L., Dal Maso, M., Bonn, B., Keronen, P., and Kulmala, M.: Seasonal variations of trace gases, meteorological parameters, and formation of aerosols in boreal forests, Boreal Environ. Res., 10, 493-510, 2005.

Mahrt, L., Heald, R.C., Lenschow, D.H., Stankov, B.B., and Troen, I.: An observational study of the structure of the nocturnal boundary layer, Bound.-Layer Meteorol., 17, 247-264, 1979.

Mahrt, L.: The early evening boundary layer transition. Quart. J. Roy. Meteor. Soc., 107, 329–343, 1981.

Marti, J.J., Weber, R.J., Saros, M.T., Vasiliou, J.G., and McMurry, P.H.: Modification of the TSI3025 Condensation Particle Counter for Pulse Height Analysis, Techncal Note, Aerosol Science and Technology, 25, 214-218, 1996.

Martin, S., Bange, J., and Beyrich, F.: Meteorological profiling of the lower troposphere using the research UAV "M^{2}AV Carolo", Atmos. Meas. Tech., 4, 705-716, 2011.

Martin, S., and Bange, J.: The Influence of Aircraft Speed Variations on Sensible Heat-Flux Measurements by Different Airborne Systems, Bound.-Layer Meteorol., 150, 153-166, 2014.

https://doi.org/10.24355/dbbs.084-201906170934-0

Martin, S., Beyrich, F., and Bange, J.: Observing Entrainment Processes Using a Small Unmanned Aerial Vehicle: A Feasibility Study, Bound.-Layer Meteorol., 150, 449-467, doi:10.1007/s10546-013-9880-4, 2014.

Mason, P.J., and Thomson, D.J.: Large-Eddy simulations of the neutral-static-stability planetary boundary layer, Q. J. Royal Meteorol. Soc., 113, 476, 413-443, 1987.

Mauritsen, T., and Svensson, G.: Observations of Stably Stratified Shear-Driven Atmospheric Turbulence at Low and High Richardson Numbers, J. Atmos. Sci., 64, 645-655, 2007.

May, R.D.: Open-path, near-infrared tunable diode laser spectrometer for atmospheric measurements of H_2O, J., Geophys. Res., 103, D15, 19161-19172, 1998.

Meischner, P., Baumann, R., Höller, H., and Jank, T.: Eddy Dissipation Rates in Thunderstorms Estimated by Doppler Radar in Relation to Aircraft In Situ Measurements, J. Atmos. Ocean. Technolog., 18, 1609-1627, 2001.

Moore, C.J.: Frequency response corrections for eddy correlation systems, Bound.-Layer Meteorol., 37, 17-35, 1986.

Nadeau, D. F., Pardyjak, E. R., Higgins, C. W., Fernando, H. J. S., and Parlange, M. B.: A simple model for the afternoon and early evening decay of convective turbulence over different land surfaces, Bound.-Layer Meteorol., 141, 301-324, 2011.

Nakanishi, M., Shibuya, R., Ito, J., and Niino, H.: Large-Eddy Simulation of a Residual Layer: Low-Level Jet, Convective Rolls, and Kelvin-Helmholtz Instability, J. Atmos. Scie., 71, 4473-4491, 2014.

Neddermann, B. and Neumann, T.: Realistic Scenario for the Offshore Wind Power Development in Germany, DEWI Mag., 47, 62-66, 2015.

Newman, J.F., Klein, P.M., Wharton, S., Sathe, A. Bonin, T.A., Chilson, P.B., and Muschinski, A.: Evaluation of three lidar scanning strategies for turbulence measurements, Atmos. Meas. Tech., 9, 1993-2013, 2016.

Nilsson, E., Rannik, Ü., Kulmala, M., Buzorius, G., O'Dowd, C.: Effects of continental boundary layer evolution, convection, turbulence and entrainment, on aerosol formation, Tellus B, 53, 4, 441–461, 2001.

O'Dowd, C., McFiggans, G., Creasey, D.J., Pirjola, L., Hoell, C., Smith, M.H., Allan, B.J., Plane, J., Heard, D.E., Lee, J.D., Pilling, M.J., and Kulmala, M.: On the photochemical production of new particles in the coastal boundary layer. Geophys. Res. Lett., 26, 12, 1707–1710, 1999.

O'Dowd C.D., Yoon Y.J., Junkermann W., Aalto P., Kulmala M., Lihavainen H., and Viisanen Y.: Airborne measurements of nucleation mode prticles II: boreal forest nucleation events, Atmos. Chem. Phys., 9, 937-944, 2009.

Oppenheim, A.V., Schafer„ R.W., and Buck, J.R.: Discrete-Time Signal Processing, 2nd Ed. Upper Saddle River, NJ: Prentice Hall, ISBN:0-13-754920-2, 870 pp., 1999.

https://doi.org/10.24355/dbbs.084-201906170934-0

Palomaki, R.T., Rose, N.T., van den Bossche, M., Sherman, T.J., and De Wekker, S.F.J.: Wind estimation in the Lower Atmosphere Using Multirotor Aircraft, J. Atmos. Ocean. Technolog., https://doi.org/10.1175/JTECH-D-16-0177.1, 1183-1191, 2017.

Paluch, I.R., and Baumgardner, D.G.: Entrainment and Fine-Scale Mixing in a Continental Convective Cloud, J. Atmos. Sci., 46, 2, 261-278, 1989.

Pätzold, F.: Windmessung mittels Segelflugzeug, PhD thesis, TU Braunschweig, 192 pp., 2017.

Parish, T.R.: Forcing of the Summertime Low-Level Jet along the California Coast, J. Appl. Meteorol., 39, 2421-2433, 2000.

Paulsen, U.S., and Wagner, R.: IMPER: Characterization of the wind field over a large wind turbine rotor. Final report 2012, ISSN 0106-2840, ISBN 978-87-92896-00-1.Roskilde, Denmark: DTU 2012 Available from: http://orbit.dtu.dk/fedora/objects/orbit:110344/datastreams/file7653538/content, 2012.

Pillai, D., Gerbig, C., Ahmadov, R., Rödenbeck, C., Kretschmer, R., Koch, T., Thompson, R., Neininger, B., and Lavrié, J. V.: High-resolution simulations of atmospheric CO2 over complex terrain - representing the Ochsenkopf mountain tall tower, Atmos. Chem. Phys., 11, 7445-7464, 2011.

Platis, A., Altstädter, B., Wehner, B., Wildmann, N., Lampert, A., Hermann, M., Birmili, W., and Bange, J.: An Observational Case Study on the Influence of Atmospheric Boundary-Layer Dynamics on New Particle Formation, Bound.-Layer Meteorol., 158, 1, 67-92, 2015.

Platis, A., Siedersleben, S., Bange, J., Lampert, A., Bärfuss, K., Hankers, R., Cañadillas, B., Foreman, R., Schulz-Stellenfleth, J., Djath, B., Neumann, T., and Emeis, S.: First in situ evidence of wakes in the far field behind offshore wind farms, Scientific Reports, doi 10.1038/s41598-018-20389-y, 2018.

Prabha, T.V., Leclerc, M.Y., Karipot, A., Hollinger, D.Y., and Mursch-Radlgruber, E.: Influence of Nocturnal Low-level Jets on Eddy-covariance Fluxes over a Tall Forest Canopy, Bound.-Layer Meteorol., 126, 219-236, 2008.

Prabha, T.V., Hoogenboom, G., and Smirnova, T.G.: Role of land surface parameterizations on modeling cold-pooling events and low-level jets, Atmospheric Research, 99, 147-161, 2011.

Ramanathan, V., Cess, R.D., Harrison, E.F., Minnis, P., Barkstrom, B.R., Ahmad, E., and Hartmann, D.: Cloud-radiative forcing and climate: Results from the earth radiation budget experiment, Science, 243, 57–63, 1989.

Ramanathan, V., Ramana, M.V., Roberts, G., Kim, D., Corrigan, C., Chung, C., and Winker, D.: Warming trends in Asia amplified by brown cloud solar absorption. Nature, 448, 575–578, doi:10.1038/nature06019„ 2007.

https://doi.org/10.24355/dbbs.084-201906170934-0

Reineman, B.D., Lenain, L., Statom, N.M., and Melville,W.K.: Development and Testing of Instrumentation for UAV-Based Flux Measurements within Terrestrial and Marine Atmospheric Boundary Layers, J. Atmos. Ocean Tech., 30, 1295-1319, DOI:10.1175/JTECH-D-12-00176.1, 2013.

Reuder, J., Brisset, P., Jonassen, M., Müller, M. and Mayer, S.: The small unmanned meteorological observer SUMO: A new tool for atmospheric boundary layer research. Meteor. Z., 18, 141–147, 2009.

Román-Cascón, C., Yagüe, C., Mahrt, L., Sastre, M., Steeneveld, G.-J., Pardyjak, E., van de Boer, A., and Hartogensis, O.: Interactions among drainage flows, gravity waves and turbulence: a BLLAST case study, Atmos. Chem. Phys., 15, 9031-9047, doi:10.5194/acp-15-9031-2015, 2015.

Rose„ C., Sellegri, K., Asmi, E., Hervo, M., Freney, E., Colomb, A., Junninen, H., Duplissy, J., Sipilä, M., Kontkanen, J., Lehtipalo, K., and Kulmala, M.: Major contribution of neutral clusters to new particle formation at the interface between the boundary layer and the free troposphere, Atmos. Chem. Phys., 15„ 3413-3428, 2015.

Sachs, T., Wille, C., Boike, J., and Kutzbach, L.: Environmental controls on ecosystem-scale CH4 emission from polygonal tundra in the Lena River Delta, Siberia, J. Geophys. Res., 113, G00A03, doi:10.1029/2007JG000505, 12pp., 2008.

Sandu, I., Beljaars, A., Bechtold, P., Mauritsen, T., and Balsamo, G.: Why is it so difficult to represent stably stratified conditions in numerical weather prediction (NWP) models? J. Advan. Model. Earth Syst., 5, 117–133, 2013.

Sauer, M., Hauf, T., Sakiew, L., Chan,P.W., Tse, S.-M., and Hupe, P.: On the Identification of Weather Avoidance Routes in the terminal maneuvering area of Hong Kong International Airport, Journal of Zhejiang University - Science A, Appl. Phys. and Eng., 17, 3, 171-185, 2016.

Saunders, P.M.: Sea smoke and steam fog, Q. J. Roy. Met. Soc., 90, 384, 156–165, 1964.

Savijärvi, H., Niemelä, S., and Tisler, P.: Coastal winds and low-level jets: Simulations for sea gulfs, Q. J. Roy. Met. Soc., 131, 625-637, 2005.

Schiller, C., Krämer, M., Afchine, A., Spelten, N., and Sitnikov, N.: The ice water content in Arctic, midlatitude and tropical cirrus, J. Geophys. Res., 113, D24208, doi:10.1029/2008JD010342, 2008.

Schmeissner, T., Shaw, R.A., Ditas, J., Stratmann, F., Wendisch, M., and Siebert, H.: Turbulent Mixing in Shallow Trade Wind Cumuli: Dependence on Cloud Life Cycle, J. Atmos. Scie, 71, 2810-2822, 2014.

Schmitgen, S., Geiß, H., Ciais, P., Neininger, B., Brunet, Y., Reichstein, M., Kley, D., and Volz-Thomas, A.: Carbon dioxide uptake of a forested region in southwest France derived from airborne CO2 and CO measurements in a quasi-Lagrangian experiment, J. Geophys. Res., 109, D14302, doi:10.1029/2003JD004335, 2004.

https://doi.org/10.24355/dbbs.084-201906170934-0

Scholtz, A., Kaschwich, C., Krüger, T., Kufieta, K., Schnetter, P., Wilkens, C.-S., and Vörsmann, P.: Development of a new multi-purpose UAS for scientific application, Proceedings of the International Conference on Unmanned Aerial Vehicle in Geomatics (UAV-g), Zurich, Switzerland, 14-16 September 2011, XXXVIII-1/C22, 149-154, 2011.

Shapiro, A., and Fedorovich, E.: Analytical description of a nocturnal low-level jet, Q.J.R. Meteorol. Soc., 136, 1255-1262, 2010.

Siebert, H., Stratmann, F., Wehner, B.: First observations of increased ultrafine particle number concentrations near the inversion of a continental planetary boundary layer and its relation to ground-based measurements, Geophys. Res. Lett., 31, 9, L09102, 2004.

Siebert, H., Wehner, B., Hellmuth, O., Stratmann, F., Boy, M., and Kulmala, M.: New particle formation in connection with a nocturnal low-level jet: Observations and modeling results, Geophys. Res. Lett., 34, L16822, doi:10.1029/2007GL029891, 2007.

Siebert, H., Beals, M., Bethke, J., Bierwirth, E., Conrath, T., Dieckmann, K., Ditas, F., Ehrlich, A., Farrell, D., Hartmann, S., Izaguirre, M.A., Katzwinkel, J., Nuijens, L., Roberts, G., Schäfer, M., Shaw, R.A., Schmeissner, T., Serikov, I., Stevens, B., Stratmann, F., Wehner, B., Wendisch, M., Werner, F., and Wex, H.: The fine-scale structure of the trade wind cumuli over Barbados - an introduction to the CARRIBA project, Atmos. Chem. Phys., 13, 10061-10077, 2013.

Siedersleben, S.K., Platis, A., Lundquist, J.K., Lampert, A., Bärfuss, K., Cañadillas, B., Djath, B., Schulz-Stellenfleth, J., Neumann, T., Bange, J., and Emeis, S.: Evaluation of a Wind Farm Parametrization for Mesoscale Atmospheric Flow Models with Aircraft Measurements, submitted to Meteorologische Zeitschrift, 2018.

Siedersleben, S.K., Platis, A., Lundquist, J.K., Lampert, A., Bärfuss, K., Cañadillas, B., Djath, B., Schulz-Stellenfleth, J., Neumann, T., Bange, J., and Emeis, S.: Micrometeorological Impacts of Offshore Wind Farms as seen in Observations and Simulations, submitted to Geophys. Res. Lett., 2018.

https://en.wind-turbine-models.com/turbines/646-siemens-swt-3.6-120-onshore, accessed on 26 February 2018.

Sievers, J., Papakyriakou, T., Larsen, S.E., Jammet, M.M., Rysgaard, S., Sejr, M.K., and Sorensen, L.L.: Estimating surface fluxes using eddy covariance ans numerical ogive optimization, Atmos. Chem. Phys., 15, 2081–2103, 2015.

Smedman, A.-S., Bergström, H., and Grisogono, B.: Evolution of stable internal boundary layers over a cold sea, J. Geophys. Res. Ocean., 102, 1091–1099, 1997.

Soddell, J., McGuffie, K., and Holland, G.: Intercomparison of atmospheric soundings from the aerosonde and radiosonde. J. Appl. Meteor., 43, 1260–1269, 2004.

Sodemann, H., Aemisegger, F., Pfahl, S., Bitter, M., Corsmeier, U., Feuerle, F., Graf, P., Hankers, R., Hsiao, G., Schulz, H., Wieser, A., and Wernli, H.: The stable isotope composition of water vapour above Corsica during the HyMeX SOP1: insight into vertical

https://doi.org/10.24355/dbbs.084-201906170934-0

mixing processes from lower-tropospheric survey flights, Atmos. Chem. Phys. Discuss., doi:10.5194/acp-2016-728, 2016.

Song, J., Liao, K., Coulter, R.L. and Lesht, B.M.: Climatology of the low-level jet at the southern Great Plains Atmospheric Boundary Layer Experiment Site. J. Appl. Meteor., 44, 1593-1606, 2005.

Spiess, T., Bange, J., Buschmann, M., and Vörsmann, P.: First application of the meteorological Mini-UAV 'M^{2}AV', Meteorologische Zeitschrift, 16, 2, 159-169, 2007.

Spindler, G., Grüner, A., Müller, K., Schlimper S., and Herrmann, H.: Long-term size-segregated particle (PM10, PM2.5, PM1) characterization study at Melpitz–influence of air mass inflow, weather conditions and season, J. Atmos. Chem., 70, 2, 165–195, 2013.

Spracklen D. V., Carslaw K. S., Kulmala M., Kerminen V.-M., Sihto S.-L., Riipinen I., Merikanto J., Mann G. W., Chipperfield M. P., Wiedensohler A., Birmili W., and Lihavainen H.: Contribution of particle formation to global cloud condensation nuclei concentration, J. Geophys. Res,.35, L06808, doi:10.1029/2007GL033038, 2008.

Steele, C.J., Dorling, S.R., von Glasow, R., and Bacon, J.: Modelling sea-breeze climatologies and interactions on coasts in the southern North Sea: implications for offshore wind energy, Q.J.R. Meteorol. Soc., 141, 1821-1835, 2015.

Stensrud, D.J.: Importance of Low-Level Jets to Climate: A Review. Journal of Climate, 9: 1698-1711, 1996.

Stevens, M.J.M., and Smulders, P.T.: The estimation of the parameters of the Weibull wind speed distribution for wind energy utilization purposes, Wind Engineering, 3, 2, 132-145, 1979.

Stickney, T.M., Shedlov, M.W., and Thompson, D.I.: Goodrich Total Temperature Sensors, Technical Report, 5755, C, 32 pp. http://www.faam.ac.uk/index.php/faam-documents/science-instruments/47-rosemount-report-5755/file, 1994.

Stone, R., Herber, A., Vitale, V., Mazzola, M., Lupi, A., Schnell, R., Dutton, E., Liu, P., Li, S.-M., Dethloff, K., Lampert, A., Ritter, C., Stock, M., Neuber, R., and Maturilli, M.: A three-dimensional characterization of Arctic aerosols from airborne Sun Photometer observations; PAM-ARCMIP – April 2009, J. Geophys. Res., 115, D13203, DOI: 10.1029/2009JD013605, 2010.

Storm, B., Dudhia, J., Basu, S., Swift, A., and Giammanco, I.: Evaluation of the Weather Research and Forecasting model on Forecasting Low-Level Jets: Implications for Wind Energy, Wind Energy, 12, 81-90, 2009.

Stratmann, F., Siebert, H., Spindler, G., Wehner, B., Althausen, D., Heintzenberg, J., Hellmuth, O., Rinke, R., Schmieder, U., Seidel, C., Tuch, T., Uhrner, U., Wiedensohler, A., Wandinger, U., Wendisch, M., Schell, D., and Stohl, A.: New-particle formation events in a continental boundary layer: first results from the SATURN experiment, Atmos. Chem. Phys., 3, 1445–1459, doi:10.5194/acp-3-1445-2003, 2003.

https://doi.org/10.24355/dbbs.084-201906170934-0

Stull, R.B.: An Introduction to Boundary Layer Meteorology, Kluwer Academic Publishers, Reprint 1991, 666 pp., 1988.

Stull, R.: Practical Meteorology: An Algebra-based Survey of Atmospheric Science -version 1.02b, Univ. of British Columbia, ISBN 978-0-88865-283-6, 940 pp., 2017.

Tagawa, M., Kato, K., and Ohta, Y.: Response compensation of temperature sensors: Frequency-domain estimation of thermal time constants, Rev. Sci. Instrum., 74, 3171–3174, 2003.

Tatarskii V.I.: The effects of the turbulent atmosphere on wave propagation, Israel Program for Scientific Translations, Jerusalem, 472 pp., 1971.

Taylor, G.I.: The spectrum of turbulence, Proc. Roy. Soc. Lond., 164, 476–490, 1938.

Tetzlaff, A., Lüpkes, C., and Hartmann, J.: Aircraft-based observations of atmospheric boundary-layer modifications over Arctic leads, Q. J. Roy. Met. Soc., 14, 2839-2856, 2015.

Thebaud, L.: An atmospheric turbulent velocity spectrum for three dimensions, J. Geophys. Res., 109, D10109, doi:10.1029/2002JD003173, 2004.

Thomas, R.M., Lehmann, K., Nguyen, H., Jackson, D.L., Wolfe, D., and Ramanathan, V.: Measurement of turbulent water vapor fluxes using a lightweight unmanned aerial vehicle system, Atmos. Meas. Tech., 5, 243-257, 2012.

Trenberth, K. E., Jones, P. D., Ambenje, P., Bojariu, R., Easterling, D., Klein Tank, A., Parker, D., Rahimzadeh, F., Renwick, J. A., Rusticucci, M., Soden, B., and Zhai, P.: Observations: Surface and Atmospheric Climate Change, in: Climate Change 2007: The Physical Science Basis. Contribution of Working Group I to the Fourth Assessment Report of the Intergovernmental Panel on Climate Change, edited by: Solomon, S., Qin, D., Manning, M., Chen, Z., Marquis, M., Averyt, K. B., Tignor, M., and Miller, H. L., Cambridge University Press, Cambridge, United Kingdom and New York, NY, USA, 2007.

Troldborg, N., Larsen„ G.C., Madsen, H.A., Hansen, K.S., Sorensen, J.N., and Mikkkelsen, R.: Numerical simulations of wake interaction between two wind turbines at various inflow conditions. Wind Energy 14, 859–876, 2011.

Türk, M., and Emeis, S.: The dependence of offshore turbulence intensity on wind speed, Journal of Wind Engineering and Industrial Aerodynamics, 98, 8,466–471, 2010.

Twohy, C.H., Schanot, A.J., and Cooper, W.A.: Measurement of Condensed Water Content in Liquid and Ice Clouds Using an Airborne Counterflow Virtual Impactor, J. Atmos. Ocean. Technolog., 14, 197-202, 1997.

Vautard, R., Thais, F., Tobin, I., Bréon, F.M., Devezeaux de Lavergne, J.G., Colette, A., Yiou, P., and Ruti, P.M.: Regional climate model simulations indicate limited climatic impacts by operational and planned european wind farms, Nat. communications, 5, 3196, 2014.

https://doi.org/10.24355/dbbs.084-201906170934-0

Villa, T.F., Gonzalez, F., Miljievic, B., Ristovski, Z.D., and Morawska, L.: An Overview of Small Unmanned Aerial Vehicles for Air Quality Measurements: Present Applications and Future Prospectives, Sensors, doi:10.3390/s16071072, 29 p., 2016.

Villa, T.F., Jayaratne, E.R., Gonzalez, L.F., and Morawska, L.: Determination of the vertical profile of particle number concentration adjacent to a motorway using an unmanned aerial vehicle, Environmental Pollution, 230, 134-142, 2017.

Vörsmann, P.: Ein Beitrag zur bordautonomen Windmessung. Ph.D. thesis, Techn. Univ. Braunschweig, Germany, 117 pp., 1985.

Wächter, M., Rettenmeier, A., Kühn, M., and Peinke, J.: Characterization of short time fluctuations in atmospheric wind speeds by LIDAR measurements. Meteorologische Zeitschrift, 18, 3, 277-280, 2009.

Wagner, R., Antoniou, I., Pedersen, S.M., Courtney, M., and Jorgensen, H.E., The influence of the Wind Speed Profile on Wind Turbine Performance Measurements, Wind Energy, 12 (4) 348–362 Available from: http://dx.doi.org/10.1002/we.297, 2009.

Wagner, R., Courtney, M., Gottschall, J., and Lindelow, P.: Accounting for the speed shear in wind turbine power performance measurement, Wind Energy, 14 (8) 993–1004 Available from: http://dx.doi.org/10.1002/we.509, 2011.

Wagner, R., Cañadillas, B., Clifton, A., Feeney, S., Nygaard, N., Poodt, M., St. Martin, C., Tüxen, E., and Wagenaar, J.W.: Rotor equivalent wind speed for power curve measurement – comparative exercise for IEA Wind Annex 32, J. Phys.: Conf. Ser. 2014, 524, 012108, Available from: http://stacks.iop.org/1742-6596/524/i=1/a=012108, 2014.

Wang, Y., Klipp, C.L., Garvey, D.M., Ligon, D.A., Williamson, C.C., Chang, S.S., Newsom, R.K., and Calhoun, R.: Nocturnal Low-Level-Jet-Dominated Atmospheric Boundary Layer Observed by a Doppler Lidar over Oklahoma City during JU2003, J. Appl. Meteorol. and Climatology, 46: 2098-2109, 2007.

Wehner, B., Siebert, H., Stratmann, F., Tuch, T., Wiedensohler, A., Petäjä, T., Dal Maso, M., Kulmala, M.: Horizontal homogeneity and vertical extent of new particle formation events, Tellus B, 59,3, 362–371, 2007.

Wehner, B., Siebert, H., Ansmann, A., Ditas, F., Seifert, P., Stratmann, F., Wiedensohler, A., Apituley, A., Shaw, R. A., Manninen, H. E., and Kulmala, M.: Observations of turbulence-induced new particle formation in the residual layer, Atmos. Chem. Phys., 10, 4319–4330, doi:10.5194/acp-10-4319-2010, 2010.

Wehner, B., Werner, F., Ditas, F., Shaw, R.A., Kulmala, M., and Siebert, H.: Observations of new particle formation in enhanced UV irradiance zones near cumulus clouds, Atmos. Chem. Phys., 15, 11701–11711, 2015.

Wiedensohler A., Cheng Y.F., Nowak A., Wehner B., Achtert P., Berghof M., Birmili W., Wu Z.J., Hu M., Zhu T., Takegawa N., Kita K., Kondo Y., Lou S.R., Hofzumahaus A., Holland F., Wahner A., Gunthe S.S., Rose D., Su H., and Pöschl U.: Rapid aerosol particle growth and increase of cloud condensation nucleus activity by secondary aerosol

https://doi.org/10.24355/dbbs.084-201906170934-0

formation and condensation: A case study for regional air pollution in northeastern China, J. Geophys. Res., 114, D00G08, doi:10.1029/2008JD010884, 2009.

Wiedensohler, A., Birmili, W., Nowak, A., Sonntag, A., Weinhold, K., Merkel, M., Wehner, B., Tuch, T., Pfeifer, S., Fiebig, M., Fjäraa, A., Asmi, E., Sellegri, K., Depuy, R., Venzac, H., Villani, P., Laj, P., Aalto, P., Ogren, J., Swietlicki, E., Williams, P., Roldin, P., Quincey, P., Hüglin, C., Fierz-Schmidhauser, R., Gysel, M., Weingartner, E., Riccobono, F., Santos, S., Grüning, C., Faloon, K., Beddows, D., Harrison, R., Monahan, C., Jennings, S., O'Dowd, C., Marinoni, A., Horn, H.G., Keck, L., Jiang, J., Scheckman, J., McMurry, P.H., Deng, Z., Zhao, C., Moerman, M., Henzing, B., de Leeuw, G., Löschau, G., Bastian, S.: Mobility particle size spectrometers: harmonization of technical standards and data structure to facilitate high quality long-term observations of atmospheric particle number size distributions, Atmos. Meas. Tech., 5,657–685, 2012.

Wildmann, N., Hofsäß, M., Weimer, F., Joos, A., and Bange, J.: MASC – a small Remotely Piloted Aircraft (RPA) for wind energy research, Adv. Sci. Res., 11, 55-61, DOI: 10.5194/asr-11-55-2014, 2014.

Wildmann, N., Kaufmann, F., and Bange, J.: An inverse-modelling approach for frequency response correction of capacitive humidity sensors in ABL research with small remotely piloted aircraft (RPA), Atmos. Meas. Tech., 7, 3059-3069, 2014.

Wildmann, N., Ravi, S., and Bange, J.: Towards higher accuracy and better frequency response with standard multi-hole probes in turbulence measurement with remotely piloted aircraft (RPA), Atmos. Meas. Tech. 2014, 7, 1027-1041, DOI:10.5194/amt-7-1027-2014, 2014.

Wildmann, N., Rau, G.A., and Bange, J.: Observations of the Early Morning Boundary-Layer Transition with Small Remotely-Piloted Aircraft, Bound.-Layer Meteorol., 157, 3, 345-373, 2015.

Wittich, K.-P., Hartmann, J., and Roth, R:. On nocturnal wind shear with a view to engineering applications, Bound.-Layer Meteorol., 37, 215-227, 1986.

Zöger, M., Afchine, A., Eicke, N., Gerhards, M.-T., Klein, E., McKenna, D., Mörschel, U., Schmidt, U., Tan, V., Tuitjer, F., Woyke, T., and Schiller, C.: Fast in situ stratospheric hygrometers: A new family of balloon-borne and airborne Lymanphotofragment fluorescence hygrometers., J. Geophys. Res., 104, 1807–1816, 1999.

Zhou, Y.P., Xu, K.-M., Sud, Y.C., and Betts, A.K.: Recent trends of the tropical hydrological cycle inferred from Global Precipitation Climatology Project and International Satellite Cloud Climatology Project data, J. Geophys. Res., 116, D09101, doi:10.1029/2010JD015197, 16 pp., 2011.

Zhou, L., Tian, Y., Baidya Roy, S., Thorncroft, C., Bosart, L.F., and Hu, Y.: Impacts of wind farms on land surface temperature, Nat. Clim. Chang. 2, 539–543, 2012.

Zondlo, M.A., Paige, M.E., Massick, S.M., and Silver, J.A., Vertical cavity laser hygrometer for the National Science Foundation Gulfstream-V aircraft, J. Geophys. Res., 115, D20309, doi:10.1029/2010JD014445, 14 pp., 2010.

https://doi.org/10.24355/dbbs.084-201906170934-0

Acknowledgements

This habilitation treatise is dedicated to my beloved grandparents. They have supported me and my (sometimes crazy) ideas throughout my life, and I would like to express my deepest gratitude.
Thinking back at my beginning at TU Braunschweig, I would like to thank Jens Bange and Prof. Dr.-Ing. Vörsmann for giving me the chance to work as a scientist at the Institute of Aerospace Systems, and for believing in my project ideas. A big thanks to Carsten Wiedemann and Simone Wolf for teaching me project management.
Then I would like to thank Peter Hecker, Thomas Feuerle, Ulf Bestmann, Rolf Hankers, and everybody at the Institute of Flight Guidance for the warm welcome in 2013, and for the great collaboration and team spirit. Thank you all for the inspiring environment, the mutual help and support, the sweets in the kitchen, and the coffee breaks. In particular I would like to thank my work group, Alex Peuker, Barbara Altstädter, Falk Pätzold, Konrad Bärfuss and Thomas Rausch. It is such a pleasure to discuss projects and their challenges and progress with you, and I enjoy going to work (almost) every day. A big thanks goes to Birgit Zachrau, Dagmar Piskol, Nicole Akcabelen and Renato Lumia for their great help with any kind of problem. Thanks to all the students who contribute so much to the projects during their student theses, or as student research assistants.
A big thanks to everybody helping to gather the data for the projects, and for the great atmosphere in the field - Alex Peuker, Andreas Scholtz, Barbara Altstädter, Endres Kathe, Falk Pätzold, Gerald Lohmann, Helmut Schulz, Henning Busse, Konrad Bärfuss, Lutz Bretschneider, Mark Bitter, Nico Weil, Rolf Hankers, Sabrina Martin, Simon Nieschke, Thomas Aschenbrenner, Thomas Feuerle, Thomas Krüger, and Thomas Rausch, and to all the project partners of other institutes.
A warm thanks to all the co-authors of the different manuscripts, for the final documentation of successful projects, and for sharing with me the struggle with text, figures, and referees: Alex Peuker, Andreas Held, Andreas Platis, Andreas Scholtz, Andrei Serafimovich, Barbara Altstädter, Beatriz Cañadillas, Belén Bernalte Jiménez, Birgit Wehner, Bruno Piguet, Bughsin Djath, Christof Lüpkes, Dani Martínez-Villagrasa, David Teichert, Detlev Wulff, Dominique Legain, Endres Kathe, Eric Larmanou, Eric Moulin, Falk Pätzold, Fleur Couvreux, Gerald Lohmann, Gert König-Langlo, Guylaine Canut, Holger Baars, Janine Lückerath, Jens Bange, Joan Cuxart, Johannes Degenhardt, Johannes Schulz-Stellenfleth, Jörg Hartmann, Julie Lundquist, Katrin Kohnert, Konrad Bärfuss, Lennart Lobitz, Lutz Bretschneider, Maria Antonia Jiménez, Marie Lothon, Marius Jonassen, Markus Hermann, Michael Jähn, Norman Wildmann, Peter Hecker, Priit Tisler, Ralf Käthner, Richard Foreman, Rolf Hankers, Sabrina Martin, Simon Siedersleben, Stefan Emeis, Stefan Nowak, Thomas Kenull, Thomas Rausch, Timo Vihma, Tom Neumann, Torsten Sachs, Ulf Bestmann, William Maurel, and Wolfram Birmili.
I acknowledge the permission of John Wiley and Sons and the Copyright Clearance Center to reproduce Figures, Tables and a text extract of the article “One-year observations of

https://doi.org/10.24355/dbbs.084-201906170934-0

the wind distribution and low-level jet occurrence at Braunschweig, North German Plain" (License Numbers 44486300622858 and 4486300714899, 12 December 2018).
In the habilitation process, I would like to thank Prof. Dr.-Ing. Eilts, Prof. Dr.-Ing. Tutsch, and Prof. Dr. Dietzel for their interest and support.
I would like to thank cordially Jean - François Gayet, Stephan Weber and Jochen Reuder for their willingness to act as referee for this habilitation treatise.
Thanks to all the persons who motivated me to complete this piece of work, and who provided valuable feedback on the preliminary manuscript: Rolf Hankers, Barbara Altstädter, Stefan Emeis, Rudolf Richter, Shanna Schönhals, Falk Pätzold and Konrad Bärfuss.
Finally and most importantly I would like to thank my family. Thank you, Philipp, for your love and your support in every sense. Thank you, Dominik, Kathleen and Niklas, for the necessary distraction and grounding. I'm so happy to share my life with you.

https://doi.org/10.24355/dbbs.084-201906170934-0

https://doi.org/10.24355/dbbs.084-201906170934-0